Design of a Controllable Inflatable Aeroshell

Final Review

T. de Boer W.Dalmeijer A. Minich I. Ouerghi R. Smis
M. Coppola R. van Loo C. Möckel S. Shabazi E. van Wijk

Design Synthesis Excercise

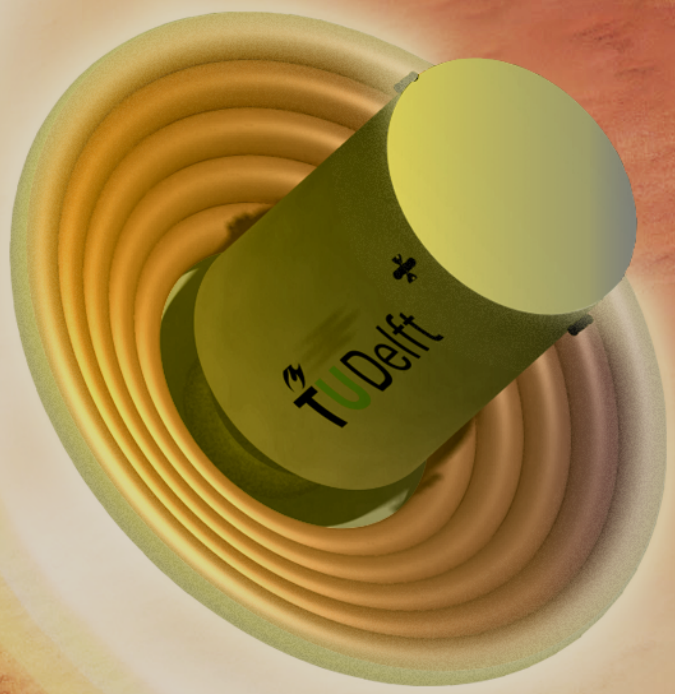

TU Delft Delft University of Technology

Faculty of Aerospace Engineering

Design of a Controllable Inflatable Aeroshell

Final Review

Design Synthesis Excercise

For the Fulfillment of the Bachelor of Science Degree in Aerospace Engineering at Delft University of Technology

DSE-03

T. de Boer
M. Coppola
W. Dalmeijer
R.van Loo
A. Minich
C. Möckel
I. Ouerghi
S. Shabazi
R. Smis

E. van Wijk

July 2, 2013

Version 1.1

Faculty of Aerospace Engineering · Delft University of Technology

Table of Contents

List of Symbols

Abbreviations

α	Angle of Attack	$[rad]$,$[deg]$
β	Sideslip Angle	$[rad]$
χ	Heading with respect to the North	$[rad]$
δm	Distributed Mass	$[kg/m]$
δn	Distributed Load	$[N/m]$
Δ	Thickness of the outer layer	$[m]$
δ	Cone Angle	$[deg]$
δ	Latitude	$[deg]$
$\dot{q}_{conv}$	Rate of Convective Heat Flux	$[W \cdot cm^{-2}]$
ϵ	Emissivity	[-]
γ	Flight Path Angle	$[rad]$,$[deg]$
γ_m	Predicted Average Flight Path Angle	$[rad]$,$[deg]$
γ_{en}	Entrance Flight Path Angle	$[rad]$,$[deg]$
γ_{sh}	Ratio of Specific Heats	[-]
κ_w	Conductivity of the Layer Material	$[W \cdot m^{-1} \cdot K^{-1}]$
λ	Thermal Conductivity of the Airflow	$[W \cdot m^{-1} \cdot K^{-1}]$
$\mathbf{C_M}$	Three-Dimensional Moment Coefficient	[-]
$\mathbf{C_{res}}$	Resultant Force Coefficient	[-]
$\mathbf{S_{ij}}$	Normal Vector of Surface Element **ij**	[-]
$\mathbf{V}$	Velocity Vector	[-]
μ	Bank Angle	$[rad]$,$[deg]$
μ_x^*	Dynamic Viscosity at Reference Temperature	$[m^2/s]$
μ_{t2}	Viscosity Behind the Normal portion of the Shockwave	$[m^2/s]$
ω_n	Natural Radian Frequency	$[Hz]$
ω_t	Mars Rotation Velocity about Z_C Axis	$[rad/s]$
Ω_v	Collision Integral	[-]
ρ	Density	$[kg \cdot m^{-3}]$
ρ^*	Density at Reference Temperature	$[kg \cdot m^{-3}]$
ρ_0	Atmospheric Density	$[kg/m^3]$
ρ_{t2}	Density Behind the Normal Portion of the Shockwave	$[kg \cdot m^{-3}]$
ρ_w	Density of Outer Material	$[kg \cdot m^{-3}]$
σ	Normal Stress	$[N \cdot m^{-2}]$
σ	Stefan Boltzmann Constant	$[Jm^{-2}s^{-1}K^{-4}]$
σ_c	Characteristic Dimension of a Molecule	$[m]$
τ	Longitude	$[N]$
τ	Shear Stress	$[N \cdot m^{-2}]$
θ	Angle between Surface Normal and Freestream	$[deg]$
θ	Half Nose Radius Angle	$[deg]$
θ	Pitch Angle	$[rad]$,$[deg]$
A	Area	$[m^2]$
A	Axial Force	$[N]$
$a_\perp$	Acceleration Perpendicular to Velocity Vector	$[m \cdot s^{-2}]$
$a_{\shortparallel}$	Acceleration Parallel to Velocity Vector	$[m \cdot s^{-2}]$

C_B	Ballistic Coefficient	[-]
C_D	Drag Coefficient	[-]
C_L	Lift Coefficient	[-]
$C_{p,max}$	Maximum Pressure Coefficient	[-]
C_p	Pressure Coefficient	[-]
c_p	Specific Heat at Constant Pressure	$[J/K]$
C_w	Heat Capacity of the Outer Material	$[J/K]$
CH	Stanton Number	$[m]$
CH^*	Stanton Number at Reference Temperature	$[m]$
D	Aeroshell Diameter	$[m]$
D	Drag Force	$[N]$
$dotq_{cond}$	Rate of Conductive heat Flux	$[cm^2]$
$dotq_{rad}$	Rate of radiation heat flux	$[cm^2]$
$dotq_{stored}$	Rate of stored heat flux	$[cm^2]$
E	Young's Modulus	$[N/m^2]$
e_{tor}	Eccentricity of Transfer Orbit	[-]
F	Force	$[N]$
g_m	Average Density over Time Increment	$[kg \cdot m^{-3}]$
g_m	Average Gravitational Acceleration over Time Increment	$[m \cdot s^{-2}]$
h	Convective-heat transfer coefficient	$[W \cdot m^{-2} \cdot K^{-1}]$
h	Distance to Mars Surface	$[m]$
h_a	Height of Apogee	$[m]$
h_d	The Average Atomic Dissociation Energy Multiplied by the Atom Mass Fraction at the Edge of the Boundary Layer	$[J]$
h_m	Average Altitude over Time Increment	$[m]$
h_p	Height of Perigee	$[m]$
H_{t2}	Enthalpy Behind the Normal Portion of the Shockwave	$[J/kg]$
I_{sp}	Specific Impulse	$[s]$
I_{xx}	Mass Moment of Inertia about X_b Axis	$[kg \cdot m^2]$
I_{xy}	Mass Product of Inertia about the X_bY_b Plane	$[kg \cdot m^2]$
I_{xz}	Mass Product of Inertia about the X_bY_b Plane	$[kg \cdot m^2]$
I_{yy}	Mass Moment of Inertia about Y_b Axis	$[kg \cdot m^2]$
I_{yz}	Mass Product of Inertia about the X_bY_b Plane	$[kg \cdot m^2]$
I_{zz}	Mass Moment of Inertia about Z_b Axis	$[kg \cdot m^2]$
K	Column effective length factor	$[-]$
k	Beam deflection stiffness	$[N/m]$
L	Buckling Length	$[m]$
L	Lift Force	$[N]$
Le	Lewis-Semenov Number	[-]
M	Internal Moment	$[Nm]$
M	Molecular Mass	$[g/mol]$
m	Mass	$[kg]$
$M^{'}$	Molecular Mass	$[kg/mol]$
M_∞	Free Stream Mach Number	[-]
M_e	Mach Number at Boundary Layer	[-]
M_x	Moment about the X_b Axis	$[Nm]$
M_y	Moment about the Y_b Axis	$[Nm]$

M_z	Moment about the Z_b Axis	$[Nm]$
N	Internal Normal Force	$[N]$
N	Normal Force	$[N]$
p	Roll Rate	$[rad/s]$
P_0	Atmospheric Pressure	$[N \cdot m^{-2}]$
P_{t2}	Pressure Behind the Normal Portion of the Shockwave	$[N \cdot m^{-2}]$
Pr	Prandtl Number	[-]
q	Pitch Rate	$[rad/s]$
R	Distance to Mars Center	$[m]$
r	Yaw Rate	$[rad/s]$
r_m	Average Radius over Time Increment	$[m]$
R_n	Nose Sphere Radius	$[m]$
R_{loc}	Local Radius	$[m]$
R_{max}	Radius at Cone Edge	$[m]$
r_{orbit}	Distance of Orbiter to Mars Center	$[m]$
Re_x^*	Reynolds Number at Reference Temperature	[-]
S	Side Force	$[N]$
S_{ref}	Reference Surface Area	$[m^2]$
T	Temperature	$[K]$
t	Thickness	$[cm]$
T^*	Temperature Reference	$[K]$
T_m	Average Temperature over Time Increment	$[K]$
T_0	Atmospheric Temperature	$[K]$
T_{aw}	Adiabatic wall temperature	$[K]$
T_{t2}	Temperature Behind the Normal Portion of the Shockwave	$[K]$
T_w	Wall temperature	$[K]$
u_e	Airflow Speed just Outside the Boundary Layer	$[m/s]$
V	Velocity	$[m/s]$
v	Internal Shear Force	$[N]$
$V_e x$	Atmospheric Exit Velocity	$[m/s]$
V_m	Predicted Average Velocity	$[m/s]$
V_{orbit}	Orbital Velocity	$[m/s]$
x, y, z	x-, y- and z-Coordinates	$[m]$
x^*	Distance over Half of the Nose Arc Parallel to the Straight Shell Segment	$[m]$
x_{gt}	Ground Track along X_m Axis	$[m]$
y_{gt}	Ground Track along Y_m Axis	$[m]$

Abbreviations

$AC1-3$	Aerocapture Entrance Corridor Trajectory
CFD	Computational Fluid Dynamics
c.g.	Center of Gravity
c.p.	Center of Pressure
DSE	Design Synthesis Exercise
$E-M$	Earth to Mars
EDL	Entry, Descent and Landing
$EDL1-3$	Entry,Descent to Landing Entrance Corridor Trajectory
EOM	Equations of Motion
GNC	Guidance and Navigation Control
$HEART$	High Energy Atmospheric Re-entry Test
$HIAD$	Hypersonic Inflatable Aerodynamic Decelerator
$IRVE-3$	Inflatable Reentry Vehicle Experiment 3
ISS	International Space Station
JOD	One-Degree-Of -Freedom Joint
LEO	Low Earth Orbit
LMO	Low Mars Orbit
$M-E$	Mars to Earth
$MIAS$	Mars Inflatable Aeroshell System
MSL	Mars Science Laboratory
PA	Primary Assumption
$RAMS$	Reliability, Availability, Maintainability, and Safety
TPS	Thermal Protection System
TRL	Technology Readiness Level
UP	Updates for Trajectory Simulation

Acknowledgment

The group would like to acknowledge Herman Damveld, Steve Sandford and Jinglang Feng for their guidance and supervision throughout the last 10 weeks. Their help has been paramount to the success of this Design Synthesis Exercise.

We would also like to express our special thanks and gratitude to Alicia Dwyer Cianciolo, Richard Powell, F. McNeil Cheatwood, and Robert Dillman. Despite complications with distance and time zones, they have been extremely helpful and provided us with indispensable insight through teleconferences.

Furthermore, we would like to recognize Ping Chu, Ian Richardson, Erwin Mooij, Ron Noomen, Kees Sudmeijer and Ferry Schrijer for their expert opinion. They have provided the group with the in-house technical expertise needed to move the project forward.

Introduction

The opportunities and possibilities enabled by successfully manned space-flight to Mars are endless. Its great potential has formed many needs within the scientific community. However, the main obstacle is safe transportation to and from Earth. Generally, interplanetary flight requires a large velocity increment when departing from Earth followed by a large velocity decrement upon arrival at the target planet. Conventional braking maneuvers performed with rocket engines require such substantial amounts of fuel that the compounded weight that is required during launch to accommodate these systems makes the entire mission economically nonviable. The feasibility of using concepts currently in existence and operation for a manned mission to Mars is low due to cost constraints. A promising solution that is currently undergoing development is to decelerate by using the Martian atmosphere. This technique provides the benefits of lower launch masses and lower overall costs, but presents many difficulties. Aerobraking and atmospheric entry require a sufficiently large decelerating heatshield (i.e. aeroshell), which is unable to fit in existing launcher fairings. The National Aeronautics and Space Administration (NASA) has invested their interest into the development of inflatable aeroshell technologies for their benefits in weight and cost reduction, and the possibility of deploying aeroshells larger than the limits imposed by current launch systems.

The scope of this project has been the design, by 10 students in 45 working days, of an inflatable aeroshell that will be used by a precursor spacecraft to the surface of Mars. The earlier stages of the overall space-flight envelope, including launch, were not analyzed in depth. The design and development of a controllable, guided deceleration system has been achieved by the students by applying the available knowledge in aero-, astro- and thermodynamics, structural and material analysis, and various systems engineering and integration tools. The main requirements were derived from the human payload and stakeholder needs. The main conditions stemmed from the desire to optimize the entry vehicle for controllability, reliability and weight and involved amending some of the soft requirements to better optimize the entire system.

The Project Plan presented organizational elements that concerned structuring the project's human resources, scheduling and work break-down approach [1]. The Baseline Review then described the preliminary systems engineering steps taken to arrive at potential design options [2]. This involved functional, requirement, and risk analyses including preliminary astrodynamic calculations. The Midterm Review presented the design logic that lead to a chosen controllability concept that proceeded to the detailed design phase. The Final Review is a continuation of the Midterm Report where detailed design analysis is performed on the recommended design option. The report describes the design analysis in four main parts: General Overview, Design Analysis, Design Review and Future Outlook and Final Comments.

General Overview is composed of Chapter 1 and 2. In Section 1-1 the problem statement is defined. Section 1-2 analyses all the functions the spacecraft must perform for a successful mission performance. Section 1-3 lists the requirements that the overall spacecraft must be ultimately designed to meet. In Section 2-1 the preliminary work completed will be summarized for clarity and completeness. General Overview concludes with Section 2-2 where the final recommended design will be previewed. The final rendered diagram is given for illustrative purposes and to summarize the resulting product of the Design Synthesis Exercise. A summary of the design is presented in a table giving the overall properties of the complete spacecraft found in A.

Design Analysis is composed of chapters 3 to 8. Chapter 3 details the astrodynamic characteristics of the trajectory for both the interplanetary travel and target orbit (between aerocapture and Entry, Descent and Landing) around Mars. In Chapter 4 the aerodynamic properties of the aeroshell are analyzed and followed by a sensitivity analysis. Chapter 5 then includes the atmospheric model and trajectory design for both aerocapture and the entry, descent and landing maneuvers. Chapter 6 entails the thermal protection system (TPS) design which commences with heat loading analysis and concludes with material selection and a final recommended TPS. Chapter 7 is composed of three sections; vehicle sizing, design logic and expected loading. Vehicle sizing is concerned with the overall spacecraft dimensions while the design logic section concerns the actuation system used for controllability. The expected loading analyses the characteristic loads that should be designed for while mechanism design further details the sizing of the actuation system based on stresses. Chapter 8 starts by exploring the expected motions of the spacecraft from which a control strategy is developed and a controller is ultimately designed for longitudinal and lateral motions. The chapter concludes with controller testing using Simulink®.

Design Review is composed of chapters 9 to 11. To commence, Part III describes the resource allocation and budget breakdown for the mass, cost and computing power of the complete spacecraft. Chapter 10 entails the operational and logistical support required to develop and use the Mars bound spacecraft. Chapter 11 analyses the design of the complete spacecraft. It does this through a sustainability analysis, a sensitivity analysis, a technical risk assessment, reliability, availability, maintainability, and safety (RAMS) characteristics and a compliance matrix. The compliance matrix indicates how well the mission requirements are met and gives the reader an indication of what still needs to be further developed.

The future road map is planned in the final part, Future Development consists of chapters 12 and 13. Section 12-1 describes the development logic and what activities are planned in the future to further the project from the conceptual to the detailed design phase. This is followed by Section 12-2 which analyses the commercial value of the spacecraft and the merging market it consequently creates. The final section, gives an overview of the report and the subsequent conclusions, followed by a reference of cited sources. The reader should note that variables present in equations and abbreviations henceforth are clarified in Nomenclature.

Part I

General Overview

Chapter 1

Mission Description

This chapter introduces the project in more detail, with formulations of the Mission Need and Project Objective statements, a general description of the mission, functional analysis and the mission requirements. The general mission description provides the rationale for this project's existence and defines the project's scope. The functional analysis presents a chronographic description of the functions that the system is expected to perform. The mission requirements, as derived from the functional breakdown structure, are shown in the homonymous section.

1-1 Problem Statement

The following section provides an introduction to the mission and details the scope of the project.

Mission Need Statement

A system architecture for the controllable, guided deceleration of an exploration-class vehicle from an interplanetary orbit to a particular location in Martian atmosphere with a particular energy at arrival.

Project Objective Statement

The design, by 10 students in 10 weeks, of a controllable system architecture for the guided atmosphere-assisted deceleration of a vehicle that employs an inflatable aeroshell that allows an exploration-class precursor spacecraft to arrive at a particular location in Martian atmosphere, with a particular energy level before landing on the surface.

General Mission Description

The general mission is to safely transport three or more astronauts to the Martian surface along with a payload of circa $9000kg$. The mission's difference from previous Mars landers is that it requires the landing of an unprecedented amount of mass with human-rated precision and reliability. The problem requires the design of a system that would sufficiently decelerate the mass using Mars' thin atmosphere to be able to perform landing. The limiting parameter for the design of a heat-shield to protect the payload from hypersonic flow at entry, is the diameter

of the launcher fairing. Designing a conventionally rigid aeroshell with a $5m$ diameter for the deceleration of a $9ton$ spacecraft would require TPS that is far too heavy.

One of NASA's solutions [3] to this particular challenge is the inflatable aeroshell - lighter than its rigid counterpart, deployable to greater sizes (increasing surface area and drag increases deceleration capabilities), and packable into the given dimensions. The scope of this project is to recommend and argument the design of a control system that would guide the inflatable aeroshell to a particular target box in the Martian atmosphere with a particular energy upon arrival. For reliability and accuracy concerns, fully ballistic entry was immediately discarded and the focus shifted to lift generating bodies and control over the vehicle's cross-range.

To dissipate enough energy, the vehicle will need to interact with the atmosphere more than once. Given humans on board, reliability and safety are top priorities and the number of interactions should be minimized to reduce the likelihood of error and subsequent mission failure. This results with a maximum of two interactions: 1 aerocapture and 1 EDL maneuver. Aerocapture will reduce the energy from interplanetary flight to orbital levels while EDL will serve to decelerate the vehicle to a speed where conventional supersonic deceleration methods are apt.

Returning astronauts to earth is outside the scope of this project. Ideally, the infrastructure that would enable the return mission will have already been established using precursor missions. The requirements and constraints that limit the design space will mostly stem from the fact that the vehicle is human rated. The minimum entry mass, maximum deceleration loads, thermal loads, and mission reliability are all derivatives of the project objective and will be top-priority. The softer requirements related to current technology readiness levels and/or particular stakeholder interests will be open to changes given stakeholder approval.

1-2 Functional Analysis

This chapters concerns the functions that the spacecraft system must perform. It will be presented in a time-sequenced flow diagram that depicts the logical flow of functions necessary to perform a successful mission. Additionally, all supporting, time-independent functions will be graphically represented in a functional breakdown structure.

Functional Flow Diagram

The functional flow diagram (FFD) shown in Figure 1-1 depicts the time-sequenced actions that are performed by the spacecraft (sub)systems during the mission. The top level, or tier zero, shows the outline of the entire mission. The mission architecture considers a spacecraft that transfers from the interplanetary travel stage to an orbit around Mars through an aerocapting procedure, this is then followed by a target orbit and EDL procedure. The EDL module will continue to perform controlled descent through aerobreaking to soft land the manned payload on the surface of Mars.

Of the tier zero overview, two functions are considered in more detail as they are the focus of this project. These stages, 4.0 Interplanetary Travel and 5.0 Entry (Aerobraking), are discussed in the remainder of this section.

Interplanetary Travel - Interplanetary travel is dominated by the operations that will deliver the spacecraft to its target with greatest accuracy. The attitude, position and velocity are constantly monitored and adjusted when necessary. When the spacecraft nears the end of its interplanetary flight to Mars, it undergoes preparations for the aerocapture stage. This includes removing anything that is no longer required and deploying the aeroshell. The correct inflation and deployment of the aeroshell will be checked and in the event of incomplete/incorrect inflation, corrective actions will be taken.

Aerocapture) - During the aerocapture maneuver it is very important that the correct attitude, position and velocity are known. The results of sensor measurements will be used to calculate the trajectory the spacecraft will follow. Upon entry into Martian orbit, this knowledge is combined with measurements of the loads experienced on the shell to allow the control computer to evaluate its determined nominal trajectory. The control system can then make course corrections to avoid experiencing critical loads or target overshoot by use of its control algorithm.

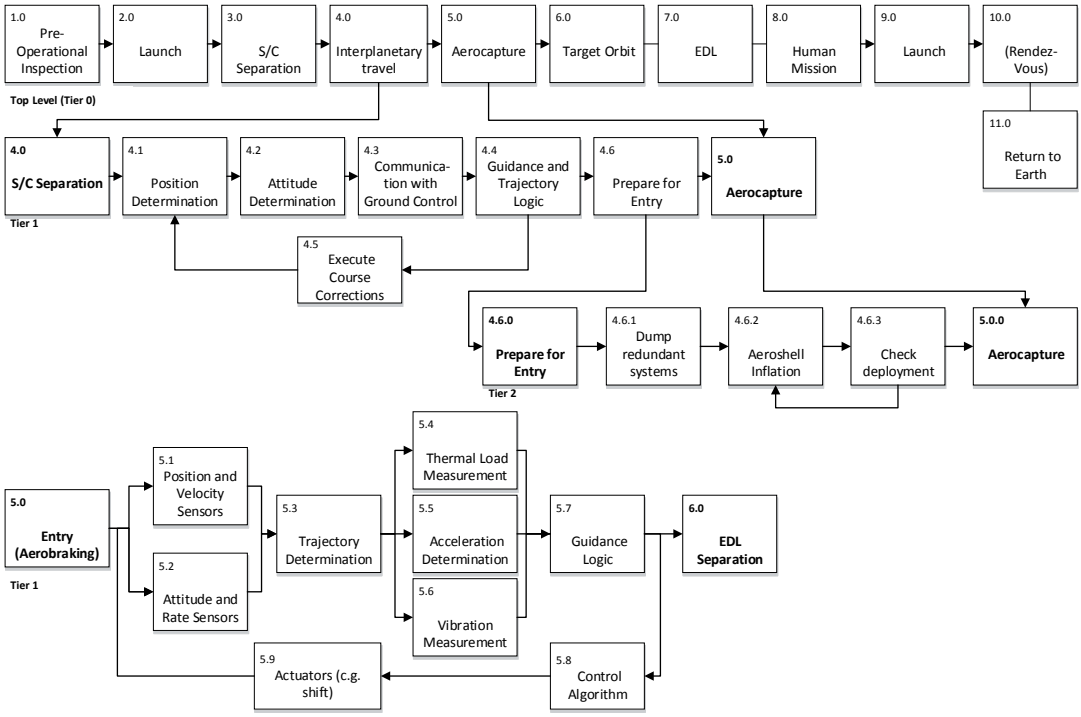

Figure 1-1: Functonal Flow Diagram(FFD)

Functional Breakdown Structure

A functional breakdown structure is presented in this section in Figure 1-2 to characterize all the functions that the spacecraft should perform to ensure a successful entry into Martian atmosphere. This will be presented as an AND tree where seven main functional groups have been distinguished that branch into their respective constituents.

Communications The first functional group is 'Communications,' which contains three main components: the ground station, the orbiter, and other spacecraft. Communication with ground control is a critical function since trajectory information and control commands would potentially be conveyed through this function. Similarly, communication with the orbiter is critical to the return of the EDL module to Earth and is therefore a main functional element. Communication capabilities with other spacecraft are important to avoid collisions in space by accounting for their spatial position during trajectory/navigation determination.

Power The second functional group is 'Power.' It is crucial for the performance of the spacecraft since almost all systems or subsystems are neither hydraulic nor pneumatic but rather electrical. Hence, the electrical power supply must properly distribute and regulate the flow of electricity to the subsystems to ensure proper performance. Additionally, an alternate power supply may

be included for redundancy so it is important to have functional compliance with this secondary power source.

Navigation and Control The third functional group is 'Navigation and Control,' which is mostly responsible for the functional ability to generate navigation and trajectory information and transmit these as commands to the control subsystems. This functional group is comparable to a brain as it is responsible for commands and decisive actions. The functional group 'Controlled Deceleration,' following the same analogy, would be the muscles of the system - receiving control commands and implementing them to result in a controlled, stable deceleration of the spacecraft during entry into Martian atmosphere.

Protection 'Protection' is a functional group which comprises all functions related to the protection of the payload from the harsh space environment and conditions during atmospheric entry. This includes providing structural integrity and thermal protection and dissipating excess energies. Additionally, the spacecraft needs to have the functionality to protect its crew from space radiation, ionization, temperature and vacuum.

Sustainability Sustainability is a growing concern in the modern space age due to the growing amount of space debris and increasing risk of collisions. Also, general pollution has increased and limited resources are becoming more scarce. Sustainability has become critical and needs to be incorporated as a function to ensure limited negative externalities. Negative externalities refers to all the negative effects to the environment caused by the mission. An example is the need to have functions to jettison elements that are no longer needed, in a sustainable manner (to burn up upon entry or boost to dead obit). This also refers to having functions that perform in a sustainable manner which for example, don't result in the formation of craters on the Martian surface as a consequence of the release of tungsten masses to introduce a center-of-gravity offset. Additionally, the functions of the spacecraft should perform in a manner that limits the generation of space debris.

Life Support The final functional group is 'life support' which encompasses all functions related to the safety and comfort of the humans on board the spacecraft. These functions are critical to the success of the manned mission and include providing oxygen, water, food and managing waste disposal. Functions to control the humidity and temperature are necessary for comfort. Withal, the spacecraft must also provide functions to supply astronauts with exercise and entertainment to ensure both physical and mental health throughout the journey to Mars.

1-3 Mission Requirements

The project statement can be broken down into a series of requirements; fulfilling these requirements indicates a successful product. In the Baseline Review [2], a requirement tree was developed to track all requirements and the relative types and categories. The requirements were subdivided into the following categories:

- *Global Constraints* that apply to the design of the mission
  - **Development (DEV):** concern the development of the system
  - **Human Rated (HUM):** deals with the human payload that is expected on this manned precursor mission
  - **General (GEN):** cannot be placed in any specific category
- *System Requirements* that apply to the spacecraft directly
  - **Guidance, Navigation and Control (GNC):** are to provide the control system with constraints and guidelines

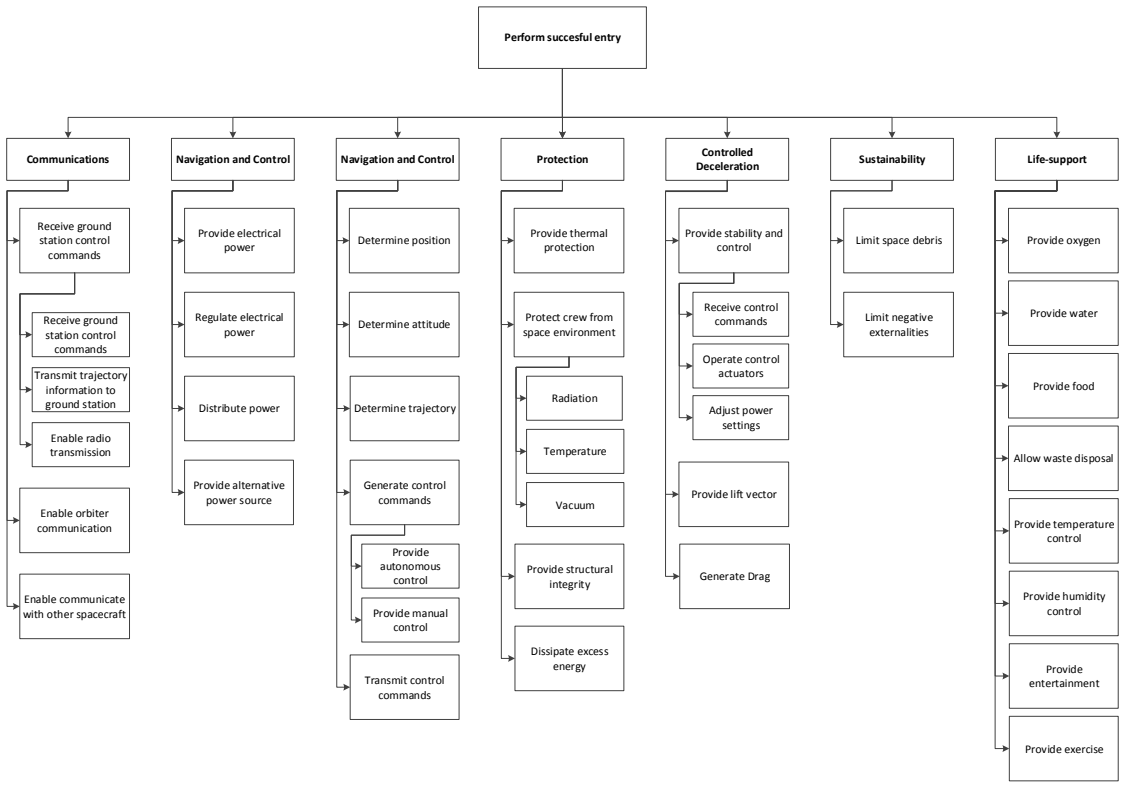

Figure 1-2: Functonal Breakdown Structure(FBS)

- **Aerodynamic (AER):** include all parameters of aerocapture and EDL that must be satisfied
- **Astrodynamic (AST):** deals with all orbital parameters and characteristics
- **Thermal Protection System (TPS):** quantifies the heat protection that is expected by the aeroshell
- **Structural (STR):** relates to the overall structure of the spacecraft

Using this approach, a list of requirements was identified. The list was extended to incorporate a date stamp to track any updates in the requirements, and a column to further categorize all requirements between **hard requirements** and **soft requirements**. The hard requirements are requirements that are considered key and requirement compliance should be assured. Soft requirements are requirements that are favorable to the mission statement, but can be amended to suit the hard/key requirements. The final list is presented in Appendix B.

Following the breakdown and identification procedures, a set of key requirements was identified. These key requirements will drive the design of the final product. The design choices throughout Part II are primarily made to suit this set of key requirements. These requirements will thusly take priority when decisions are made throughout all design stages. The key requirements are outlined in Table 1-1.

Table 1-1: List of key requirements (S = soft requirement, H = hard requirement)

Req. Number	Type	Requirement	Date	Level
1	AER	The spacecraft is to perform Entry, Descent and Landing to a target velocity of Mach 1.8 at 13 km	26/05/13	H
2	AER	The spacecraft is to guide the Entry, Descent and Landing along the determined downrange with a final accuracy of ±150m at 13km altitude	26/05/13	H
3	AER	The aerocapture must allow for dissipation of enough energy to leave the martian atmosphere with 4715 m/s	29/05/13	H
4	AER	The GNC must allow for an aerocapture exit flight path angle of 9.08 deg	18/06/13	H
5	AER	The spacecraft is to guide the Entry, Descent and Landing along the determined crossrange with a final accuracy of ±37.5m at 13km altitude	26/05/13	H
6	AER	The spacecraft is to enter the atmosphere at a speed of 7 km/s with a flight path angle of -11.05 deg	02/05/13	S
19	GNC	The system must employ an automated control system which can perform the landing on Mars autonomously	02/05/13	H
27	HUM	The accelerations on the spacecraft must not exceed 5.2g	26/05/13	H
28	HUM	The time between aerocapture and EDL must not exceed 10 days	03/06/13	S
30	STR	The mass of the vehicle must not exceed 10 000 kg	02/05/13	H
31	STR	The diameter of the fairing must not exceed 5 m	02/05/13	H
32	STR	The mass of the hypersonic atmospheric assisted decelerator must not exceed 10% of the vehicle's entry mass	02/05/13	H
33	STR	The diameter of the aeroshell must not exceed 13 m	02/05/13	S
41	TPS	The TPS system of the aeroshell must be able to withstand the heat flux during aerocapture and EDL	29/05/13	H

Legend	Type	Level
	GE = General HUM = Human DEV = Development Requirements AER = Aerodynamics AST = Astrodynamics GNC = Guidance, Navigation & Controll TPS = Termal Protection System	H = Hard Requirement S = Soft Requirement

Chapter 2

Design Process

The following chapter outlines the progress that preceded the work presented in this report and gives a brief introduction to the end result of the efforts - the final design concept.

2-1 Preliminary Work Performed

Three prior milestones precede and build towards the Final Review - the Project Plan [1], the Baseline Review [2] and the Midterm Review [4]. In the Project Plan, the planning phase of the design focused mainly on the organizational aspects of the project. This involved structuring the work flow, assigning team functions, planning processes and interactions, scheduling tasks and addressing development risks. The work flow following project organization was split into four phases - project definition, conceptual design, detailed design, and project closeout.

Documented in the Baseline Review, the project definition provided a detailed description of what the project entails: the mission need statement, and the project objective that defined the focus. Functional analysis led to a detailed list of requirements and a preliminary feasibility assessment of the mission as a whole. A second risk analysis addressed technical risks and contingencies in development. The project definition phase also included a preliminary budget analysis, a strategy for sustainable development, and design-option analyses resulting in the first iteration of the Design Option Tree (DOT).

The goal of the conceptual design phase was to generate one or two concepts that have the highest potential of satisfying mission needs while conforming to mission requirements. This was documented in the Midterm Review where mission design and concept selection were performed in parallel to optimize the available time. The mission design then created the groundwork for aerocapture and EDL trajectories. Following a brief explanation of the Martian atmosphere, the list of requirements was updated with the outputs from the initial sizing process for transfer orbit. With an updated set of requirements, preliminary calculations were performed to estimate the aerocapture and EDL maneuvers. Finally, an introduction to the numerical scheme was given that refined the EDL and aerocapture analyses. Staging was a facet of mission design that was investigated to determine how best to combine the inflatable aeroshell with existing technologies to satisfy the key requirements (chief among them requirement 1 in AppendixB). Driven by the safety and reliability requirements that come from transporting humans the final choice of staging was to use a single inflatable aeroshell to decelerate to Mach 1.8 and use conventional supersonic methods to touch down. Concept selection and analysis, in turn, began where the project definition phase

concluded. The DOT passed several feasibility checks, amendments and elaborations before being subjected to the Qualitative Design Option Ranking that led to concept generation and concept selection. The five chosen concepts were analyzed in greater detail in the concept analysis stage. Each concept was evaluated based on available quantifiable data (including aerothermodynamic models), technical risk assessment, and sustainability. The final trade-off led to the selection of a concept that came second in ranking, but was chosen for its greater potential but was accompanied with a higher risk. The concept promises great future potential and was appealing for its innovation and technological advancement. The concept that was chosen for further analysis and detailed design for lift generation and attitude control was the external, double-axis center of gravity offset shown in Figure 2-1.

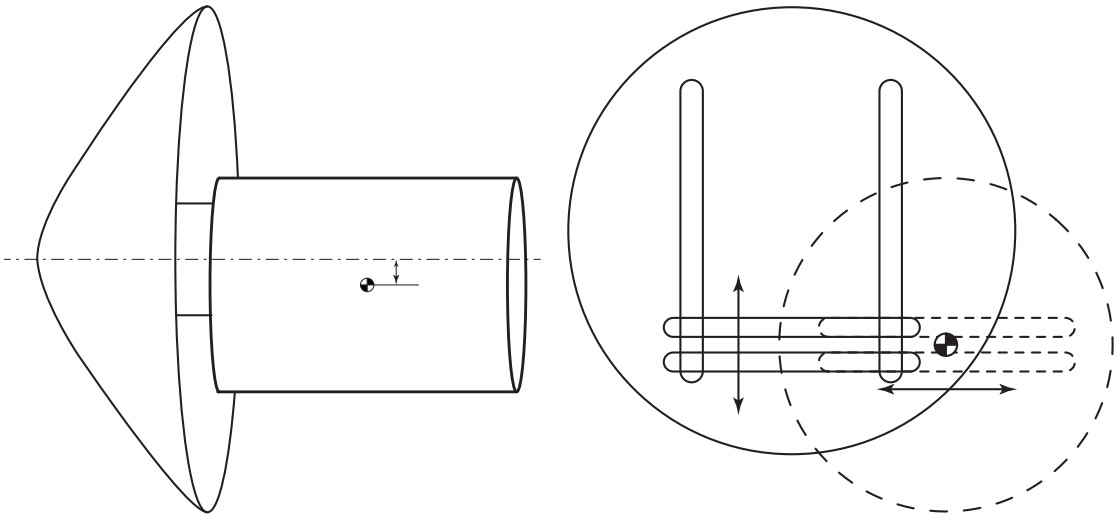

Figure 2-1: Artist's rendition of the external double-axis c.g.

2-2 Preview of Final Design Concept

The final design of the mechanism is as shown in Figure 2-2. Note that the aft body (spacecraft bus and payload) depicted here is given its maximum allowable length, *not* the average aft body length (for a distinction between the two, see Section 7-1).

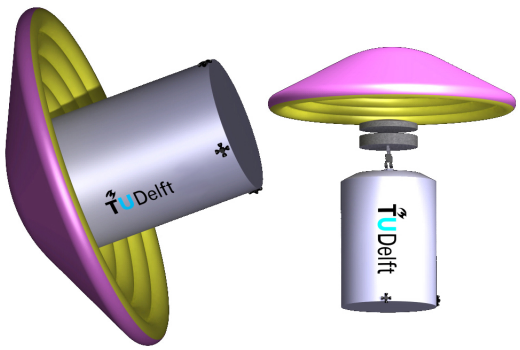

Figure 2-2: Rendering of the final vehicle design.

The control mechanism (as seen in Figure 2-3) serves two purposes - it connects the aeroshell to the

aft body (for this it needs to be rigid) and it provides the vehicle with a means of creating an angle of attack and controlling the direction of the lift vector with a double-axis center of gravity (c.g.) offset system (for this it needs to be able to displace the aft body's c.g. laterally and longitudinally with respect to the center line of the aeroshell). The aeroshell cap (disc $3m$ in diameter) is connected to the aft body cap (disc $3.5m$ in diameter) with a solid-titanium rectangular t-beam frame housed in pairs of orthogonal rails. The two rails mounted on the payload cap provide travel for the longitudinal displacement of the c.g. of the aft body with respect to the aeroshell's center line and the two rails mounted on the aeroshell cap enable the lateral c.g. offset. The simplest way of actuating the control mechanism is through a rack and pinion system where the t-beams act as racks and gears interacting with the t-beams through cut-outs in the floors of the rails act as pinions. In this configuration the titanium construction would have a mass of circa $290kg$ and the four $3kW$ electrical motor-reduction systems found in subsection 7-3-3 required to actuate it would have a mass of circa $20kg$ each - so $370kg$ for the system as a whole with conservative stress margins and redundancy (two $3kW$ electrical motor-reduction systems would be able to actuate the mechanism on their own.)

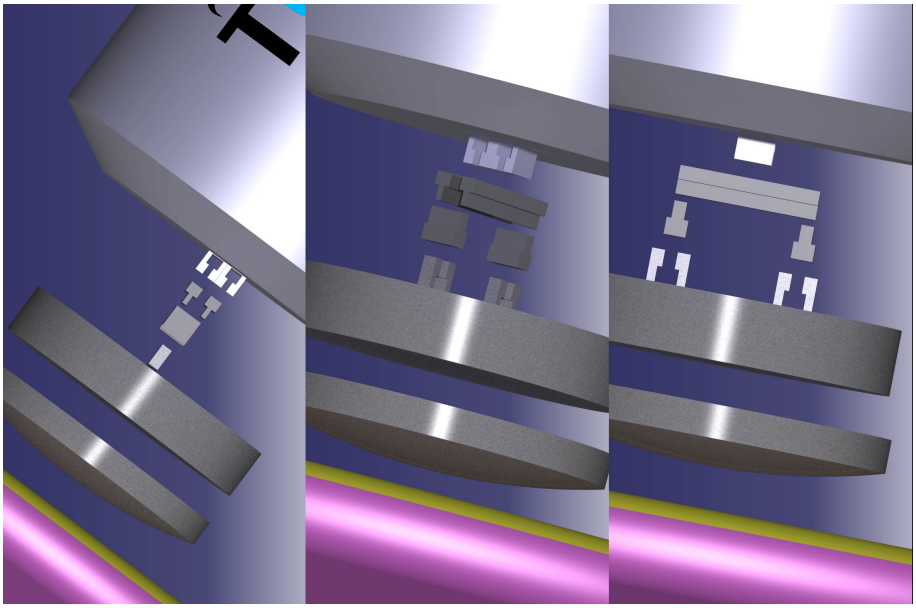

Figure 2-3: Rendering of the control mechanism

Part II

Design Analysis

Chapter 3

Astrodynamic Trajectories

This chapter describes how the interplanetary travel and post-aerocapture target orbit was characterized. Emphasis was put on energy efficiency as well as minimizing risk. The first section of this chapter discusses the design of an interplanetary orbit from Earth to Mars (E-M) and return (M-E). The next deals with the design of a post-aerocapture transfer and target orbit, on which the spacecraft will remain for a maximum of 10 days prior to EDL. A Level of Care Four as described by [5] is required; this limits the total continuous time in space to 210 days, which will include interplanetary travel and post-aerocapture/pre-EDL orbit.

3-1 Interplanetary Travel

This section covers the design drivers and design characteristics of interplanetary travel for a Mars return mission. The required(ΔV-budget) and corresponding launch mass for a specified mission duration are provided. The characteristics of a type I, high energy transfer to and from Mars are determined. These separate transfers are to be combined when the overall mission is planned.

3-1-1 Type I Transfers

First an overview of interplanetary transfer orbits will be given, starting with the assumption used to obtain a model to determine transfer trajectories with corresponding ΔV - budget, mass and transfer time. Thereafter, the methodology will be explained and the section will be concluded by discussing the obtained results.

Limitations

The aim of the model is to indicate the orbital characteristics. To minimize the complexity of the calculations, the limitations due to the assumptions by [6] are listed.

L1 No free return missions are considered due to time constraints of the research. Free return trajectories are transfer ellipses that allow the spacecraft to return to Earth without an additional ΔV-budget if interception with Mars is missed or the mission is aborted. This limitation can result in a recommended mission design that does not allow for free return if problems occur.

L2 The applied approach does not deal with departure within an atmosphere, this reduces the ΔV budget significantly. To be able to approach the total ΔV more accurately, departure from the equators is assumed, where the equatorial rotation speed for Earth is $1.674 km/s$ and for Mars $0.868 km/s$. To correct for the aerodynamic drag a ΔV budget of $2 km/s$ is added for launch from Earth and $1 km/s$ for launch from Mars [7].

Methodology

The approach that is applied is obtained from Noomen [6], where all performed steps are explained in detail. The model is designed to obtain the best solution with respect to the required ΔV budget, for a given mission duration. For a more detailed description of the methodology please contact the authors of this report.

Results

The method is used to obtain a range of different high energy type I transfers from Earth to Mars. In Figure 3-1 and Figure 3-2 the ΔV plots are depicted for E-M and M-E transfers respectively. The total ΔV-budget is split into a ΔV to be delivered partly by the launcher, and partly by the spacecraft. The ΔV of the spacecraft for E-M remains zero until the arrival velocity is larger than $7 km/s$, then a propulsive deceleration is required before entry. For M-E the arrival velocity is for the complete range larger then $7 km/s$. It can be concluded that for a reduced transfer time, the excess velocity should increase and therefore the ΔV budget increases.
Corresponding to the ΔV-budgets, mass estimations are plotted in Figure 3-3 and Figure 3-4 for E-M and M-E transfer respectively. For these computations a two stage launcher is assumed with a specific impulse (I_sp) of $400s$ for the first stage and $450s$ for the second stage. In the E-M figure, a kink occurs at a transfer time of 160 days, this corresponds to the kink in the ΔV plot of the spacecraft for E-M. At this point the spacecraft cannot reduce its velocity completely by aerocapture, therefore an additional propulsive decelerator is required. Due to the snowball effect throughout the stages, this propellant mass is a heavy penalty for the launch mass. This underlines the importance of aerocapture where arrival mass can be saved, which reduces the launch mass significantly and therefore launch costs.

The model is applied to a mission duration of 1 to 2300 days. For a mission duration up to 485 days no solutions exist for the limited ΔV budget and parallel excess velocity to the heliocentric velocity of the departure planets. For short mission durations a flyby at Venus can be performed [8], to limit calculation complexity, this is not taken into account in the model. After 485 days solutions exist that require high ΔV budgets, this reduces to a minimum of $22.10 km/s$ for a mission duration of 515 days. Launch at Earth requires $11.96 km/s$, launch at Mars $6.10 km/s$ and the spacecraft has to decelerate $4.05 km/s$ before Earth entry. This option requires a E-M transfer of 199 days and a M-E transfer of 199 days. Therefore, one has to depart at a relative position of Earth and Mars of $\Delta\theta_{E-M}$ $44.6 deg$. Due to the synchronization time this will occur every 780 days. The total required launch mass corresponding to this mission design is $866,000 kg$, this includes a launch mass of $595,000 kg$ from Earth. For Mars this is $271,000 kg$, assuming that only a launch will be used and no rendezvous. The required launch mass at Mars shows that multiple precursor missions are needed to obtain a sufficient launch system at Mars.

Sensitivity Analysis

The study shows that a required mission duration should be wisely chosen. A small change in mission duration can result in a significant weight penalty, due to the use of inefficient transfer trajectories.
The model is also sensitive for aerocapture capabilities. A higher aerodynamic assisted deceleration will lower the ΔV_3 required, thereby lowering the spacecraft weight. Therefore the propellant weight of the last launch stage can be lowered, lowering the required propellant weight of the

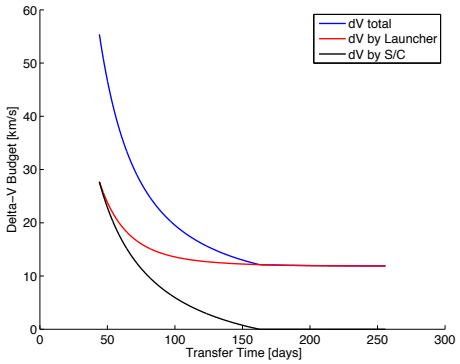

Figure 3-1: Change in Δ-V budget with transfer time for Earth to Mars transfer

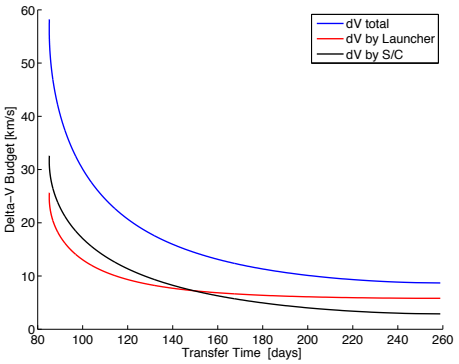

Figure 3-2: Change in Δ-V budget with transfer time for Mars to Earth transfer

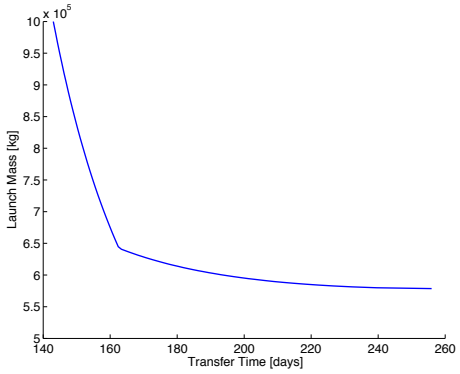

Figure 3-3: Change in launch mass with transfer time for Earth to Mars transfer

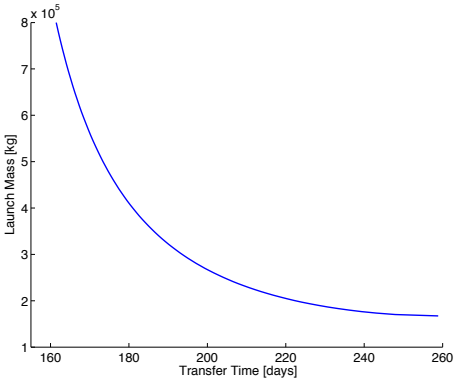

Figure 3-4: Change in launch mass with transfer time for Mars to Earth transfer

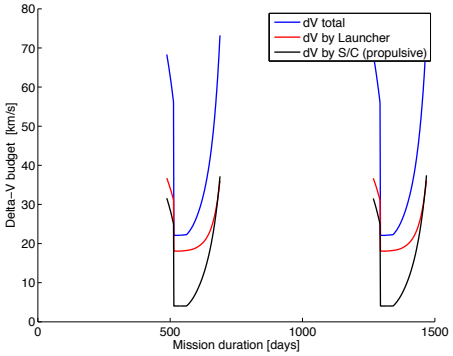

Figure 3-5: Change in Δ-V budget with transfer time for complete mission design

previous stage, and so on. Due to this snowball effect the launch mass is sensitive to changes in the aerocapture capability, as is visible in Figure 3-1.

3-2 Post Aerocapture Transfer and Target Orbit Characterization

Following the aerocapture maneuver the spacecraft will remain in a temporary orbit around Mars, for a maximum time of 10 days, until the conditions in the landing-site are favorable and EDL is performed. To reach this orbit (referred to as "target orbit"), the aerocapture maneuver must continue into a transfer orbit, followed by a periapsis raise. The interested reader is referred to the Midterm Review [4] for a more detailed analysis of this phase. This section summarizes the design logic and the results obtained, which were then used to constrain the aerocapture and EDL maneuvers as seen in Chapter 5.

3-2-1 Assumptions

The assumptions used throughout this section to estimate the orbital parameters are:

PA1 The Equations of Motion are based on point masses in a two-body problem.
PA2 No energy is dissipated to the environment except during aerocapture and re-entry maneuvers.
PA3 The maneuver is a planar motion.

3-2-2 Methedology: Target Orbit

The detailed method and the relationships used to design the orbit are presented in the Midterm Review. The two most important equations for the process are restated in this section.

Vis-Visa relation The Vis-Visa, Equation 3-1 from [9], is a relation between the position r_{orbit}, velocity V_{orbit} and semi-major a_{orbit} of an orbit; it can be derived from the law of conservation of energy. The equation was used to obtain information on the periapsis raise maneuver and velocity upon exit and entry of the atmosphere.

$$V_{orbit}^2 = \mu \left(\frac{2}{r_{orbit}} - \frac{1}{a_{orbit}} \right) \tag{3-1}$$

Flight Path Angle - Velocity Equation To obtain information on the desired aerocapture exit conditions, Equation 3-2 was used to determine the desired combination of exit velocity V_{ex} and exit flight path γ_{ex} angle [9].

$$k_i = \frac{V_{ex}^2}{V_c^2} \qquad e_{tor} = \sqrt{1 - k_i(2 - k_i)cos^2(\gamma_{ex})} \tag{3-2}$$

3-2-3 Target Orbit Sizing Logic

A schematic flowchart of the method used is displayed in Figure 3-5. Two parameters of the target orbit were fixed: the orbital period and the periapsis. The aim was to keep the post-aerocapture velocity increment to reach the target orbit to a minimum. The periapsis was thus fixed just outside of the atmosphere ($200km$ altitude) so as to avoid atmospheric interactions, yet minimize velocity budget. The output of this estimation process was a set of boundary conditions (velocity, flight path angle) for an aerocapture maneuver that, upon exit, reaches the apoapsis of a Mars-synchronous eccentric orbit.

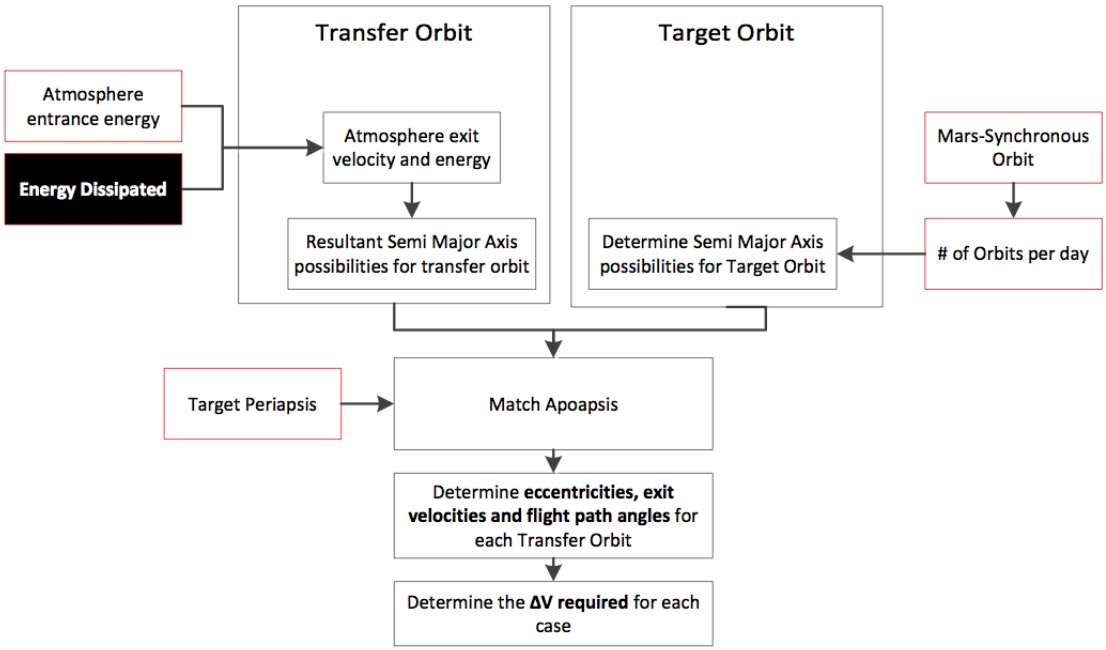

Figure 3-6: Flow-chart for the target orbit sizing simulation

Target Orbit Type Analysis

The choice of the target orbit was determined by several key drivers:

- **Energy dissipation ratio** Analysis of the heat loading in Chapter 6 and literature [10] have shown that the highest heat flux is expected during the aerocapture maneuver. To limit the constraints on the aerocapture maneuver, the velocity loss in the aerocapture maneuver was kept to a minimum. The maximum exit velocity from the atmosphere was determined by the Martian escape velocity of $5km/s$.
- **Energy efficiency** The ΔV budget required to raise the periapsis outside of the atmosphere is correlated to the type of post-aerocapture orbit. The eccentric orbit offers the advantages of a relatively small increase in velocity at the apoapsis to avoid further interaction with the atmosphere at periapsis. Oppositely, a circular orbit requires a higher velocity increment to circularize the orbit, resulting in a higher fuel mass.
- **Accuracy** An eccentric orbit requires a higher accuracy due to its higher sensitivity with respect to the exit conditions as visualized in Figure 3-6. The figure describes the relation between exit conditions and the post aerocapture ΔV burn. The lower limit is set by the physical limitations of the system. Furthermore, the position where the periapsis raise maneuver is performed is constrained by the final target box. A circular orbit allows for a higher error margin in exit conditions, as the position where the circularizing maneuver is performed is of less importance.
- **Risk** The closer the exit velocity is to the maximum exit velocity the higher is the risk of performing a so called "fly by". Hence, a small safety margin is recommended to allow for possible inaccuracy.

The final choice for the target orbit, as elaborated in detail in the Midterm Review, was an eccentric Mars-synchronous orbit. The final choice is based on an iteration process that resulted in the following exit condition: $\gamma_e x = 9.08$ and $V_e x = 4715.5$. The energy efficiency was weighed higher than accuracy, assuming that the controller can deliver the required accuracy. To reduce

the risk, a Mars Sol orbit was chosen over the more energy efficient two day synchronous orbit. Over ten days, this target orbit can provide the spacecraft with nine opportunities to perform EDL with favorable landing-site conditions.

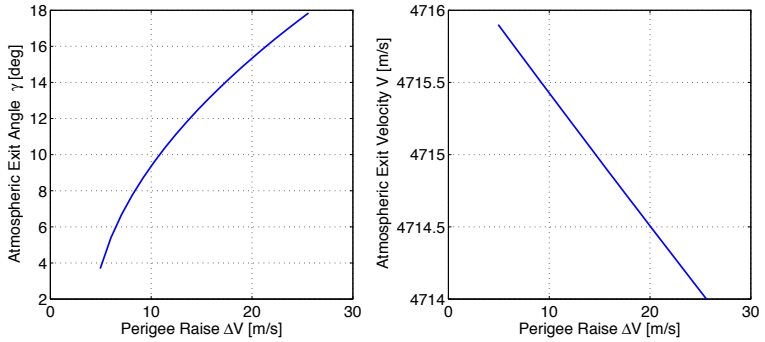

Figure 3-7: Post-aerocapture transfer orbit sensitivity

3-2-4 Target Orbit specifications

The initial choice for a target orbit is a Mars sol orbit, for the reasons discussed in the previous section.The final transfer orbit specifications, as listed in Table 3-1, were used for the sizing of aerocapture and EDL. If the choice of target orbit were to impose unachievable constraints on either of the two atmospheric phases, the design team was planning on updating the target orbit. The target orbit from the Midterm Report was kept; however, the transfer orbits were altered to favor the aerocapture and EDL maneuvers discussed in Section 5-4 (Results: Aerocapture)and Section 5-5 (Results: Entrance, Descent and Landing).

Table 3-1: Reference transfer and target orbit specifications

Design Parameter	Variable	Magnitude	Unit
Transfer Orbit: Post Aerocapture			
Exit velocity	V_{ex}	4715.5	m/s
Exit angle	γ_{ex}	9.08	deg
Eccentricity	e	0.8324	-
Semi major axis	a	20359	km
Apoapsis altitude	r_a	37307	km
Periapsis altitude	r_p	3589	km
Periapsis raise maneuver	ΔV	10.29	m/s
Target Orbit			
Orbital Time	T	24.66	h
Apoapsis altitude	r_a	37307	km
Periapsis altitude	r_p	3589	km
Closest Distance to Mars	h_a	200	km
Semi major axis	a	20448	km
Eccentricity	e	0.8245	-
Transfer Orbit: Pre EDL			
Entrance velocity	V_{ex}	4715.3	m/s
Entrance angle	γ_{ex}	11.55	deg
Eccentricity	e	0.8346	-
Semi major axis	a	20336	km
Apoapsis altitude	r_a	37307	km
Periapsis altitude	r_p	3364	km
Periapsis lowering maneuver	ΔV	13.09	m/s

Chapter 4

Aerodynamic Characteristics

This chapter discusses the aerodynamic model created for use throughout the design process. The methodology behind the aerodynamic model is explained in Section 4-1; it deals with the generation of a computational mesh, the determination of pressures on the aeroshell's surface, and how these contribute to the output aerodynamic coefficients. The limitations of the model and strategies to reduce errors are explained in Section 4-2. Section 4-3 discusses the validity of the model, where it is shown that the model provides reliable results within 6% of values from more accurate Computation Fluid Dynamics (CFD) codes. An analysis of aerodynamic characteristics of the final aeroshell design is discussed in Section 4-4. An investigation into the sensitivity to changes in the design parameters is performed in Section 4-5.

4-1 Methodology

The aerodynamic model used consists of three parts functions: surface geometry generation, calculation of pressure coefficient, and determination of the aerodynamic coefficients.

4-1-1 Surface Geometry Generation

All coordinates in this chapter are in the body-fixed reference frame depicted in Figure 4-1. The tip of the aeroshell is the origin of this reference frame and has coordinates (0,0,0). The X-axis is the symmetry axis of the aeroshell, positive in the rearward direction. The Y-axis was chosen to point in the direction that is considered 'up'. The Z-axis completes the right-handed reference system.

The surface of the aeroshell is a spherically blunted cone; its surface can be broken down in two parts: a spherical section and a cone section. In the model, these two parts are first created separately and are then attached to each other. The location of the transition from sphere to cone is determined from geometry. The x-coordinate of transition (x_t) is determined with Equation 4-1, where R_n is the nose radius and δ_n is cone angle. From the aeroshell tip to this point (the gray area in Figure 4-1), x is increased in millimeter sized steps. For each x-coordinate, the corresponding y- and z-coordinates are calculated using Equations 4-2 to 4-4, which are determined from geometry. θ represents the circumferential location and runs from 0 to 2π.

$$x_t = R_n - R_n \sin \delta_n \tag{4-1}$$

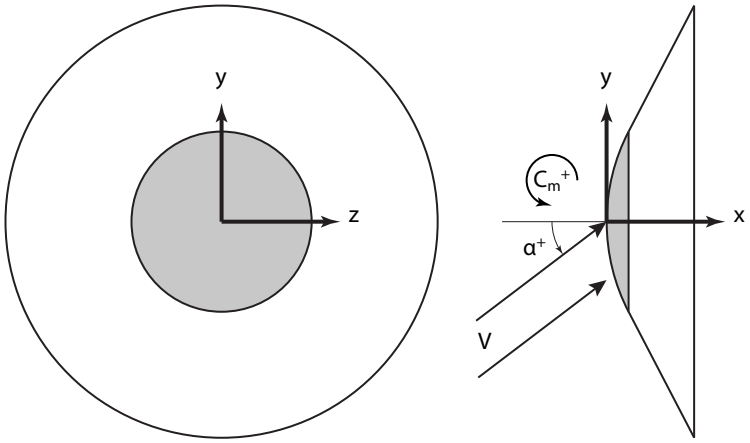

Figure 4-1: Body-fixed system used in this chapter, front view (left) and side view (right).

$$R_{loc} = R_n \sin\left(\cos^{-1}\left(\frac{1-x}{R_n}\right)\right) \tag{4-2}$$

$$y = R_{loc} \sin(\theta) \tag{4-3}$$

$$z = R_{loc} \cos(\theta) \tag{4-4}$$

Because the radius increases linearly with distance from the transition with the spherical section of the aeroshell, the local radius (R_{loc}) at every point in the conical section can be shown to be:

$$\frac{dR}{dx} = \frac{R_{max} - R_t}{\frac{R_{max}}{\tan\delta_n} - x_t} \tag{4-5}$$

$$R_{loc} = x_c \frac{dR}{dx} + R_t \tag{4-6}$$

Using the above methods, a coordinate grid that describes the aeroshell's surface is generated. In order to continue with determining the pressure coefficients as explained in subsection 4-1-2 the surface orientation along the grid has to be determined; this was done by creating two vectors on each grid point. One vector points to the next point in the longitudinal direction and the second vector to the next point in circumferential direction. Using the vector cross product, a third vector is calculated that holds information on the orientation and size of the surface element. This is presented graphically in Figure 4-2, and symbolically in Equations 4-7 to 4-9.

$$\mathbf{r_{1,ij}} = \begin{bmatrix} x_{i+1,j} - x_{i,j} \\ y_{i+1,j} - y_{i,j} \\ z_{i+1,j} - z_{i,j} \end{bmatrix} \tag{4-7}$$

$$\mathbf{r_{2,ij}} = \begin{bmatrix} x_{i,j+1} - x_{i,j} \\ y_{i,j+1} - y_{i,j} \\ z_{i,j+1} - z_{i,j} \end{bmatrix} \tag{4-8}$$

$$\mathbf{S_{ij}} = \mathbf{r_{1,ij}} \times \mathbf{r_{2,ij}} \tag{4-9}$$

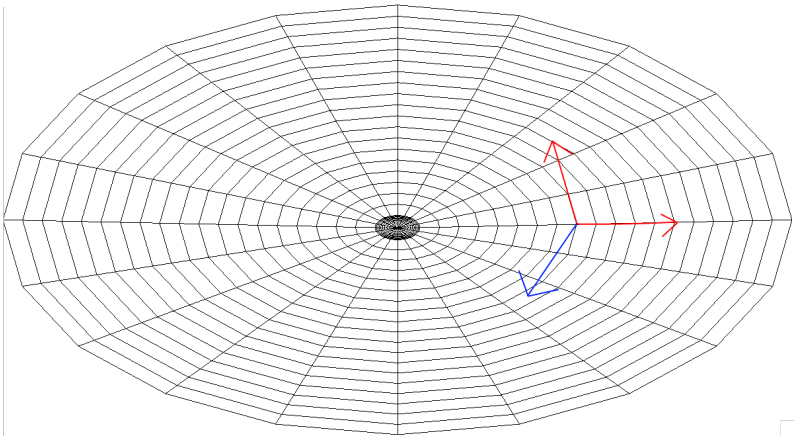

Figure 4-2: Grid used for calculations. The red arrows represent the two vectors used to create the third vector which defines the surface (shown in blue).

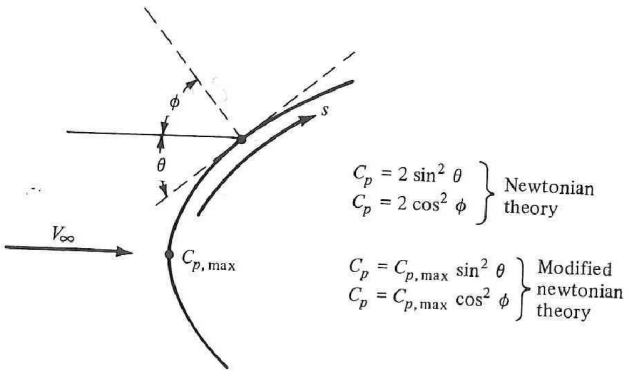

Figure 4-3: Definition of flow orientation [11]

Table 4-1: Effective ratio of specific heats and Mach number dependence of Martian atmosphere, data [13]

$\mathbf{M_\infty}$	22.3	18.3	16.0	12.2	9.4	6.6	2.0
$\boldsymbol{\gamma_{sh}}$	1.0938	1.1010	1.1105	1.1405	1.1800	1.2125	1.3300

.

4-1-2 Pressure Coefficients Calculation

To calculate the pressure coefficients the Modified Newtonian method is used. It is assumed that pressure on the surface is directly related to the orientation with respect to the free stream, as determined from Figure 4-3 and Equation 4-10, from [11].

$$C_p = C_{p,max} \sin^2 \theta \tag{4-10}$$

The maximum pressure coefficient, $C_{p,max}$, is related to the freestream Mach number, M_∞, and the ratio of specific heats, γ_{sh}, through Equation 4-11, as found in [12].

$$C_{p,max} = \frac{2}{\gamma_{sh} M_\infty^2} \left(\left(\frac{(\gamma_{sh}+1)^2 M_\infty^2}{4\gamma_{sh} M_\infty^2 - 2(\gamma_{sh}-1)} \right)^{\frac{\gamma_{sh}}{\gamma_{sh}-1}} \left(\frac{1-\gamma_{sh}+2\gamma_{sh} M_\infty^2}{\gamma_{sh}+1} \right) - 1 \right) \tag{4-11}$$

The ratio of specific heats is not constant throughout all flight conditions; there is a dependence on the Mach number. An approximate relation was established based on data from [13]. This data, repeated in Table 4-1, is used in an interpolation algorithm that outputs an effective ratio of specific heats for an input Mach number.

4-1-3 Determination of Aerodynamic Coefficients

Once the surface orientation and pressure distribution are known, it is possible to perform a numerical integration to determine the aerodynamic coefficients. The contribution of every surface element is summed and divided by the aeroshell reference area, which results in a three-dimensional vector. This vector represents the coefficient of resultant force, which can be decomposed into two vectors: one parallel to the velocity vector and the other perpendicular to it, representing the drag and lift coefficients respectively. This is symbolically denoted in Equation 4-12, 8-25, and 8-23.

$$\mathbf{C_{res}} = \frac{\sum\sum C_{p,ij} \mathbf{S_{ij}}}{S_{ref}} \tag{4-12}$$

$$C_D = \frac{\mathbf{V} \cdot \mathbf{C_{res}}}{|\mathbf{V}|} \tag{4-13}$$

$$C_L = \mathbf{C_{res}} - C_D \frac{\mathbf{V}}{|\mathbf{V}|} \tag{4-14}$$

The accuracy of this model drastically drops when the Mach number decreases below approximately 5, as the assumptions of the Newtonian method are no longer valid. A correction to this effect is introduced in Section 4-2.

Similarly to the computations of force coefficients, moment coefficients were calculated using a numerical integration over the complete aeroshell surface. As moments are calculated about the center of gravity, the arm of a surface element is computed first with Equation 4-15.

$$\mathbf{r_{ij}} = \begin{bmatrix} x - x_{cg} \\ y - y_{cg} \\ z - z_{cg} \end{bmatrix} \tag{4-15}$$

The moment arm and force on every surface element are multiplied in a cross product, resulting in an elemental moment contribution. After summing over the total area, the moment is rendered non-dimensional by dividing by the total surface area (S_{ref}), and the diameter of the aeroshell ($l_{ref} = d$). This calculation, shown symbolically in Equation 4-16, produced a moment about the three axes.

$$\mathbf{C_M} = \frac{\sum\sum C_{p,ij}\mathbf{S_{ij}} \times \mathbf{r_{ij}}}{S_{ref} l_{ref}} \tag{4-16}$$

4-2 Limitations of Model

The assumptions related to Newtonian flow introduce limitations to the model, which influence the accuracy. The problems regarding supersonic velocities are discussed first, followed by the issues involved with the calculation of the moment coefficients.

4-2-1 Supersonic Speeds

Modified Newtonian theory, as used to calculate pressure coefficients, is only applicable to hypersonic flows. In accordance, the results obtained during verification and validation of the model differed significantly from a reference study in the low Mach regime. It was found that the lift and drag coefficients computed dropped faster in the model than in the reference study. To fix the issue, a scaling of the Mach number was implemented. When the Mach number input for the model is lower than 5, it is corrected by using Equation 4-17. This relation was established through trial and error, it was tuned until the error was in an acceptable range (±6%, as seen in Section 4-3).

$$M = 1.5 + 0.7M_{\infty} \tag{4-17}$$

4-2-2 Moment Coefficients

Calculating moment coefficients with the Newtonian method does not provide reliable results. That is because there are effects along the edge of the aeroshell that cannot be simulated in Newtonian flow [13]. The influence on moment coefficients is significant due to the distance from center of gravity. Unfortunately a lack of resources for the project prevents the creation of a new model dedicated moment coefficients. The results obtained are thus used in the design process. For continued development, improving accuracy of this aspect is recommended.

4-3 Verification and Validation

The accuracy of the model had to be confirmed before the results could be trusted and be used in the design process; this was done by replicating tests and simulations from literature. This section shows the result of that process.

A study [13] on the Mars Pathfinder and its 70 degree aeroshell was used for validation, as this study was very clear on the corrections that were performed for the Martian atmosphere. It is noted that the model's ability to determine a correct L/D had already been demonstrated in the Midterm Report [4], and thus the emphasis was on determining the validity of the model on the Martian atmosphere. Characteristics of the Pathfinder aeroshell can be found in Table 4-2. The result of this validation step is shown in Table 4-3

In Table 4-3 C_L and C_D match very closely to the Pathfinder study, with an error of at most 6 %, which is considered acceptable. For Mach numbers of 6.6 and above, the results of the Newtonian

Table 4-2: Characteristics of Mars Pathfinder Aeroshell

Characteristic	**Pathfinder**
Nose Radius [m]	0.6625
Cone Angle [*deg*]	70
Maximum Radius [m]	1.325
Mach Range [-]	1.9-39.3

Table 4-3: Simulation results comparison to [13]

α [*deg*]	$\mathbf{M_\infty}$	$\mathbf{C_L}$ [13]	$\mathbf{C_L}$ **DSE03**	$\mathbf{C_L}$ **error [%]**	$\mathbf{C_D}$ [13]	$\mathbf{C_D}$ **DSE03**	C_D **error [%]**
0	22.3	0	0	-	1.716	1.722	0.36
0	18.3	0	0	-	1.715	1.717	0.11
0	16	0	0	-	1.712	1.711	-0.06
0	12.2	0	0	-	1.680	1.694	0.79
0	9.4	0	0	-	1.636	1.669	2.05
0	6.6	0	0	-	1.597	1.634	2.28
0	2	0	0	-	1.342	1.409	4.99
5	22.3	-0.131	0.130	-1.11	1.679	1.705	1.58
5	18.3	-0.132	0.130	-2.28	1.676	1.700	1.45
5	16	-0.133	0.129	-3.41	1.671	1.694	1.38
5	12.2	-0.136	0.128	-6.01	1.656	1.677	1.24
5	9.4	-0.132	0.126	-4.69	1.622	1.653	1.88
5	6.6	-0.127	0.123	-3.03	1.584	1.617	2.11
5	2	-0.105	0.106	0.95	1.333	1.395	4.65
11	22.3	-0.269	0.276	2.72	1.579	1.641	3.94
11	18.3	-0.269	0.275	2.37	1.575	1.636	3.90
11	16	-0.270	0.274	1.82	1.571	1.631	3.79
11	12.2	-0.270	0.272	0.48	1.558	1.614	3.57
11	9.4	-0.271	0.268	-1.12	1.542	1.591	3.14
11	6.6	-0.269	0.262	-2.62	1.523	1.557	2.23
11	2	-0.225	0.226	0.44	1.295	1.342	3.63

method were not amended. However, the error for Mach 2 was close to 20 %. For that reason, the correction explained in Section 4-2 was implemented, which reduced the error to the acceptable range.

The pitch moment coefficients have been compared to [14]; the comparison can be seen in Figure 4-4. Simulated and calculated values do differ by a significant margin (more than 6%), the cause of which was explained in Section 4-2. However, the behavior of the moment coefficient with changing Mach number and angle of attack is similar.

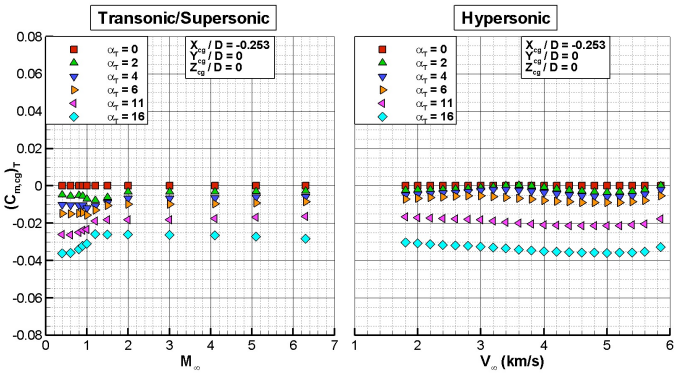

(a) Phoenix moment coefficient, from [14]

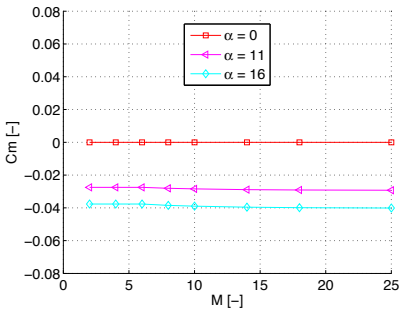

(b) Computed phoenix moment coefficient

Figure 4-4: Comparison of Phoenix lander moment coefficient

4-4 Aerodynamic Properties of the Aeroshell

The aerodynamic behavior of final design is investigated. For the Mach numbers and angles of attack encountered during aerocapture and entry, the aerodynamic coefficients are computed and shown in Figure 4-5. As discussed in Section 7-1, angles of attack beyond $30deg$ are not expected, thus C_L and C_D are investigated for that range.

All coefficients are almost constant above approximately Mach 6 and move quickly toward zero below Mach 5. This behavior can be attributed to Equation 4-11 which has an asymptote for $M_\infty \to \infty$ but changes rapidly when M_∞ is small. Lift and drag coefficient reach values of 0.36 and 1.36 respectively for the targeted angle of attack. The slope of the graph of coefficient of drag versus angle of attack is at first slightly negative and gradually curves down more as angle of attack increases. That is caused by the decreasing amount of surface area which impacts the flow. From the plot of C_M versus α, it can be observed that the slope is negative between angles of attack of 0 to about $30deg$. This means that the aeroshell is statically stable in that range. Beyond $35deg$ the slope is distinctly positive, which indicates instability.

4-5 Sensitivity Analysis

In this section the effects of changing the maximum cone radius and cone angle on the aerodynamic properties are discussed to establish how the design affects the aerodynamic coefficients.

4-5-1 Maximum Radius

Displayed in Figure 4-6 are the results of changing the maximum cone radius. It can be seen that the coefficients of lift and drag slightly decrease with an increase of cone size; this is because a higher pressure coefficient is associated with surfaces that are more perpendicular to the oncoming

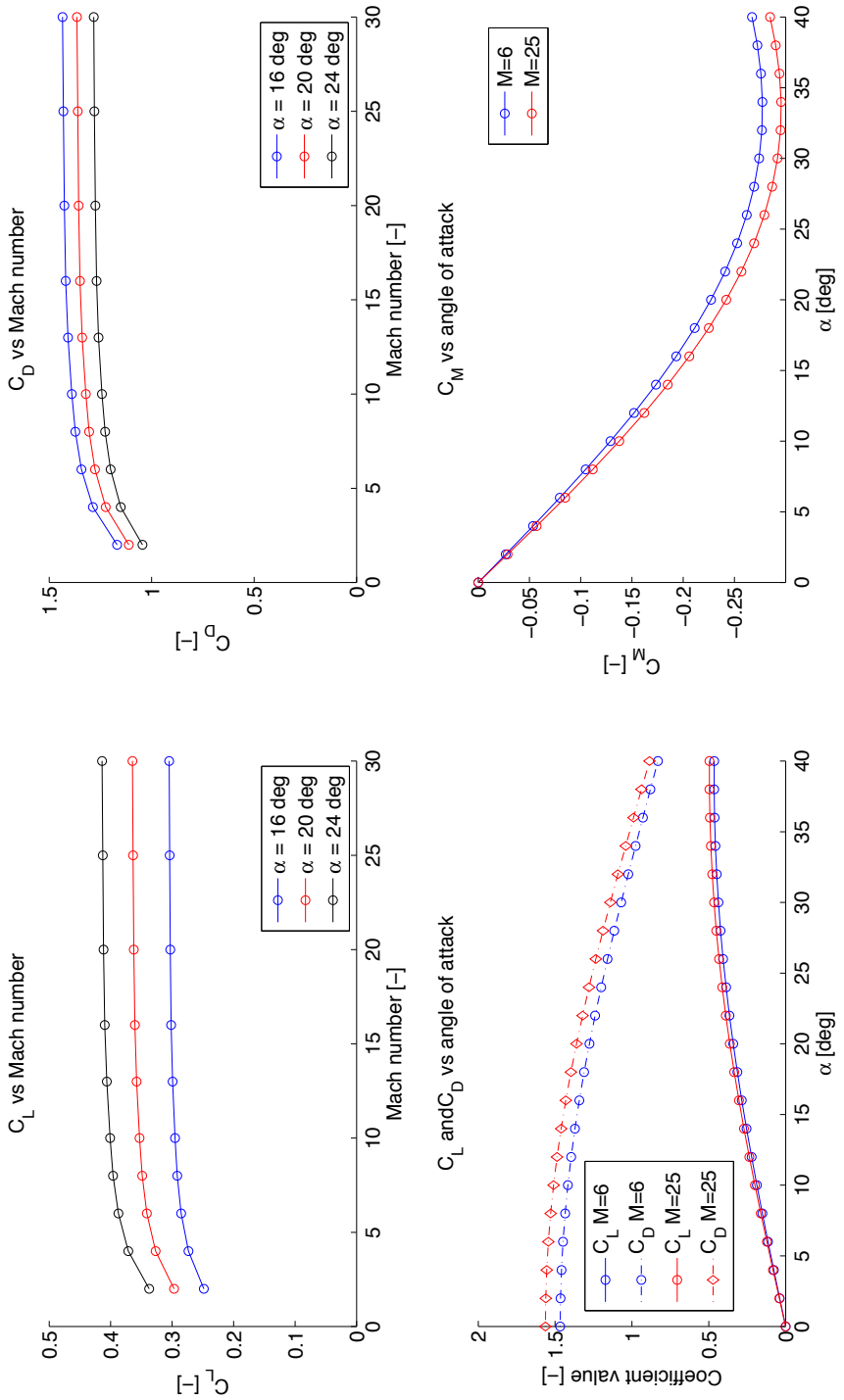

Figure 4-5: Aerodynamic Coefficients of the Final Design

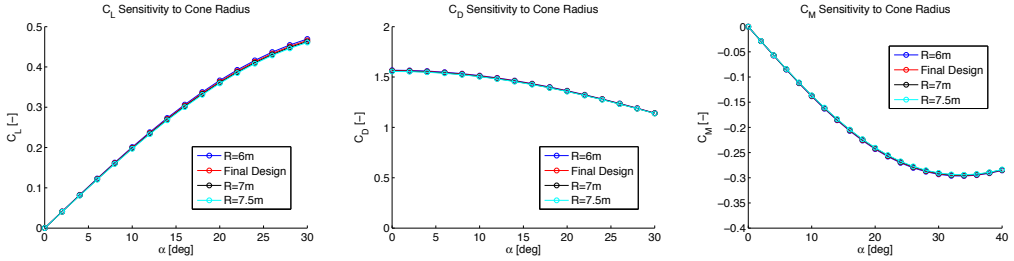

(a) C_L Sensitivity **(b)** C_D Sensitivity **(c)** C_M Sensitivity

Figure 4-6: Sensitivity of the aerodynamic coefficients to changing cone radius

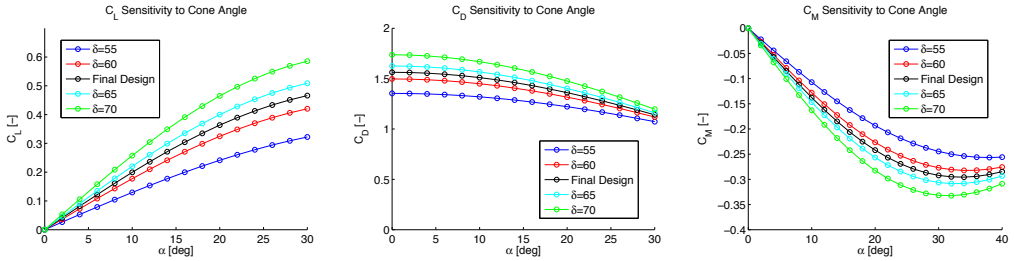

(a) C_L Sensitivity **(b)** C_D Sensitivity **(c)** C_M Sensitivity

Figure 4-7: Sensitivity of the aerodynamic coefficients to changing cone angle

flow. The parts with the highest pressure coefficients are thus located on the nose. With an increase in cone size, the influence of the sphere becomes smaller, hence the reduction in lift and drag coefficients. These effects are very small as the surface area of the spherical part is small if compared to the surface of the cone. Oppositely, the forces are more significantly increased when cone radius is increased, due to the larger increase in surface area. When the moment is expressed per unit of dynamic pressure (as $C_P S_{ref} l_{ref}$), the effect of increase in radius is even more pronounced due to the fact it has a cubical relationship with R_{max}.

4-5-2 Cone Angle

The effect of changing cone angle on the aerodynamic coefficients is presented in Figure 4-7. All coefficients increase in magnitude with a higher cone angle. As the cone surface is angled more perpendicular to the flow with higher cone angles, lift and drag increase due to higher pressure at the surface. The range of angle of attack where the aeroshell is stable, changes with the cone angle. The lowest computed value of C_M of the final design occurs at $\alpha = 34deg$, for a cone angle of $70deg$ it is found at $\alpha = 32deg$, and for a $55deg$ cone at $\alpha = 38deg$

Chapter 5

Atmospheric Trajectory Design

This chapter focuses on implementing the aerodynamic model in a trajectory analysis that provides information on the feasibility of the aerocapture and the EDL phases, together with respective final reference trajectories to be followed by the control system. After a brief discussion of the atmospheric model the simulation model is explained in more detail, followed by discussion of its limitations. Lastly, the reference trajectory for aerocapture and EDL are presented along with a risk and sensitivity analysis.

5-1 Atmospheric Model

The information regarding the planet was collected via the Mars fact sheet available on the NASA website [15]. This provided the following planetary information: the radius, mass, volume, gravitational parameters and escape velocity. The Mars atmosphere is taken to end at an altitude of 130 km from the surface level, based on the information gathered from [16] and [17]. It is assumed that the density decreases exponentially from surface level [18], with a density at the surface of 0.016 kg/m^3 and a scaling height of 10 km [18]. The pressure and temperature are then reproduced based on the tables provided by [17] and are represented in Figure 5-1. This data is based on average conditions, even though the Martian atmosphere is highly sensitive to seasonal changes [18].

5-2 Methodology

This section elaborates on the simulation model that provides information on the entrance corridor for both EDL and aerocapture. This model relies on linearizing the motion at each time increment so as to apply a predictor scheme on the forward integration of the Equations of Motion (EOM).

5-2-1 Assumptions

For the forward integration in time, a set of assumptions were implemented to obtain approximate solutions for the given aerocapture and EDL phases.

PA1 Mars is assumed to be non rotating, neglecting centripetal and Coriolis effects during motion.
PA2 The time step is assumed to be small enough such that linearization errors can be neglected.

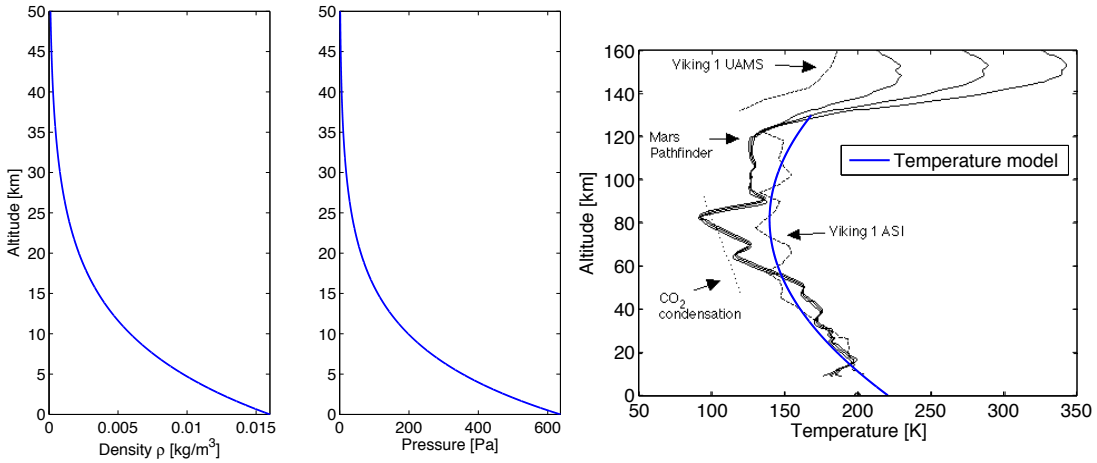

Figure 5-1: Standard Martian atmosphere model

PA3 There are no fluctuations in the Martian atmosphere, and for each time increment atmospheric conditions can be assumed to be constant.
PA4 The mass of the vehicle is assumed to be constant.
PA5 The spacecraft is entering with the nominal entrance conditions.

5-2-2 Equations of Motion

The EOM are based on Figure 5-2 and the derivations are presented in [19]. The variables used in the following equations are presented in the nomenclature. The flight path angle γ was defined positive above the local horizon.

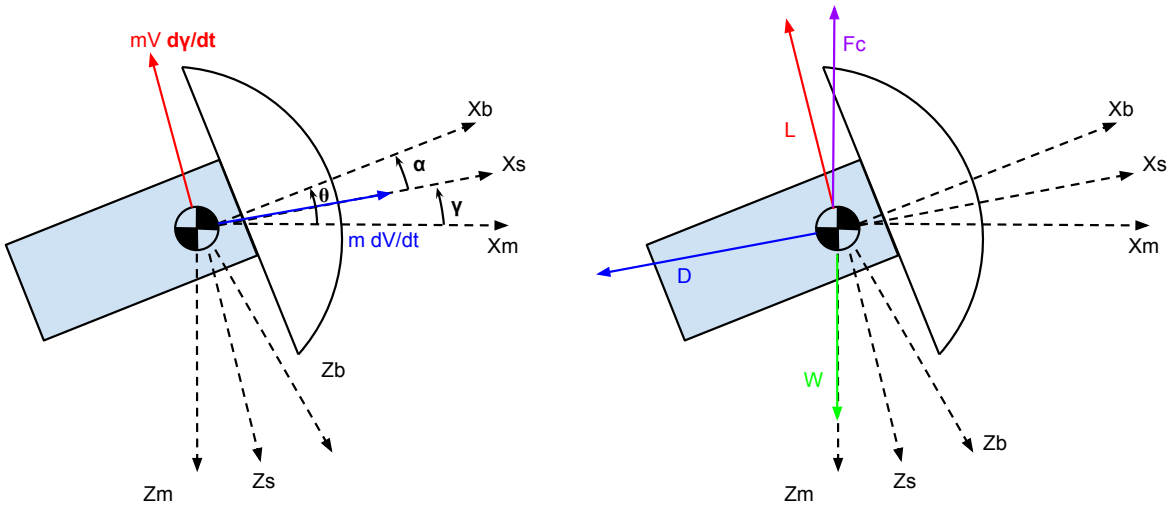

Figure 5-2: Free body diagram for an (re)entry vehicle

The equations of interest are:

$$\frac{dV}{dt} = \frac{dV}{dh}\frac{dh}{dt} = -\frac{D}{m} - g\sin\gamma \tag{5-1}$$

$$V\left(\frac{d\theta}{dt} + \frac{d\gamma}{dt}\right) = \frac{L}{m} - g\cos\gamma \tag{5-2}$$

The associated kinematic equations are:

$$\frac{dh}{dt} = V sin\gamma \qquad (5\text{-}3) \qquad\qquad \frac{d\theta}{dt} = -\frac{V\cos\gamma}{R_m + h} \qquad (5\text{-}4)$$

5-2-3 Entry and Simulation conditions

The model relies on input data from the aerodynamic analysis found in Section 4-4 (Aerodynamic Properties of the Aeroshell) and is set up for simulation conditions mentioned in the following list. For the aerocapture and EDL phases further constraints are added in terms of entrance velocity, entrance angle, target conditions.

- **Time Step:** A time step of $dt = 0.1s$ was chosen to integrate forward in time. Atmospheric Conditions are constant during this time interval.
- **Entry Height:** The entry height was set to be at $130km$, in accordance with the atmospheric model presented in Section 5-1 (Atmospheric Model).
- **Entry Parameters:** The entry parameters for aerocapture ($V = 7000m/s$, $\gamma = -11.05deg$) and EDL ($V = 4715.3m/s$, $\gamma = -11.55deg$) are set by the target orbit analysis presented in Chapter 3.
- **Further Entry Conditions:** As the model relies on linearization the initial variations are assumed to be small ($\frac{d\gamma}{dt} \approx 0$, $\frac{dV}{dt} \approx 0$)
- **Ballistic Coefficient:** For the initial sizing a ballistic coefficient C_B of 63.77 is used.
- **Lift Coefficient:** Lift coefficient C_L is estimated to be 0.427.
- **Target Conditions:** The target conditions are specified by the respective mission targets (Aerocapture: exit conditions, EDL: target box).
- **Constraints:** The constraints on the variation simulation results are determined by the requirements identified in Section 1-3.

5-2-4 Simulation Logic

The logic of information during each time interval is visualized in Figure 5-3, and will be used as a basis to explain each step of the model. The model relies on linearization to predict conditions for the given time interval. Based on predicted conditions an estimate is made for the updated velocity and flight path angle at the end of the time step. The outputs serve as the inputs for the subsequent box.

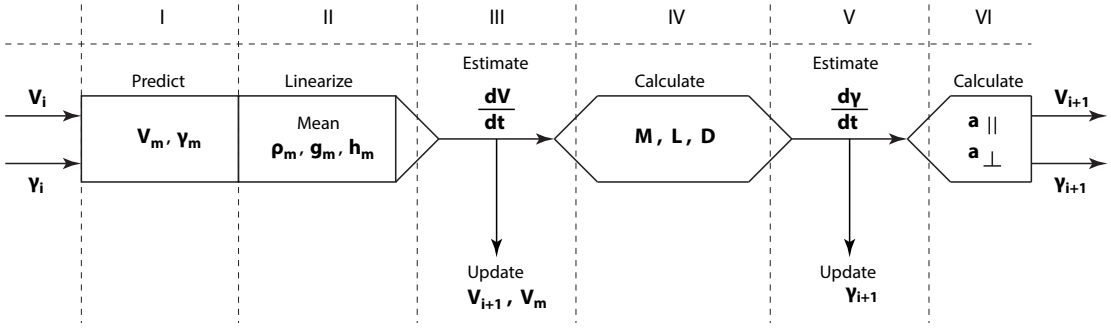

Figure 5-3: Predictor corrector algorithm

Part I To minimize errors for the a given interval, the expected average velocity V_m and flight path angle γ_m are predicted by means of linearization (Equation 5-5 and Equation 5-6). These predicted values are used in the equations of motion to update the actual velocity loss over the time step dt.

$$V_m = V_i + \left.\frac{dV}{dt}\right|_i dt \quad (5\text{-}5) \qquad \gamma_m = \gamma_i + \left.\frac{d\gamma}{dt}\right|_i dt \quad (5\text{-}6)$$

Part II Given the predicted conditions the mean atmospheric conditions are calculated using Equation 5-7 to Equation 5-12.

$$dh = V_m \, sin\gamma_m \, dt \quad (5\text{-}7)$$

$$h_m = h_i + \frac{dh}{2} \quad (5\text{-}8)$$

$$r_m = r_i + \frac{dh}{2} \quad (5\text{-}9)$$

$$g_m = \frac{GM}{r_m} \quad (5\text{-}10)$$

$$T_m = T(h_m) \quad (5\text{-}11)$$

$$\rho_m = \rho(h_m) \quad (5\text{-}12)$$

Part III Combining the outcome of Part I and Part II the velocity loss can be estimated based on the following idea: the equations of motion are rewritten in the following form (Equation 5-14) and a matching $\left.\frac{dV}{dt}\right|_{i+1}$ that satisfies both sides of the equation is determined.

$$\left.\frac{dV}{dt}\right|_{i+1} = -\frac{D_{i+1}}{m} - g_m \, sin\,\gamma_m \quad (5\text{-}13)$$

$$\left.\frac{dV}{dt}\right|_{i+1} = -\frac{\frac{1}{2}\rho_m \left(V_i + \left.\frac{dV}{dt}\right|_{i+1}\right)^2 C_D S_{ref}}{m} - g_m \, sin\,\gamma_m \quad (5\text{-}14)$$

Given this relation the velocity at the end of the time increment can be obtained together with an update on the average velocity V_m.

$$V_{i+1} = V_i + \left.\frac{dV}{dt}\right|_{i+1} dt \quad (5\text{-}15)$$

$$V_m = V_i + \frac{1}{2} \cdot \left.\frac{dV}{dt}\right|_{i+1} dt \quad (5\text{-}16)$$

Part IV The next step in the model is the calculation of Mach number M_{i+1} lift L_{i+1}, drag D_{i+1} as well as an estimate on the heat flux $\dot{q}$ in accordance with the Equations 5-17 to 5-20. The heat flux was estimated based on the Sutton-Graves heat flux Equation 5-20. The coefficients were found in [20] and [21] along with the nose radius of $R_N = 5.41m$. The heat flux calculations are refined in Chapter 6 (Thermal Protection System Design).

$$M_{i+1} = \frac{V_{i+1}}{\sqrt{\gamma_{sh}\bar{R}T_m}} \quad (5\text{-}17)$$

$$L_{i+1} = \frac{1}{2}\rho_m V_m^2 S C_L \quad (5\text{-}18)$$

$$D_{i+1} = \frac{1}{2}\rho_m V_m^2 S C_D \quad (5\text{-}19)$$

$$\dot{q}_{i+1} = 1.9027\,10^{-4}\frac{\sqrt{\rho_m}}{\sqrt{R_N}}V^{3.15} \quad (5\text{-}20)$$

Part V To update the flight path angle accordingly, the initial idea was to also apply a semi grit search. This being too time consuming, the linearization approach (Equation 5-21) was preferred.

$$\left.\frac{d\gamma}{dt}\right|_{i+1} = \frac{L_{i+1}}{mV_m} - \left(\frac{g_m}{V_m} - \frac{V_m}{r_m}\right) cos\gamma_m \quad (5\text{-}21)$$

$$\gamma_{i+1} = \gamma_i + \left.\frac{d\gamma}{dt}\right|_{i+1} \quad (5\text{-}22)$$

Part VI The final step is to obtain information on the acceleration parallel to velocity $a_{\parallel}$ and perpendicular to velocity $a_{\perp}$ to assure that maximum loads on the humans are not exceeded.

$$a_{\parallel} = -\frac{D_{i+1}}{m} - g_m \, sin y_{i+1} \tag{5-23}$$

$$a_{\perp} = \frac{L_{i+1}}{m} - \left(g_m - \frac{V_m^2}{r_m}\right) cos\gamma_{i+1} \tag{5-24}$$

$$a_{total} = \sqrt{a_{\parallel}^2 + a_{\perp}^2} \tag{5-25}$$

5-2-5 Updates to the Model

To optimize the model a set of updates [**UP**] was included that was used to refine the analysis and provide more reliable reference trajectories.

UP1 In Section 4-4 (Aerodynamic Properties of the Aeroshell) it was explained that the aerodynamic coefficients change with the Mach number. An interpolation scheme was included to provide a better estimate of these coefficients throughout the trajectory.

UP2 To provide further information for the TPS sizing, ambient conditions before and after the bow-shock were estimated.

UP3 Entrance corridor limitations caused by skip out and deceleration requirements were included.

UP4 The trajectory was optimized with respect to the target conditions, by varying the angle of attack at certain critical points in the trajectory. This is discussed further in Section 5-5 (Results: Entrance, Descent and Landing).

UP5 Instead of applying step inputs on the angle of attack, a ramp input of $5s$ was used to reach the new attitude.

5-3 Limitations of Model

A set of limitations was identified that limit the overall accuracy of the model. Limitations mitigation strategies are mentioned for further research.

Step Size and Computing Power The model relies on linearization to predict conditions for the integration of the EOM. This limitation was visualized in Figure 5-5 by showing the difference between the predicted velocity over time increment and the actual one that stems from the calculation. The error generated is related to the step size of the simulation and can be mitigated by decreasing the step size; a finer discretization also allows for a better timing in maneuvers allowing a better optimization process. The issue is that the computing power available sets a limit to the precision that the results of the model can achieve. To show the impact on the resolution an EDL trajectory analysis was performed with the same simulation conditions, but for two different step sizes: $dt = 0.1s$ and $dt = 0.01s$. The comparison is shown in Figure 5-4 along with the relative Mach number error. The error is acceptable, yet accumulates over a full scenario.

Aerodynamics in the Supersonic Phase As stated in the aerodynamics section the accuracy of the modified Newtonian Method decreases in the supersonic regime. Although scaling is applied to the coefficients in supersonic flow, the reliability of the model in the final stage of the EDL decreases.

Atmospheric Fluctuations The simulation assumes no fluctuations in density, temperature and pressure in the atmosphere. However, research [18] indicates that large variations in the Martian atmosphere are possible. The GNC must assure that the model works within the given atmospheric variations.

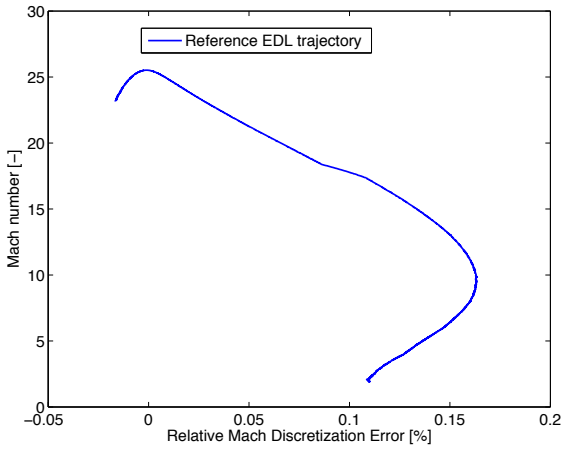

Figure 5-4: Discretization error for Mach between simulation with $dt = 0.1s$ and $dt = 0.01s$

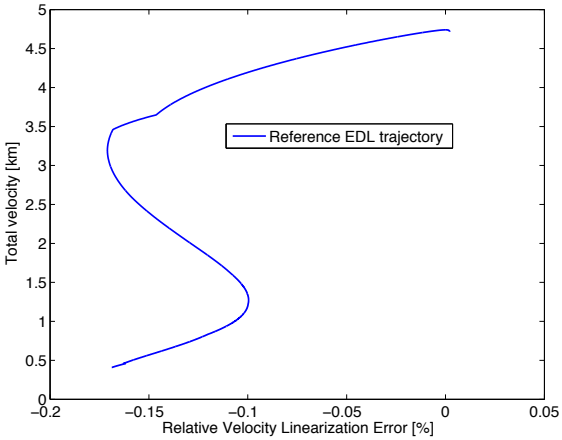

Figure 5-5: Linerarization error on velocity

Smart Control Algorithm The simulation is unable to predict whether altering the trajectory would be beneficial for target conditions. Only a full simulation run shows the effects of altering the simulation conditions, resulting in a more extensive optimization process.

Verification

During the programming process the model was tested for a range of inputs to determine if the outputs where with accordance to the expected results. The first finding was related to the fact that skipping was modeled incorrectly, resulting in discontinuities in the flight path angle. This problem was tackled by conditioning the equations for positive and negative altitude gain. This was confirmed by simulating shallow flight path trajectories and checking if the simulation would predict a smooth flight path angle change. Furthermore, the outcome of each trajectory was checked for their first derivatives to assure that no jumps are present throughout the trajectories. Another method was the comparison between the analytic solutions presented in the Midterm Review and the simulation results in this section. Similar relations were found and the overall shape of the analytical solutions could be reproduced.

Validation

In the Phase 1 study [10] the HYPAS analytical closed-loop guidance algorithm was used to provide information on the aerocapture and EDL maneuvers. By means of running the DSE03 simulation for the same conditions the simulation could be validated. A simulation with similar conditions to the 23m HIAD and a mass of 80 tons was performed and the two graphs were compared. A qualitative comparison was performed because the information in the Phase 1 study is only available in form of graphics. The results are compared with Figures 5-6 and 5-7. The model follows the overall trajectory profile closely and descends to a similar altitude. At the beginning and end of the main deceleration process there is a small discrepancy as the Phase 1 study follows a more horizontal path.

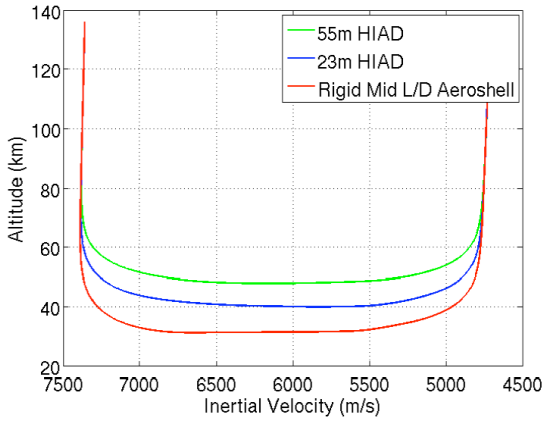

Figure 5-6: Phase 1: aerocapture maneuver [10]

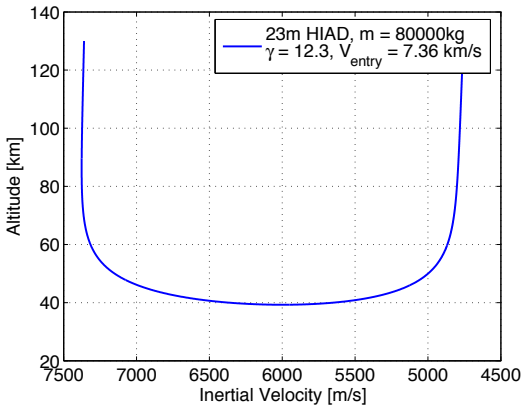

Figure 5-7: DSE03 aerocapture validation

5-4 Results: Aerocapture

The results are specified after the entrance corridor was established and a short risk mitigation was performed within the given entrance corridor.

5-4-1 Entrance Corridor

The aerocapture trajectories were constrained by three limit trajectories which for different combinations of maximum lifts still result in the required exit conditions . All three trajectories are designed for an Entrance speed of $7000m/s$ and such that the exit velocity of $4715m/s$ is met. The three different trajectories are displayed in Figure 5-8 and are as follows:

AC1 The first physical limitation for entry requires full lift up throughout the whole aerocapture maneuver. This mission allows the deepest penetration of the atmosphere by entering with the steepest possible entrance angle $\gamma_{en} = -11.56$ and uses lift assist to achieve the skip-out. The deceleration takes place around the lowest point of trajectory, where the atmosphere is denser. Furthermore, this trajectory results in the least time in the atmosphere when compared to AC2 and AC3, but features the highest TPS loading and maximum g-loads. This mission has the steepest exit flight path angle.

AC2 The second limitation is set by a reference mission that flies using negative lift for the whole maneuver. This mission enters with the shallowest possible flight path angle ($\gamma_{en} = -9.55$) resulting in a higher altitude where the spacecraft decelerates. This mission spends the longest time in atmosphere, resulting in the highest heat load yet having the lowest heat flux. Contrary to AC1 this option will result in the most shallow injection angle for the transfer orbit.

AC3 This option combines AC1 and AC2 by using both full lift and full lift down. Entering with $\gamma_{en} = -10.60$ it is required to apply full lift up until perigee, followed by a lift reversal and full lift down from perigee on. This mission is a compromise for the TPS system, having both a lower heat flux and heat load than AC1 and AC3.

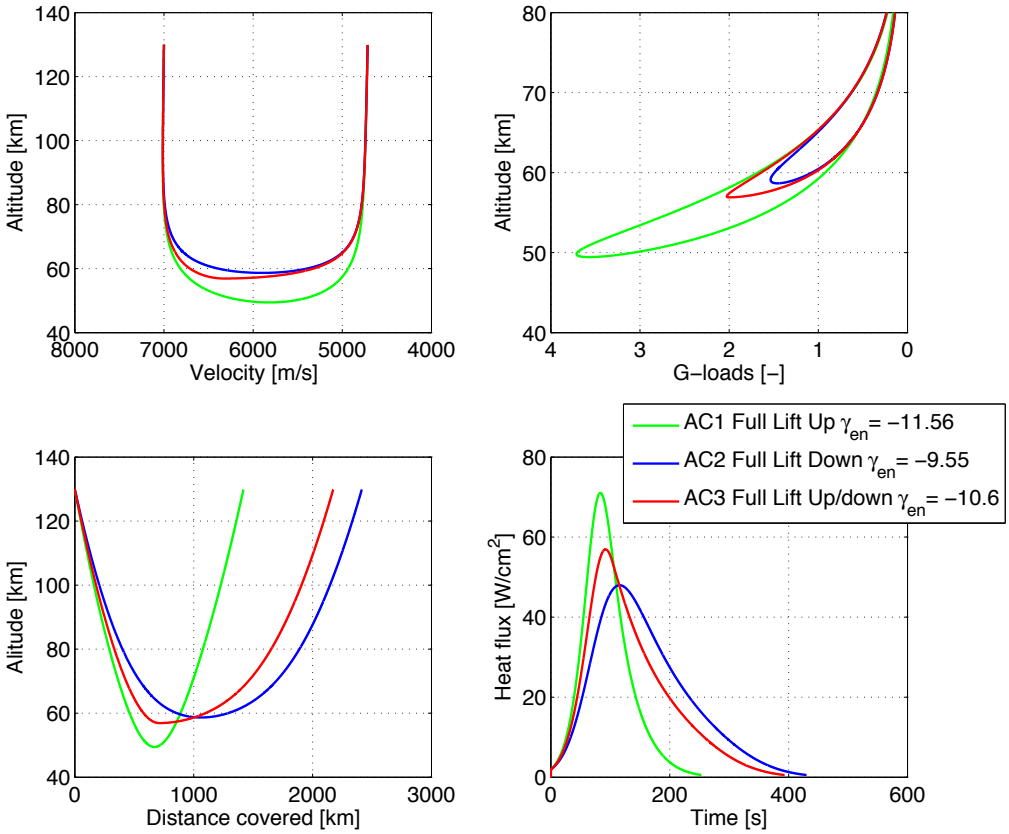

Figure 5-8: Entrance corridor for the aerocapture maneuver

5-4-2 Sensitivity Analysis

The three factors that are of interest to the trajectory sensitivity analysis are the mass and area of the aeroshell along with varying entrance conditions. The most important relations are shown in Figure 5-9 and are explained in the following list:

- **Change in Surface Area -** An increase in the surface area results in a higher lift and drag generation capabilities, resulting a faster deceleration process and less penetration in the atmosphere. This is beneficial for the TPS system in terms of heat flux. However, increasing the surface area of the aeroshell comes at the cost of an increase in mass, as the supporting structure has to cope with the higher shear and normal loads. Decreasing the surface area puts higher loads on the already critical design of the TPS. These relationships are given as the blue lines in Figure 5-9.
- **Change in Mass -** With an increase in mass the system is forced to lose more energy; the spacecraft has to stay longer in the atmosphere to achieve the required dissipation of energy. Following EOM Equation 5-1 and Equation 5-2 higher mass would result in lower deceleration loads considering that a higher mass results in a higher ballistic coefficient. In terms of controllability a higher mass will give the spacecraft more momentum and thus less and slower control on its trajectory. This limits the controller in actively influencing the flight path angle.
- **Variations in Aerocapture Entrance Speed -** The target orbit conditions are designed such

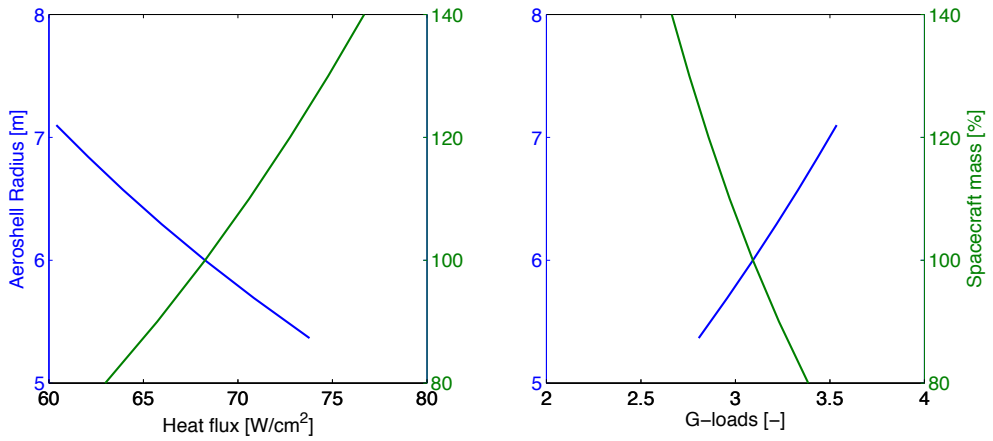

Figure 5-9: Change of heat flux with change in area and mass

that the aerocapture maneuver can assure the atmospheric exit conditions. Hence variations in the entrance conditions have to be fully compensated by the aerocapture maneuver. A higher entrance velocity results in a steeper penetration of the atmosphere so to meet exit energy conditions. This increases the deceleration loads.

5-4-3 Risk Analysis

The entrance corridor defines the physical limits for the system, thus the final trajectories requires a safety margin to decrease the risks of exceeding the limits. Section 3-2 (Post Aerocapture Transfer and Target Orbit Characterization) showed that the target orbit is very sensitive to the exit conditions, allowing for very little error. The following list entails the most critical risk related to the limits of the entrance corridor.

AC1 Since the aerocapture trajectory relies on lift assistance to manage skip out, variations in the atmosphere result in failure to provide enough lift to meet the exit conditions. Too little lift results in a lower exit velocity unfavorable to reach the apocenter of the target orbit. Furthermore, due to the fact that the EDL target box is constrained in its position to the perigee of the target orbit, there is a requirement on the distance covered by the aerocapture maneuver. Insufficient lift results in a longer covered distance, thus shifting the perigee of the target orbit and risking that the target box cannot be reached by the EDL phase. Not meeting the requirements for the target orbit has critical consequences for the mission. Lastly, this mission requires the most advanced TPS, making it a high operational risk. Any damages to the TPS may render it unsafe for use in EDL.

AC2 The full lift down mission risks not generating enough negative lift to meet the exit conditions. Contrary to AC1 this trajectory can leave the atmosphere at too high velocities, risking that the spacecraft escapes from Mars. In line with AC1, however, this trajectory risks not achieving the desired distance covered during aerocapture with critical consequences for mission success. This mission has less constraints on the TPS in terms of heat flux, however the system has to account for increased heat loading and thus putting payload insulation at higher risk.

AC3 Option AC3 shares the risk in terms of the accuracy with the two previous option AC1 and AC2. The operational risk on the TPS is lower, as this trajectory compromises between heat flux and heat load.

Risk Mitigation Limiting the risk along with decreasing their likelihood was accomplished by a set of safety margins. The first one relates to the entrance flight path angle: the final reference mission requires a margin of $\pm 0.5°$ for the entrance angle from the limits set by AC1 and AC2.

Table 5-1: Reference aerocapture trajectory specifications

Design Parameter	Variable	Magnitude	Unit
Entrance velocity	V_{en}	7000	m/s
Exit velocity	V_{ex}	4715.7	m/s
Entrance angle	γ_{en}	-11.05	deg
Skip out margin		$\pm$ 0.5	-
Exit angle	γ_{ex}	9.08	deg
Angle of attack	α	-16	deg
Maximum G-Load	g_{max}	3.3	-
Time	t	271.3	s
Minimum altitude	h_{min}	51.5	km
Groundtrack distance	R	1520.5	km
Maximum heat flux	$\dot{q}$	68.13	W/cm^2
Total heat load	q	6214.2	J/cm^2

The second safety margin is set by the requirements on the angle of attack. Since trajectories requiring full lift cannot compensate a lower than nominal density, these mission are avoided and are flown at lower angle of attack. Contrary to this the TPS requires a larger angle of attack to decrease the heat flux [22], such that the final trajectory flies at a high angle of attack, yet with a safety margin of $\alpha_{nominal} = 0.75\ \alpha_{max}$.

5-4-4 Final Trajectory

The final chosen trajectory is AC1, including the safety margins discussed in the risk mitigation section. This decision is because analysis of the TPS showed that heat load should be minimized. Hence the mission with the least time in the atmosphere is chosen. Table 5-1 shows the most important design parameters of the final reference trajectory.

5-5 Results: Entrance, Descent and Landing

After a short description of the EDL entrance corridor, a risk analysis is performed. Before the final trajectory is stated, a short optimization process was performed to assure best performance.

5-5-1 Entrance corridor

Similarly to the aerocapture maneuver three different limiting trajectories were identified. The limiting factor for EDL were identified to be the g-load limit and skipping out of the atmosphere. The following list details the trajectories, which are graphed in Figure 5-10.

EDL1 The first reference trajectory is designed to have full lift up until target altitude is reached. The trajectory enters with the steepest entrance angle $\gamma_{en} = -12.77$ such that g-loads of 5-g are reached, in accordance with the requirements. Due to the high velocities the spacecraft is able to generate enough lift to gain altitude (skipping), before it descends and lands on the Mars surface. The Mach number at target altitude was found to be close to the desired conditions of $M = 1.8$.

EDL2 In this approach the spacecraft generates full lift down during its descent to Mars. This allows for the most shallow entrance flight path angle, such that skipping out of the Martian Atmosphere is found to be the limiting factor. The spacecraft begins to skip but does not have enough energy to escape the atmosphere. From this point it descends and reaches the target altitude at a relatively high Mach number compared to EDL1 and EDL3.

EDL3 This trajectory follows EDL1 until maximum g-loads are reached, at which point the spacecraft maneuvers to a less lift generating attitude. Because the C_{D_α} is negative, a smaller angle of attack results in a higher drag coefficient and a small spike in the g-loads. To avoid exceeding g-load the spacecraft enters with shallower angle $\gamma_{en} = -12.50$ to assure that the g-load spike is within the 5-g limit. This mission then follows a non skipping trajectory, and descends to a lower Mach number than EDL1 and EDL2.

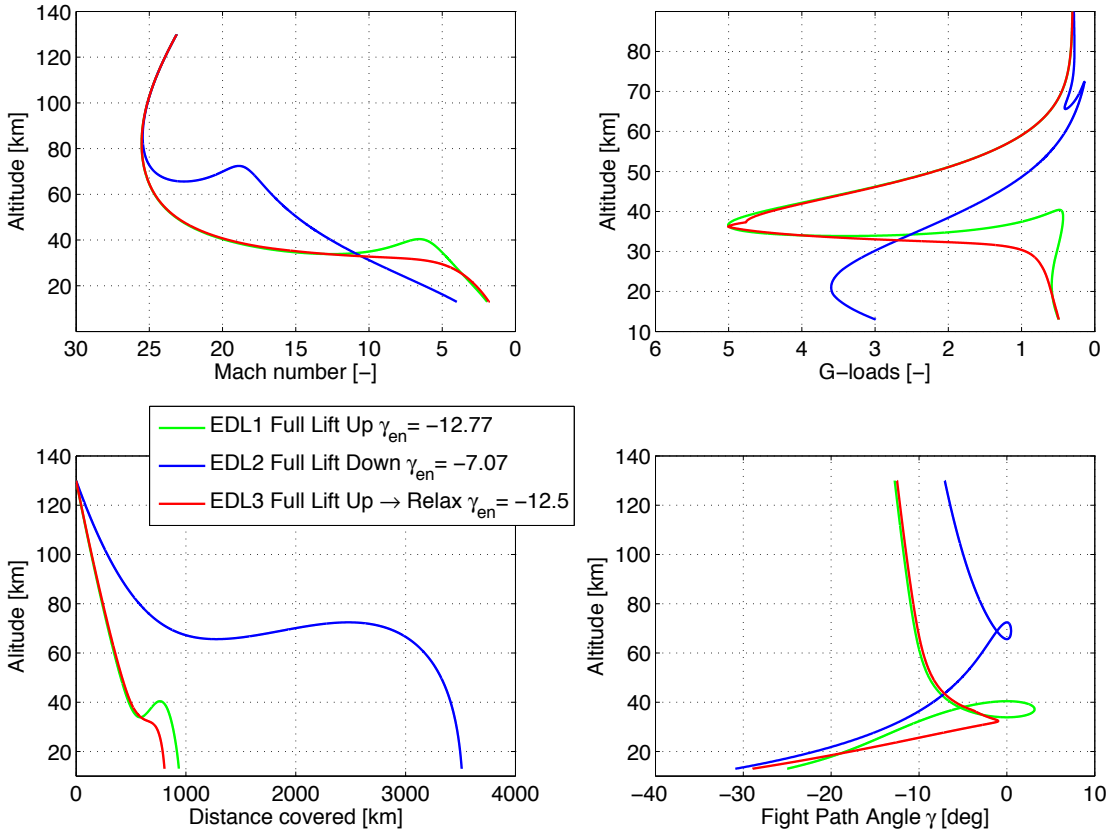

Figure 5-10: Entrance corridor for the Entry, Descent and Landing

5-5-2 Sensitivity Analysis

The sensitivity analysis is performed for the three parameters mentioned in aerocapture sensitivity analysis: mass, surface area and entrance conditions. The sensitivity analysis is performed for the non optimized reference mission and the influence on the target Mach number is displayed in Figure 5-11.

- **Change in Surface Area -** An increase in the surface area results in a lower final Mach number, yet comes at the cost of an increase in mass. Additionally, it causes higher drag forces on the system, resulting in a faster deceleration process such that the entry conditions have to be altered to assure the 5-g limit. However, a larger surface allows for more control on the flight path angle since the gain in lift generated is at dispense to modify the flight path angle.
- **Change in Mass -** Increasing the the mass is closely related to decreasing the surface area considering the definition of ballistic coefficient. With no change in the area, the same aeroshell

cannot dissipate the increased potential and kinetic energy, resulting in higher velocities at the target altitude. Furthermore, because of the increased ballistic coefficient it results in lower deceleration loads.

- **Variations in EDL Entrance Speed -** Variations in the entrance conditions are already briefly discussed in the risk analysis. In case the spacecraft enters with a more shallow flight path angle, it experiences lower g-loads. However, it is more prone to start to skip, which was considered unfavorable in the optimization analysis. Oppositely, a steeper entrance results in higher g-loads and lower Mach number at the target-box. A higher entrance velocity for the same entrance angle will experience an increase in g-loads along with skipping inside of the atmosphere.

5-5-3 Risk Analysis

Each of the given trajectories describes the physical limits of the system such that a small inaccuracy can easily lead to exceeding these limits. For each trajectory the main risks are listed. A risk mitigation proposal follows.

EDL1 Reference mission EDL1 is designed to enter with the steepest possible angle. In case the spacecraft enters with a steeper angle, or is not able to generate the desired lift, the 5.2-g limit will be exceeded. A second risk is the skipping maneuver. Analysis in subsection 5-5-4 (Optimization of Final Trajectory) shows that the benefit of skipping in terms of final Mach number was very small compared to the increase in heat load due to the prolonged time of EDL.

EDL2 The second trajectory bares the risk of either entering too shallow, or not being able to generate enough negative lift such that the spacecraft skips out of the atmosphere, having catastrophic consequences. Similarly to EDL1 this trajectory results in one skip, increasing the time in the atmosphere and thus the loads on the insulation of the spacecraft.

EDL3 The third option shares the risk of exceeding the g-load limit with EDL1. However, since this mission avoids the skipping maneuver, it takes the least time to reach target altitude, keeping the heat load low. The overall heat flux is comparably high to EDL1; there is a risk that if the TPS suffers considerable damage during aerocapture maneuver, it could potentially result in mission failure.

Risk Mitigation There were four strategies identified to reduce the likelihood of the above described scenarios. The first strategies is to apply a safety margin of 1-g to the maximum g-load expected, thus 4-g was identified as the new maximum limit for the trajectory. This directly results in a more shallow entrance flight path angle, for which a safety margin of ± 0.5 deg was set. The second strategies follows the idea of the aerocapture strategy by flying with $\alpha_{nominal} = 0.75\ \alpha_{max}$. As the benefit of skipping is considered low, the team chose a strategy that avoids skipping inside of the atmosphere, such that $\gamma < 0$. Finally, to decrease the TPS loading it was decided to enter with a high angle of attack, accounting for possible small damages to the TPS from aerocapture.

5-5-4 Optimization of Final Trajectory

Before the final trajectory is chosen a short optimization was performed to assure that target conditions were met efficiently. It was found that if staying within the g-limits, the Mach number at target height became the key driver, requiring optimization to assure requirement fulfillment.

No Skipping Skipping inside the atmosphere comes at a considerable advantages by reducing the g-loads on the system, as can be seen in the g-load comparison (blue line in Figure 5-10). However detailed trajectory analysis revealed that skipping does not result in a lower Mach number at target altitude, because aeroshell drag is a function of the velocity squared. At a higher altitude, the spacecraft has a considerably lower velocity, yet a higher energy level; on its descent its velocity is too low to generate enough drag and slow down to target velocity. The optimization scheme avoids

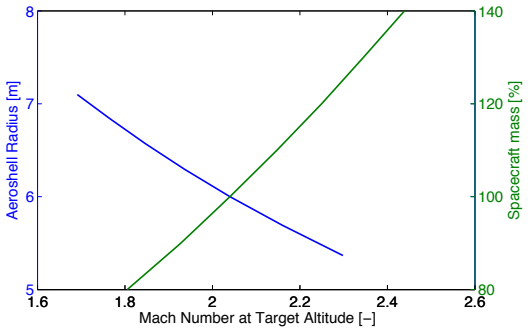

Figure 5-11: Change of Mach number at target with change of area and mass

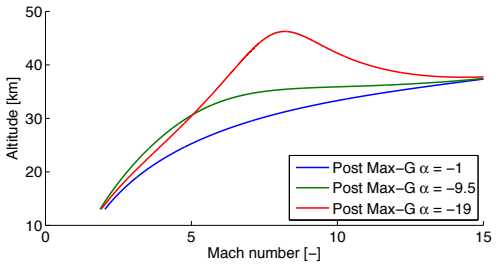

Figure 5-12: Change of Mach number with altitude for a range of angle of attacks

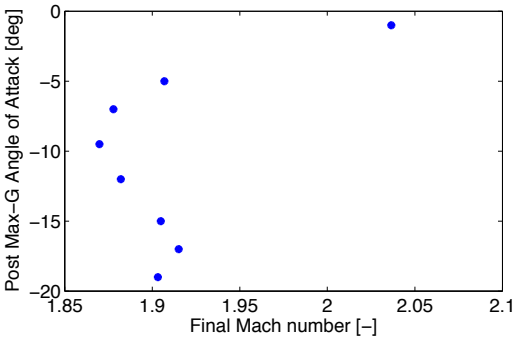

Figure 5-13: Change of target Mach number with post maximum g angle of attack

skipping. It was found that when using trajectory **EDL3** a reduction of lift after the maximum g-loads to a half of the maximum nominal value $\alpha_{update} = 0.5\alpha_{max\ nominal}$ would result in the lowest Mach number out of the all the combinations as visualized in Figure 5-12 and 5-13.

Increase of Lift Once the spacecraft reaches a certain energy level, it is physically impossible to skip. This point is determined by means of applying full lift up throughout several points in the trajectory, and the most efficient turned out to be return to nominal maximum lift after 241 seconds after entry.

Change of Aeroshell Radius It was found that the current radius of the aeroshell does not deliver the required target Mach number of 1.8. Reaching the target box with the required conditions is found more important than remaining with the maximum radius of the aeroshell. During the status update on the 18th of June 2013 the decision to redefine the maximum aeroshell diameter from 6 to 6.5 meter was agreed with the customer. The effects of this on the aerocapture maneuver can be observed in the sensitivity analysis of the aerocapture maneuver in subsection 5-4-2. At the same time the safety margin for the g-loads was relaxed from 1 to 0.9, resulting in a max g-load of 4.1.

5-5-5 Final Trajectory

The final trajectory resembles EDL3, but combines the safety margins explained in the risk analysis together with the optimization strategies identified beforehand. The increase of the aeroshell radius from 6 to 6.5 meters results in the final specifications listed in Table 5-2 and are visualized in Figure 5-14.

Table 5-2: Reference EDL trajectory specifications

Design Parameter	Variable	Magnitude	Unit
Entrance Velocity	V_{en}	4715.3	m/s
Target Mach number	V_{ex}	1.80	m/s
Entrance Angle	γ_{en}	-11.55	deg
Skip out margin		$\pm$ 0.5	-
Angle of attack	α	$19 \rightarrow 9.5 \rightarrow 19$	deg
Angle at Target	γ_{ex}	-25.5	deg
Maximum G-Load	g_{max}	4.11	-
Time	t	400.3	s
Groundtrack distance	R	943.718	km
Maximum heat flux	$\dot{q}$	27.94	W/cm^2
Total heat load	q	2401.8	J/cm^2
Aeroshell radius	R_{as}	6.5	m
Skipping trajecory		no	

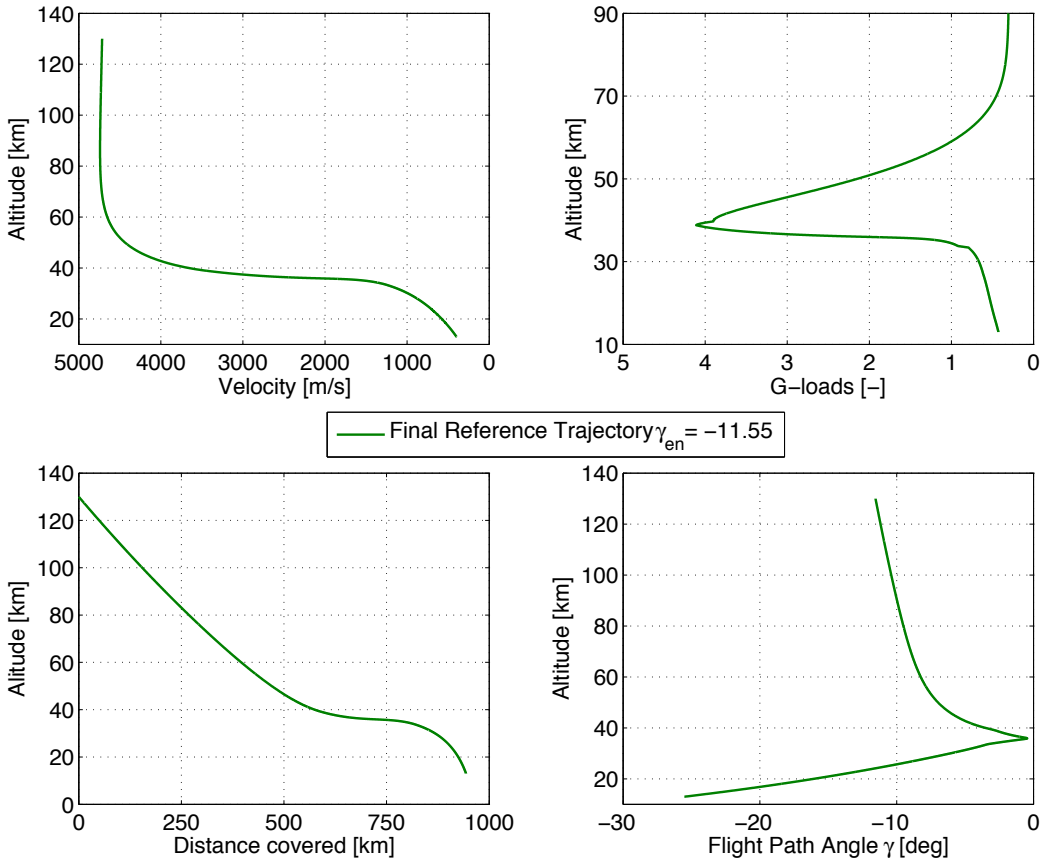

Figure 5-14: Reference EDL trajectory

Chapter 6

Thermal Protection System Design

During aerocapture and EDL, high temperatures are generated by the viscous boundary layer behind the shock wave of the hypersonic flow. The thermal protection system is designed to act a passive system consisting of different heat resisting layers and this chapter entails the approach to design this TPS. A model is used to size the heat flux expected, and is described in the first section together with the assumptions. The model is then verified and validated by scaling and comparing it to the results of the NASA Phase 1 study [10]. Hereafter, the heat transfer and the wall temperature at the stagnation point are defined, and with this knowledge, the distribution of heat transfer on the rest of the shield is obtained; this information allows for a material selection and thickness layer determination of the TPS.

6-1 Model

The model is valid for the blunt nose of an aeroshell on which the stagnation point is located. Figure 6-1 shows the heat transfer breakdown due to incoming convective heat. The convective heat decays into three forms: radiation back to the atmosphere ($\dot{q}_{rad}$), conductive heat through the shell ($\dot{q}_{cond}$) and heat stored in the wall of the shell ($\dot{q}_{stored}$)[23]. The method explained in the following section is used to determine the heat transfer and wall temperature at the stagnation point.

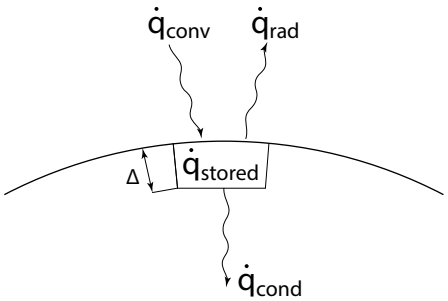

Figure 6-1: Heat transport on a small element

6-1-1 Assumptions

The assumptions used in the model are:

PA1 The stagnation point is the point with the maximum heat transfer and remains on the curved segment of the aeroshell
PA2 The velocity of the airflow behind the shock wave is subsonic. The reason for this assumption is the high half cone angle of the cone (approaching a flat plate)
PA3 The atmosphere of Mars consists of CO_2 only
PA4 The heat transfer to the vehicle is solely due to convective heat transfer. Incoming heating due to radiation is associated with the free electron movement caused by the the ionization, and the effects are not significant at this velocity. For reentry to Earth, radiative heat becomes important for velocities in excess of 9.14 km/s because of ionization of Oxygen and Nitrogen [23]. The ionization of CO_2 occurs at higher temperatures and higher reentry velocities
PA5 The gas across the shock wave is both thermally and calorically perfect
PA6 The flow decelerates isentropically downstream of the normal portion of the shock wave to the stagnation point. This is happing outside of the thermal boundary layer
PA7 The density, pressure and dynamic viscosity behind the normal portion of the shock wave (at stagnation) point are comparable to the density, pressure and dynamic viscosity just outside the viscous boundary layer
PA8 The heat transfer to stagnation point is one dimensional. Changes in directions tangent to the surface of the TPS are relatively small
PA9 The heat transfer at the outer edge of the shell increases, but remains below the heat transfer of the stagnation point

6-1-2 Method

For the element shown in Figure 6-1, the energy decay [23] is given by Equation 6-1 as a function T_{aw}, the adiabatic temperature.

$$\dot{q}_{conv} = \dot{q}_{stored} + \dot{q}_{cond} + \dot{q}_{rad} = h(T_{aw} - T_w) \tag{6-1}$$

Where h is the convective-heat transfer coefficient, analytically obtained with Equation 6-2, gathered from [23] and [24]:

$$h = \frac{0.763}{Pr^{0.6}}(\rho_{t2}\mu_{t2})^{0.5} c_p \left[1 + (Le^{0.52} - 1)\frac{h_d}{H_{t2}}\right]\sqrt{\frac{du_e}{dx}} \tag{6-2}$$

Pr is the Prandtl number, given by $Pr = \mu c_p/\lambda$ (around 0.78 for the Mars atmosphere). The Lewis-Semenov number (Le) approaches 1 for turbulent conditions. The dynamic viscosity (μ) and thermal conductivity are (λ) both dependent on surrounding temperature and the gas [25] and given by:

$$\mu = 26.69 \times 10^{-7}\frac{(MT)^{0.5}}{\Omega_v \sigma_c^2} \tag{6-3}$$

$$\lambda = 2.63 \times 10^{-23}\frac{(T/M')^{0.5}}{\Omega_v \sigma_c^2} \tag{6-4}$$

The stagnation point velocity evaluated by Euler's equation [23] is:

$$\sqrt{\frac{du_e}{dx}} = \frac{1}{R_N}\sqrt{\frac{2(P_{t2} - P_0)}{\rho_{t2}}} \tag{6-5}$$

Therefore, the expression for stagnation point heat-transfer by Fay and Riddell becomes:

$$\dot{q}_{conv} = \frac{0.763}{Pr^{0.6}} \sqrt{\frac{\rho_{t2}\mu_{t2}}{R_N}} \left(\frac{2(P_{t2} - P_0)}{\rho_{t2}} \right)^{0.25} c_p(T_{aw} - T_w) \tag{6-6}$$

The adiabatic temperature T_{aw} in the above equation is derived from the relation:

$$T_{aw} = T_{t2} + \sqrt{Pr}(T_0 - T_{t2}) \tag{6-7}$$

The rate at which the heat energy is stored [23] can be found using Equation 6-8. The conductive heat rate through the back wall of the element is given by the Fourier Heat conduction law [26], Equation 6-9 and the rate at which heat is radiated into the atmosphere from the TPS wall is given by equation Equation 6-10.

$$\dot{q}_{stored} = \rho_w c_w \Delta \frac{dT_w}{dt} \tag{6-8}$$

$$\dot{q}_{cond} = -k_w \frac{dT}{dy} \tag{6-9}$$

$$\dot{q}_{rad} = \epsilon \sigma T_w^4 \tag{6-10}$$

Solving Equations 6-6, 6-8, 6-9 and 6-10 simultaneously, a differential equation for the wall temperature of the TPS can be obtained. The differential equation can be solved based on airflow properties in the free stream and across the shock wave, obtained from the reference trajectories in Chapter 5. The equation is solved numerically using Euler's method and the result are hereafter further processed to obtain the heat transfer at the stagnation point. However, the heat that the vehicle is exposed to at the stagnation is not equal to the amount of convective heat transferred to it. The ratio between heat absorbed by the system and heat dissipated by the airflow is given by the Stanton number [24]. The Stanton number is defined by Equation 6-11 and can be used in the validation of the model.

$$CH = \frac{\dot{q}_{conv}}{\rho_{t2} u_{t2} c_p \left(T_{aw} - T_w\right)} \tag{6-11}$$

6-2 Verification

The Sutton-Graves convective heating relation [20] is a simplified equation for heat flux that can be used to verify the model. This relation, Equation 6-12, makes use of the nose radius as the only geometric parameter to define the heat at the stagnation point [24]. It is accurate for blunt bodies within 5-10% [21].

$$\dot{q}_{conv} = C \sqrt{\frac{\rho_0}{R_N}} V^{3.15} \qquad with \;\; C = 1.9027 \times 10^{-4} \tag{6-12}$$

The above constant C, 1.9027×10^{-4}, is applicable to the Mars atmosphere only [21]. The trajectory and aeroshell properties are based on NASA Phase 1 Report: 23 meter HIAD with a nose radius of 7.5. The comparison of the results is presented in Figure 6-2. The error between the model, presented in this chapter and the simplified Sutton-Graves are small, and the model is thus considered verified.

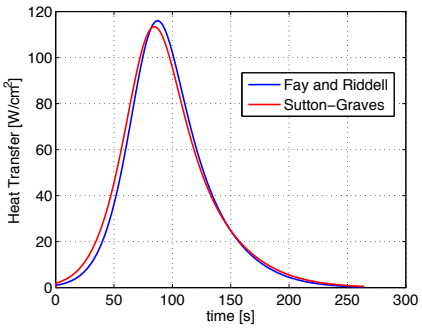

Figure 6-2: Sutton-Graves and Fay Riddell Heat Transfer

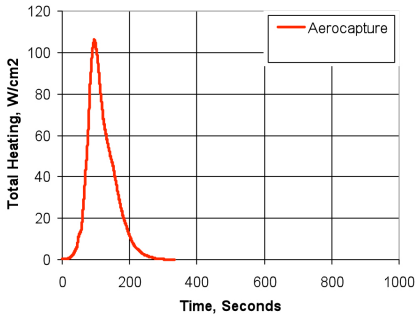

Figure 6-3: Heat Transfer of HIAD concept according to [10]

6-3 Validation

The heat transfer used in this report, given by Equation 6-6, is also dependent on the TPS material. The materials selection is based on the materials used on the HIAD concept [10]: 0.25 inch Silicia Felt for the windside and 0.01 inch RTV-560 for the leeside. The material thickness and properties are not accurately specified in the Phase 1 report and the design aimed to reproduce similar compounds. This has a minor yet noticeable effect on the heat transfer.

Further validation is performed by comparing the Stanton number on the stagnation point to the results obtained from study [27] on blunt cones performed in a hypersonic test. The value for the Stanton number is independent of the geometry of the concept and its maximum value is around 0.017 at the stagnation point. The average value of the Stanton number is 0.0245 at the stagnation point; the logarithmic graph for the Stanton number for the DSE03 model is shown in Figure 6-4:

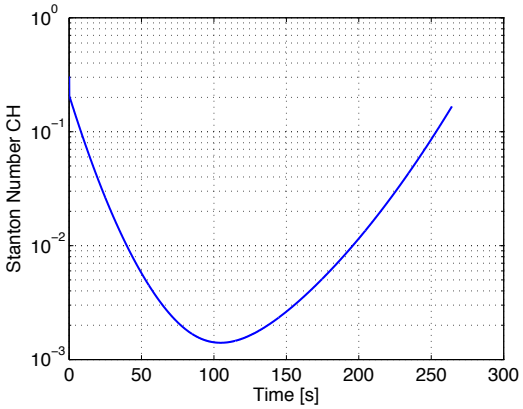

Figure 6-4: Logarithmic plot of the Stanton number

The higher value obtained can be related to the Knudsen number, which defines the border of the discrete particle flow and the continuum airflow [24]. Using the result for the Sutton-Graves relation, this value would be slightly lower. However, the density and the airspeed at the thermal boundary layer given in the denominator of Equation 6-11 are also expected to be higher than the one assumed in the model. Overall, it is concluded that, even though the results obtained are slightly higher, the TPS model is valid for the preliminary sizing of the TPS.

6-4 Heat Transfer at Stagnation Point

The heat transfer at the stagnation point is defined for aerocapture and EDL as taken from Section 5-4. Part of the decision for these trajectories is based on the TPS limitations. To design the TPS, the total heat flux defines the materials that can be used as it is directly related to the wall temperature, which has to stay below the allowable value for the material of the outer layer. The thickness required for the materials to protect the payload from the heat is instead defined by the heat load. The heat transfer for aerocapture is illustrated in Figure 6-5. The initial speed of the vehicle during the aerocapture is 7 km/s; this is in the hypersonic regime, for which the ratio of specific heats γ_{sh} across the shockwave cannot be considered constant; this is directly taken into account in the trajectory model (based on relationships presented in Chapter 4). Overall, the peak heat flux is $68 W/cm^2$ during aerocapture; this is close to the current maximum market specifications, even though new materials have been successfully tested which are capable of withstanding higher heat transfer range [28].

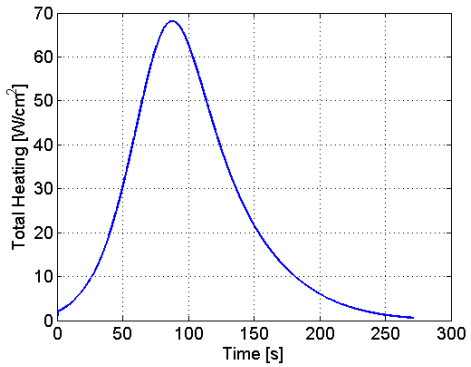

Figure 6-5: Heat Transfer at stagnation point during aerocapture

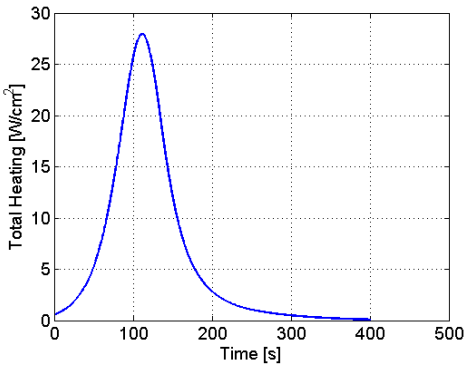

Figure 6-6: Heat Transfer at stagnation point during EDL

For the EDL phase, the heat transfer at the stagnation point is given in Figure 6-6. The magnitude of the initial velocity is $4.715 km/s$. This velocity eventually decreases within the supersonic regime. The drop in heat transfer after the peak is due to the large decrease in velocity as the spacecraft enters denser layers of the atmosphere.

6-5 Heat Transfer Distribution over the Aeroshell

One of the requirements for the design of the TPS is that the stagnation point should remain on the spherical blunt nose. If the stagnation point is located on the straight segment flat plate undesireable conditions [24] occur; this defines the maximum angle of attack for the TPS. The distribution of heat transfer on the aeroshell is determined separately for the spherical nose and the straight segment of the aeroshell. This approach is performed for a zero angle of attack, where the distribution would be symmetric across the aeroshell and implies that the stagnation point is located on the tip of the nose. After this point the heat transfer drops considerably with distance. A schematic of the aeroshell with all the useful geometric descriptions and coordinates is shown in Figure 6-7.

For the round segment the local value of the heat is only dependent on the angle θ [24]. This variation is given in Equation 6-13, in which $q(0)$ stands for the heat transfer at the stagnation point.

$$q(\theta) = q(0) cos^{3/2}\theta \tag{6-13}$$

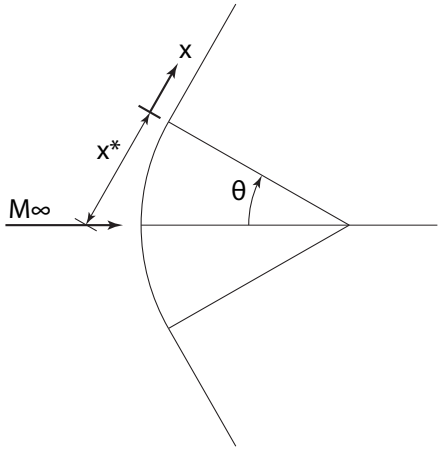

Figure 6-7: Aeroshell's geometric coordinates

The heat transfer for the flat segment is approximated using the reference temperature method [24]. The Mach number used is approximated by $M_e = 0.4$ at the thermal boundary layer. The airflow particles behind the shock vary in velocity from rest at the stagnation point to below Mach 1 directly after the shock. Therefore the approximation $M_e = 0.4$ at the boundary of the thin boundary layer, is considered valid. This is done to better approximate reference values for the calculations that follow. The reference temperature at distance x^* is given by Equation 6-14 [24].

$$\frac{T^*}{T_{t2}} = 1 + 0.032M_e^2 + 0.58\left(\frac{T_w}{T_{t2}} - 1\right) \tag{6-14}$$

Density (ρ), dynamic viscosity (μ), thermal conductivity (λ) and the Prandtl reference number (Pr) are all update according to the new temperature. The values at position x^* are denoted by the same superscript. The Reynolds number (Re_x) at x is given by:

$$Re_x^* = \frac{\rho^* u_{t2} x}{\mu^*} \tag{6-15}$$

Stanton number also updates to CH^* with Equation 6-17 and is compared to the Stanton number along a flat plate in incompressible flow, Equation 6-16.

$$CH^* = \frac{0.332}{\sqrt{Re_x^*}}(Pr^*)^{2/3} \tag{6-16}$$

$$CH^* = \frac{\dot{q}_{conv}}{\rho^* u_{t2} c_p \left(T_{aw} - T_w\right)} \tag{6-17}$$

Solving Equations 6-16 and 6-17 simultaneously results in an expression for the convective heat flux, Equation 6-18, as a function of x. This expression is valid for the flat part of the aeroshell, when $x > x^*$. Note that the heat capacity for constant pressure is assumed to be constant. The heat transfer at five different locations on the aeroshell during aerocapture is shown in Figure 6-8.

$$\dot{q}_{conv}(x) = \frac{f(Pr^*, P_{t2}, T_{t2}, u_{t2}, T_{aw}, T_w, M_e)}{\sqrt{x^* + x}} \tag{6-18}$$

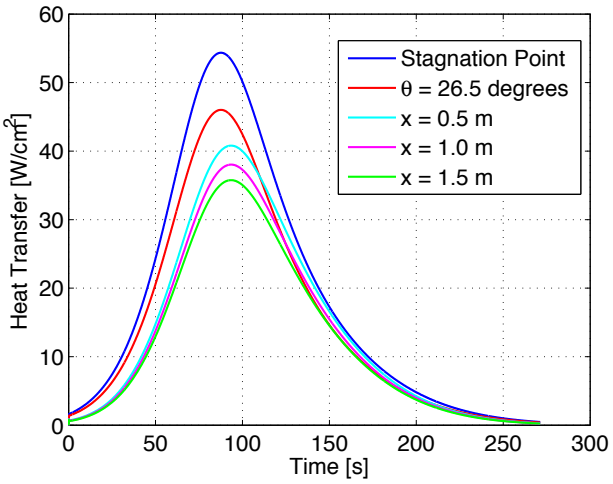

Figure 6-8: Heat transfer on five different locations on the aeroshell for the aerocapture phase

6-6 Material Selection

The materials used must ensure that the TPS is able to:

- Resist the temperature
- Fold and package without damage
- Ensure air-tightness
- Provide resistance to chemical reactions on the surface material
- Be durable for the duration of aerocapture and EDL

To minimize the mass, thickness is one factor that can be minimized. The materials researched are shown in Table 6-1. The material selected and considered in this chapter are obtained based on research results from references [29], [30], and [31].

Table 6-1: TPS material characteristics

Material	**Layer**	**Density** $[kg \cdot m^{-3}]$	**Conductivity** $W/m/K$	**Specific Heat** $J/kg/K$	**Emissivity** [-]
Nextel AF14 (312)	Outer	858	0.15	1050	0.44
Refrasil C1554-48	Outer	924	0.865	1172	0.7
Hexcel 282 Carbon	Outer	891	0.5	1000	0.9
Silicia Felt(SiC)	Outer	240	0.024	750	0.85
Pyrogel 6650 (5223)	Insulator	110	0.03	1046	
Pyrogel 5401	Insulator	170	0.0248	1046	
Refrasil 1800	Insulator	156	0.085	1172	
KFA5	Insulator	98	0.25	1250	
Saffil	Insulator	144	0.06	1000	
Polyimide	Insulator	1430	0.52	1150	
Kapton	Boundary	1468	0.12	1022	
Upilex	Boundary	1470	0.29	1130	
kelvar	Boundary	1140	0.04	1400	
RTV 560-32	Boundary	480	0.043	1420	

One material per layer is chosen from Table 6-1. Emphasis is placed on the temperature resistance, high heat capacity of the material, low thermal conductivity of insulator and boundary layer, and emissivity to ensure high radiation heat transfer back to the atmosphere. Materials with a lower

density are favored as they will result in a lower TPS mass. The material choices are documented below:

- **Outer -** The material selected for the outer layer is Silicia Felt (SiC). The main reason is that the material has low density, low thermal conductivity, and maximum continuous temperature resistance of 1800 Celsius. Although heat capacity is lower, the high emissivity reduces the effect of heat transfer to the material. The properties of this material are not public, and are thus iterated from other silicon compounds.
- **Insulator -** The insulator provides resistance against the head loads. Pyrogel 5401 features the lowest thermal conductivity, and should perform the best. However, considering the density of the material, Pyrogel 6650 is preferred.
- **Boundary -** This layer provides permeability for conducted gases; material RTV 560-32 is selected for its low thermal conductivity and low density.

6-7 Thickness Determination and Finalized Design

The thickness is sized on the aerocapture loads as they are highest. The wall temperature at stagnation during aerocapture is shown in Figure 6-10. The initial temperature is taken at 130 km altitude. This temperature depends on the albedo and infrared radiation from Mars, the heat from sun, the material's emissivity, absorption, and the internal heat dissipation[32]. The value was estimated at -173.15 Celsius (100 K) [33]. Note that the maximum temperature occurs slightly after the maximum heat transfer. At the end of aerocapture, the final temperature at the wall is around $27°C$.

6-7-1 Method

The design choice led to a three layer TPS, where each layer had different functions. The first layer has to cope the with the heat transfer and the radiation back to the atomosphere. The second segment acts as an insulator and withstands the heat load, hence a low conducting material. The inner most layer, is a permeable material which acts as a gas barrier protecting the mechanism behind. The thickness of each layer is determined by the heat transfer across the three layers, satisfying the the law of conservation of energy.

$$k\frac{T_w - Ti}{L_1} = \rho_w C\Delta\frac{dT}{dt} \tag{6-19}$$

For multiple layers, shown in Figure 6-9, the preceding equation becomes:

$$k^*\frac{T_w - Ti}{L_1 + L_2 + L_3} = \rho C\Delta\frac{dT}{dt} \tag{6-20}$$

Where k^* is:

$$\frac{1}{k^*} = \frac{1}{k_1} + \frac{1}{k_2} + \frac{1}{k_3} \tag{6-21}$$

The thicknesses obtained are presented in Table 6-2. Using these thicknesses, the peak temperature is reduced to $200°C$ behind the TPS.

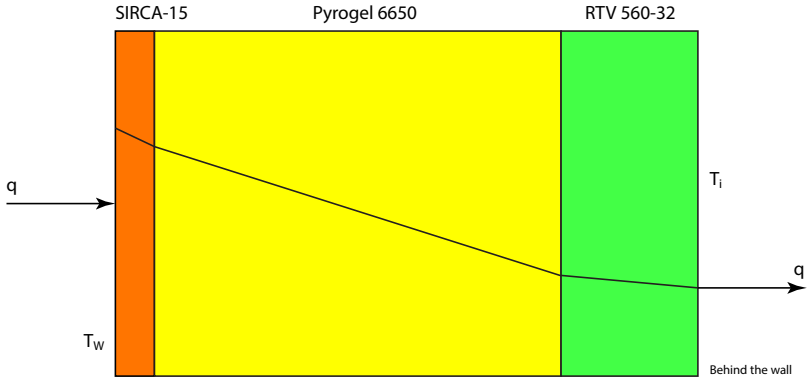

Figure 6-9: Heat shield material layers

Table 6-2: Layer Thicknesses at the Cone Section

Material	**Layer**	**Thickness** $[mm]$	**Max. Allowable Temp.** $[C]$
SiC	Outer	5	1800
Pyrogel 6650 (5223)	Insulator	52	650
RTV 560-32	Boundary	17.5	260

6-7-2 Mass Estimation

The location of the stagnation point is limited to the round segment of the aeroshell; the calculated thicknesses thus remains constant in that section. After the cone section the thickness of Pyrogel 6650 and RTV 650-32 layers decrease linearly to $20mm$ and $10mm$, respectively, due to the decrease in heat flux. However, as the aerodynamic model from Chapter 4 has problems in determining flow conditions around the edges, a conservative approach is taken whereby the outer $0.5m$ of the shell feature the same thickness as the round section. The final values for the mass of each layer at each segment of the TPS is given in Table 6-3

The total mass for the nose segment, middle part and edge segment are respectively $79.6kg$, $1157.8kg$ and $268.2kg$. This results into a total mass of 1505.6 kg for the whole heat protection blanket of the TPS. This means that the TPS alone prevents the system for fulfilling the requirement whereby the HIAD and control system weigh less than $1000kg$. The mass of the TPS is also higher than examples from literature when up scaled to a similar size, as seen in Chapter 9. The reasons for the large mass are:

- For the rigid section, non-flexible materials could be used to save weight. For simplicity, the material is kept constant
- Due to the uncertainties in the flow at the edges of the aeroshell, the thickness is increased in outer layer of the aeroshell to the same thickness as the stagnation point. This conservative design choice increases mass. A more detailed analysis of the flow around the tips can help to decrease the thickness.

Table 6-3: Weight of each layer at each segment

Material	Nose segment $[kg]$	Middle segment $[kg]$	Edge segment $[kg]$
SiC	6.232	118.144	21.004
Pyrogel 6650 (5223)	29.704	389.875	100.118
RTV 560-32	43.621	649.792	147.026

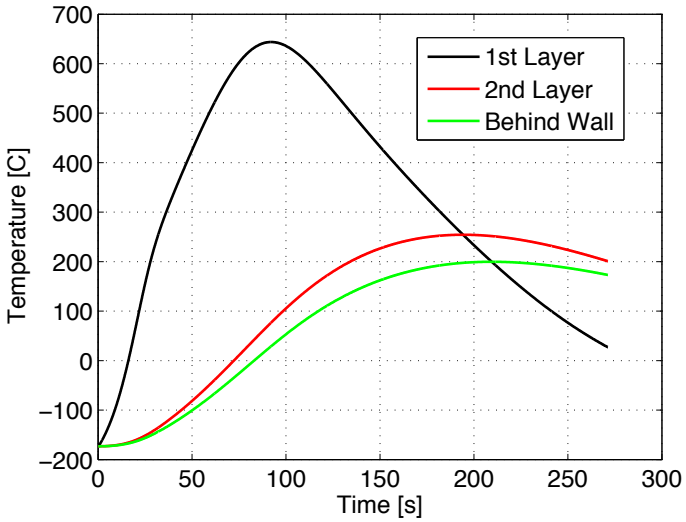

Figure 6-10: Temperature in each different TPS layer

6-8 Limitations and Risks

The limitations and potential risks involved with the current TPS design are outlined below:

- No analysis is done on the adhesive bonding of the layers. The temperature inside each material should not result into delimitation of the TPS protective blanket.
- The model assumes that the atmosphere consists only of CO_2, but the presence of particles of dust in the atmosphere could damage the TPS blanket. The heat transfer is assumed to be one dimensional; the heat travels straight from one layer to the next. This assumption indicates that the designed thickness is actually higher than necessary.
- After aerocapture, the heat conducted will cause the temperature to increase. A method for dealing with the heat should be included to allow the TPS to be reusable after such to environment should be considered. This also holds for exiting the atmosphere. The time outside the atmosphere should be enough such that the initial temperature for reentering is comparable to pre-aerocapture conditions.

Chapter 7

Structural Design

The goal of the chapter is to provide the vehicle's structural characteristics, with a particular focus on the c.g. offset mechanism. To achieve this goal, first the relevant geometric dimensions are determined. Then the section is present discussing seven design options for the actuator mechanism, together with a RAMS analysis. With this knowledge, an actuator mechanism is chosen and the load analysis started. Thereafter, the chosen control mechanism is sized.

7-1 Vehicle Sizing

The following section presents the method that was used to determine the dimensions of the vehicle that were necessary for the advancement and implementation of various analyses.
The overall process is as follows:

1. Isolate relevant requirements and transform them into constraints
2. Gather reference data for existing inflatable aeroshell concepts
3. Calculate characteristic ratios
4. Apply said ratios to determine vehicle dimensions

7-1-1 Requirements

The requirements (as seen in Appendix B) that were found to be relevant for the geometric layout of the vehicle are:

- The stability ratio (aft distance of center of mass divided by diameter) [34] must not exceed 0.3 per req. 20
- The mass of the vehicle at entry must not exceed 10,000kg per req. 30
- The diameter of the launcher fairing must not exceed 5m per req. 31
- The mass of the control system must not exceed 10% of the vehicle's entry mass per req. 32
- The diameter of the aeroshell must not exceed 13m per req. 33
- The vehicle must fit within the maximum static payload length of 16.484m for the Delta IV launch vehicle per req. 34
- The elements of the vehicle that are not protected by the TPS may not be exposed to the flow per req. 35

7-1-2 Reference Data

The reference data was gathered for two existing inflatable aeroshell configurations: IRVE-3 and the MIAS as given in Table 7-1. Some of the measurements (denoted with a *) were obtained by means of visual inspection of the schematics provided in the respective sources.

Table 7-1: Reference data for the IRVE-3 and the MIAS

	IRVE3 [3]	MIAS [35]
Direct from sources:		
Aeroshell diameter $[m]$	3	23
Launcher adapter diameter $[m]$	0.4699	3.6
Single toroid diameter $[m]$	0.245*, 0.088*	0.92
Aeroshell half-nose angle [deg]	60	60
Inflation volume $[m^3]$	1.43 [36]	
Inflation system height $[m]$	0.554*	-
Derived:		
Inflation volume $[m^3]$		620
Inflation tank volume $[m^3]$	0.0185	-
Stacked toroid height $[m]$	0.282	1.98
Filled volume $[m^3]$	1.37	582

In Table 7-1, "Stacked toroid height" is the thickness of the hollow conical frustum that the toroids occupy in the vertical direction. "Filled volume," in turn, is the volume of said hollow conical frustum.

7-1-3 Characteristic Ratios

The reference data was used to calculate three ratios that were taken to be constant for inflatable aeroshells and were then used to scale the dimensions of an aeroshell given a number of initial constraints. The ratios are presented in Table 7-2.

7-1-4 Assumptions & Vehicle Dimensions

The scaling ratios determined in the previous section were applied to existing vehicle constraints to arrive at the figures given in Table 7-3.

Then, assuming that:

PA1 The rigid section of the aeroshell is $5m$ in diameter to maximize the nose radius and minimize the weight by using conventional TPS,

PA2 The inflated section of the aeroshell begins at the outer edge of the rigid section of the aeroshell,

Table 7-2: Characteristic ratios derived from reference data for the IRVE-3 and the MIAS

	IRVE-3	**MIAS**	**Average**
$\frac{\text{Stacked toroid thickness } [m]}{\text{Aeroshell diameter } [m]}$	9.42%	8.62%	9.02%
$\frac{\text{Filled volume } [m^3]}{\text{Inflation volume } [m^3]}$	95.6%	93.9%	94.8%
$\frac{\text{Inflation tank volume } [m^3]}{\text{Inflation volume } [m^3]}$	1.30%	-	1.30%

Table 7-3: Characteristic ratios derived from reference data for the IRVE-3 and the MIAS

	Characteristic ratio	**DSE03 value**
Stacked toroid height $[m]$	9.42%	1.08
Inflation volume $[m^3]$	95.6%	89.6
Inflation tank volume $[m^3]$	1.30%	1.16

PA3 The center of gravity of the aeroshell (including the inflation system and the mechanical connection between the aft body and the aeroshell) lies at $\frac{3}{4}$ of the total height of the aeroshell (a conservative estimate, given the fact that the rigid section of the aeroshell and the inflation tank are positioned far forward),

PA4 The aft body is packed uniformly (density of aft body is constant throughout and the center of gravity of the aft body therefore coincides with its geometric center)

The resulting dimensions of the vehicle are given in Table 7-4.

Table 7-4: Final vehicle dimensions

Nose radius $[m]$	5.41	$X_{c.g.}$ Aeroshell $[m]$	1.83
Aeroshell height $[m]$	2.43	$X_{c.g.}$ Aft Body $[m]$	4.11
Volume of sphere cap $[m^3]$	6.13	Average aft body length $[m]$	4.60
Total distance from nose to interface $[m]$	1.30	Maximum aft body length $[m]$	7.11
$X_{c.g.}$ Vehicle $[m]$	3.90	Maximum aft body cap diameter $[m]$	3.55

Another constraint imposed by geometry that impacts all further analyses is the maximum angle of attack. Since the stagnation point should not be allowed to travel past the spherical cap (from subsection 6-1-1) the maximum angle of attack is the complement of the half-nose angle. The larger the nose angle the smaller the maximum possible angle of attack. With the chosen half-nose angle of $62.5deg$ the maximum angle of attack is $27.5deg$.

7-1-5 Sensitivity Analysis

The main outputs of the method are the maximum aft body length, $X_{c.g.}$ aft body, and maximum aft body cap diameter. The response of those outputs to the main inputs are shown in Table 7-5.

The maximum aft body length is very sensitive to changes in half-nose angle and aeroshell diameter. Increasing the half-nose angle or the aeroshell diameter leaves significantly more room for the aft body as per requirement 35 in B. Increasing the launcher fairing diameter reduces the aft body's maximum length since the diameter of the aft body bus is taken to be the diameter of the launcher fairing and, ceteris paribus, increasing the width of the aft body bus causes it to be exposed to the flow sooner at maximum angles of attack. Increasing the magnitude of the required c.g. offsets decreases the maximum aft body length since, at maximum displacement the aft body of the vehicle would be exposed to the flow sooner.

The location of the center of gravity of the aft body is particularly sensitive to changes in aeroshell diameter. This is because its location is determined using the location of the center of gravity of the entire vehicle, which, in turn is placed at 0.3 aeroshell diameters away from the nose of the aeroshell as per requirement 20 in Appendix B.

The maximum aft body cap diameter (the diameter of the disc that seals the aft body bus onto which the c.g. actuation mechanism is mounted) is sensitive to changes in half-nose angle and

Table 7-5: The response of the main outputs of vehicle sizing to inputs

	Reaction to 10% increase in					
	Half-nose angle	Aeroshell diameter	Launcher fairing diameter	Control system mass fraction	Required longitudinal c.g. offset	Required lateral c.g. offset
Maximum aft body length	21%	20%	-7%	0%	-2%	-0.33%
$X_{c.g.}$ Aft Body	1%	10%	0.14%	0.57%	0%	0%
Maximum aft body cap diameter	11%	4%	5%	0%	-4%	-0.69%

less sensitive to changes in aeroshell and launcher fairing diameter. This parameter is calculated so that at maximum c.g. displacement the geometry of the aft body does not intersect the geometry of the aeroshell which has a certain thickness due to the inflated toroids and TPS layup the vertical component of which is given in this method as stacked toroid height. Increasing the half-nose angle relaxes said geometric constrains in nearly a 1:1 ratio. Increasing the aeroshell and launcher fairing diameters does so half as effectively.

7-1-6 Limitations

The sizing method uses only two points of reference, which makes the method questionable. Whether or not the characteristic ratios that were chosen for the estimation of various parameters are appropriate, descriptive, characteristic and scale linearly is not fully known. Similarly, the assumptions that were made to enable the calculations are based on little more than engineering intuition and would need to be thoroughly examined for this sizing method to be considered adequate.

The distance from the nose of the aeroshell to the interface with the c.g. offset mechanism was calculated as the height of the spherical inflation tank - the bulkiest part of the inflation system. (The dimensions of the tank have been scaled with inflation volume using the respective dimensions of the IRVE-3.) Given a tank that would fit closer to the nose of the aeroshell, the allowable length of the aft body would increase.

The estimated average length of the aft body assumes uniform mass distribution. If, instead, the more massive items would be packed closer to the fore of the aft body bus, there would be sufficient remaining length to allow for an aft body bus that can be extended to approximately $7m$ in length. (Given a maximum angle of attack of circa $27.5deg$ and at maximum lateral and longitudinal center of gravity displacements making the aft body longer than the indicated maximum would expose it to the flow.)

7-2 Design Logic

This section commences by investigating different actuation systems that could potentially be used to move the center of gravity by displacing the payload with respect to the aeroshell. Different actuation systems were investigated and it was noted that examples of load-bearing connections used for space applications were scarce. Therefore, examples in non-space applications were analyzed and redesigned for potential use on spacecraft. Both the actuation and linkage systems have to be simultaneously designed to ensure efficiency in weight and capability to both provide and constrain the required degrees of freedom.

7-2-1 Actuation Type

The possible actuation methods belong to three general categories: hydraulic, pneumatic and electrical actuation. These actuation systems are discussed below.

- **Hydraulic** actuation focuses on the engineering uses of fluid properties and exists in aircraft systems and maritime crafts. It can deliver large actuation forces, but is susceptible to leaks. Leakage of fluids is a common failure and is potentially dangerous. The application of hydraulic systems in space compounds the risk due to the high heating experienced in entry maneuvers. The payload is a pressurized system with an-oxygen rich environment that enables explosive decompression. Furthermore, the harsh vacuum and low temperature environment poses additional potential risks (e.g. freezing of hydraulic fluid) that require mitigation strategies. Hydraulic systems also tend to be relatively heavy when compared to electrical actuation systems.
- **Pneumatic** actuation focuses on the application of pressurized gas and is widely used in a variety of systems. Compressibility of gases is a major concern. If high loads are experienced compressibility and potential vibrations become increasingly important.
- **Electrical** actuation is primarily used in space application due to a lower system mass relative to pneumatic and hydraulic systems. Therefore, this actuation system will be prioritized during the design of the actuation system [37].

7-2-2 Possible Actuation Systems

Many conceptual design options can be created as a mechanical linkage between the payload and aeroshell. In the following, several concepts have been developed to provide and constrain the degrees of freedom required between the payload and aeroshell to deliver vertical and lateral translation of the center of gravity.

Ball Joint with Actuation Cords

In Figure 7-1 a conventional ball joint was considered which would provide the payload with two degrees of rotational freedom. The ball joint would bear the principle loads and the proposed cords would provide the actuation. Ball joints require lubrication which introduces complications due to the space-vacuum environment This design provides no rotational resistance to a moment M_y and needs constraining. Strings can only be loaded in tension, thus during performance half the strings are not used (when resisting M_x, M_z). This suggests over-design or poor efficiency. Due to the unpredictability of load transfer through the inflatable aeroshell, loads may concentrate on a few cords at a particular time, leading to potential failure of cords. According to simulations in [38], the flow in the wake of the aeroshell becomes fully turbulent and oscillatory vibration of the cords require a damping system.

Hydraulic/Pneumatic Pistons

In Figure 7-2 a hydraulic/pneumatic piston system can be used to actuate the distance and relative angle between the payload and aeroshell through the control of each pistons' respective length. The

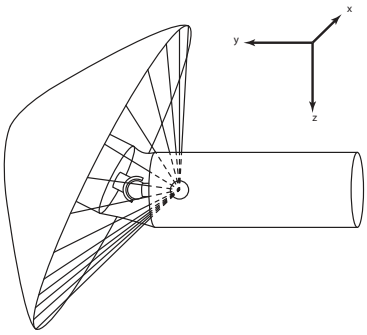

Figure 7-1: Ball Joint with Actuation Cords

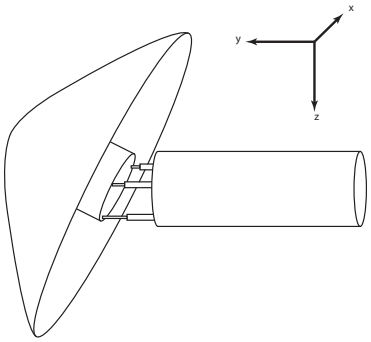

Figure 7-2: Hydraulic/Pneumatic Pistons

main advantage of such a system is the capability to provide 3 degrees of translational freedom to the center of gravity. The principle concern of this design is the relatively heavy weight of hydraulic/pneumatic systems [37]. Furthermore, pistons require structural support to resist shear loading (F_x and F_z) which needs an even heavy system weight. Common failures of hydraulic systems are leakages which are subject to the aggressive space environment [37]. To compound this danger, the payload is a pressurized, oxygen-rich environment. Space vacuum may help to accelerate leak-out rate (or out-gassing for pneumatics). Low temp environment and heating upon entry can lead to contraction and expansion of the hydraulic fluid or pneumatic gas, leading to further complications.

A proposed adaptation is to use electrically actuated pistons with structural supports seen in Figure 7-3 that enable better resistance to shear loading.

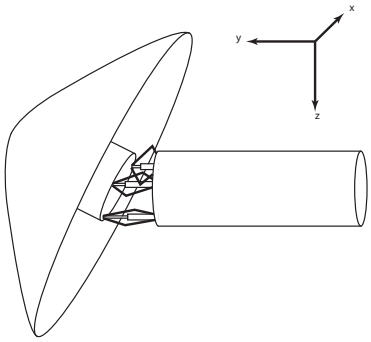

Figure 7-3: Electrical Pistons

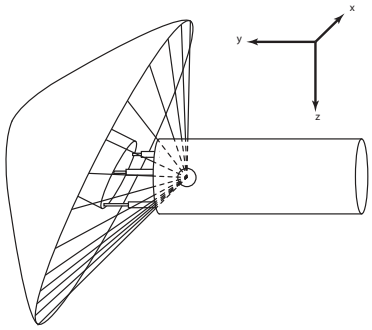

Figure 7-4: Shock Absorbers with Actuation Cords

Shock Absorbers with Actuation Cords

In Figure 7-4 the actuation system is similar to Figure 7-2, however the pistons are replaced with shock absorbers and the actuation is performed using cords. The main advantage is the capability of 3 degrees of translational freedom for the center of gravity. Shear loads (F_x and F_z) can be transfered as tension loads along the cords. If cords cannot be practically designed to bear the shear loading then structural supports such as the ones applied in Figure 7-3 would be required. Moments M_x and M_y applied to the aeroshell would induce tension loads into the cords where similar concerns as in Figure 7-1 also apply. The use of shock absorbers imposes conflicting requirement where they have to be rigid enough to withstand loads and vibrations, but

flexible enough to enable the cords to pull and actuate each shock absorber's respective length. The shock absorbers are effectively spring systems and therefore require a damping system. Also, if pneumatic shock absorbers are used then, similar problems to Figure 7-2 occur where the gas is influenced by the vacuum and low temperature of space and the heating experienced during entry. To control these influencing factors, the complexity of the system must be increased.

Hinge on Rotating Disk

In Figure 7-5 the aeroshell is attached to a hinge which provides the c.g. shift with 1 degree of translational freedom. The second degree of freedom is provided by the rotating disk which is mounted on the payload. The actuation method is absent from Figure 7-5 however, the envisioned actuation method uses two inflatables on either side of the hinge. Controlling the inflation/deflation of each respective inflatable would effectively determine the angle between the payload and aeroshell. A potential concern is the time required for active inflation and deflation since the inflation system would be incomparable to IRVE (where 115s till full pressurization was required [39]). Another concern would be the compressibility of the airbag if moments M_x and M_y were applied, however an alternative actuation device can be proposed if this problem persists. Shear loads F_x and F_z concentrate stress along the hinge line but structural supports (struts similar to Figure 7-3) can be added if required. To constrain rotation around the $y-axis$ which the rotating disk provides, a braking/locking mechanism is required.

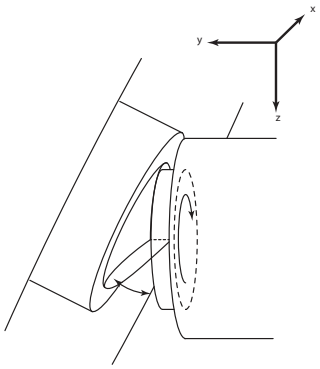

Figure 7-5: Hinge on Rotating Disk

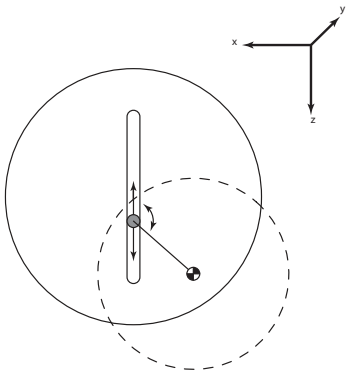

Figure 7-6: Single Rail with Lever Arm

Single Rail with Lever Arm

In Figure 7-6 the aeroshell is attached to the lever arm which provides the center of gravity with lateral translational freedom. The second degree of freedom is provided by the rail which enables vertical translation of the center of gravity. The poor shear capability of a single lever arm (against F_z and F_y) would require structural struts for support however they would also need to be placed on rails. A design concern is the poor resistance to moments M_x and M_z which will translate to a tension and compression force along the cross section of the lever arm. Currently there is no redundancy in the design and significant modifications are required to ensure reliability.

Double Rail System

In Figure 7-7 the payload is attached to a set of vertical rails while a set of horizontal rails are attached to the aeroshell. The horizontal and vertical rail sets are attached by pin wheels accompanied by a breaking/locking mechanism. Sets of rails are used to distribute stress over a larger surface. This system provides the required 2 degrees of translational freedom to the center of gravity. Actuation of the payload/aeroshell along the rails are envisioned to be performed using

electrical motors that drive the pin wheels along the respective rails. Design concerns are the braking mechanisms required along the rail to ensure constrained translation along the rail due to shear forces F_x and F_z. Additional concerns are the high power required to actuate the rails, unless the shear forces from flight paired with controlled rail braking can be used for actuation. Also, point load transfer through the pin wheels may lead to failure stresses, however an increase in the number of rails per vertical/horizontal set may solve this concern. This design option would be recommended for further study in the continuation to the detailed design. Reasons for this are as followed. The angle between the payload and the aeroshell remains constant, this is favorable for modeling as less uncertainties are introduced. Furthermore, a derivative of this rail system was already proved on the IRVE 3 to perform a successful shift of the center of gravity. Unlike the other design options, the double rail system provides the 2 degrees of freedom necessary and does not introduce unnecessary freedom that then needs constraining. E.g. Freedom of rotation around $y - axis$ of Figure 7-1.

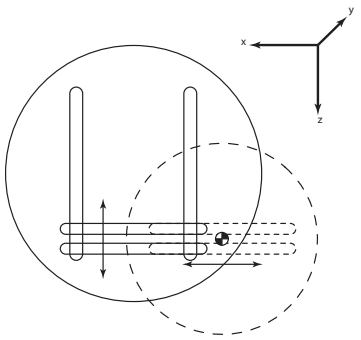

Figure 7-7: Double Rail System

7-2-3 Technology Readiness Level

This section concerns the technology readiness level of actuation systems that exist for space applications. The double rail system presented in Figure 7-7 has already been proven to work on a smaller scale HIAD - the IRVE-3. For the IRVE-3, the aft centerbody is attached to the fore centerbody by an actuated rail system. The system creates a radial center of gravity offset through the relative translation of aft to fore centerbody [40]. During flight performance, actuation of the rails to execute the offset of the center of gravity required one second [3]. This was performed using an entry mass of $281kg$. Though the actuation rail system used in IRVE-3 may not be directly scalable, the technology readiness level is high which lowers the developmental risk involved if such a system was potentially chosen for the detailed design phase. Entry loads were transferred through Bellville washer stacks that connected the rail system. Due to the connections used, small linear and angular deflection were measured at peak dynamic pressure to be 0.1 ± 0.003 deg (between nose and aft centerbody) [40]. This alerts potential technical risk when the entry mass concerned is higher at 10 tons with higher expected entry loads. For a more detailed technical risk assessment structural modeling needs to be performed where the rail system can be simulated as a spherical spring damper that is connected between the fore and aft centerbody.

Relevant to Figures 7-1, 7-5 and 7-6, joints that can be used to provide 1 or 2 degrees of movement can be derived from the shoulder joint of the Canadarm. The shoulder joint and subsequent joints are all composed of "basic elements called a joint one-degree-of-freedom or JOD" [41]. JODs are motor-driven gearboxes that include their own brakes and joint motor speed control. Again this may not be directly scalable to use for the design mission, however the technology readiness level is moderate. It is comparatively lower than the double rail system as application on HIADs has yet to be demonstrated.

7-2-4 Reliability, Availability, Maintainability and Safety (RAMS)

System reliability reflects the ability to perform and maintain functions in routine circumstances as well as unexpected circumstances. This translates to the redundancy of the actuation system and if a fail safe or safe life design approach is followed. Although a reusable and recyclable spacecraft is ultimately desired, it must be noted that this design reflects a precursor mission. Thus, the actuation system must be able to withstand only the short aerocapture and descent to landing maneuvers. Consequently, redundancy in design should not be exaggerated and a safe life approach will be followed. Furthermore, the following list ranks the design options concerning their potential reliability.

Reliability Ranking:

1. Double Rail System, Figure 7-7
2. Electrical Pistons, Figure 7-3
3. Shock Absorbers with Actuation Cords, Figure 7-4
4. Hinge on Rotating Disk, Figure 7-5
5. Ball Joint with Actuation Cords, Figure 7-1
6. Single Rail with Rotative Arm, Figure 7-6

Design availability is the degree to which a system is ready and in a committable state at the start of the mission. It is greatly determined by the technology readiness level of system components. As already mentioned the technology readiness level is highest for the double rail system since it has already been demonstrated on a smaller scale HIAD, the IRVE3.

Maintainability refers to the ease at which a system can be maintained. This is of a lower concern for the actuation system for a precursor mission since actuation is mainly performed during aerocapture and EDL. These maneuvers are currently expected to take approximately $271s$ and $400s$ respectively, and only occur for Mars arrival and return. A safe life approach will be taken, therefore, no maintenance will be required prior to the retirement of the spacecraft.

Safety critical functions are introduced into a system to prevent, or stop the development of undesirable events, unacceptable risk of physical injury or damage, either directly or indirectly on systems or individuals. Safety critical functions range from physical to non-physical (e.g. software) and can be simple or complex systems. Safety critical functions are required for the high loads experienced upon mars including the long transfer time during interplanetary flight were performance characteristics should not deteriorate. These safety critical functions include:

- Physical systems to take into account vibration loads that will be experienced and mitigate these to avoid discomfort of passengers and structural damage or fatigue.
- The actuation system should be designed with materials with good thermal properties to avoid significant degradation of material properties with varying temperature. If heat were to penetrate the TPS to a higher degree than expected it should not weaken the actuation system's structure nor conduct too much heat to the payload. This may require specialized coating or thermal insulation.
- Physical systems should be implemented to take into account the effects of the space environment. Vacuum conditions may require certain out-gassing mitigation techniques and low temperatures may cause certain metals to have an unacceptably low fracture toughness.
- Radiation and Ionization should be taken into account to avoid damage to both actuation system and payload. This may also require avoiding the use of certain composites that can be damaged by free radicals.
- Redundancy policy where extra structural elements are included that provide alternative load paths in case of unexpected loading or damage of existing structure.
- Safety factor where load-bearing capabilities are designed with a safety margin applied to the design loads (thermal, mechanical and vibrational that).

- Sensors should be included so that the health of the spacecraft can be monitored. (e.g. If actuation system is damaged during aerocapture, the crew can know not to immediately proceed with EDL). These may include strain gauges and displacement and temperature sensors.

7-2-5 Conclusions and Recommendations

The actuation design space was explored and several design concepts were discussed. Due to time constraints, in-depth structural analysis cannot be performed on all concepts within the design space. Therefore, a quantitative trade-off will not be performed, however, a recommendation will be made for an actuation design which shows the greatest potential. The DSE road map plans to invest current and future efforts towards the recommended design option for this potential. Due to lack of resources and time, sizing and analysis will proceed for the recommended design unless major difficulties or obstacles make the sizing and analysis of the recommended design option impossible.

The recommended design for detailed analysis is the double rail system, depicted in Figure 7-7. This design is recommended for the following reasons:

- Center of gravity offset is not accompanied by a change in the angle between payload and aeroshell. This simplifies modeling which is highly desirable.
- A similar rail system was already successfully demonstrated on the IRVE-3 so the technology readiness level is relatively high.
- Exactly two degrees of freedom are provided by the rail system, so it does not provide more degrees than necessary (that would then require constraining).
- Greater adaptability for redundancy and therefore reliability and safety.
- Good packing capability. (The payload and aeroshell can physically be closer due to small width along the aft body axis).

7-2-6 Electrical and Hardware Definition (Electrical and H/W Block Diagram)

To determine the hardware required for the actuation design as per recommendation, one can form a case study using the similar rail system found on IRVE3. The general components required for such a system are listed below:

- Sliding rails
- Pin connectors
- Payload adapter and aeroshell adapter connectors
- Electrical motor
- Motor speed control
- Braking/locking System
- Rail displacement/velocity sensors
- Electrical discharge controller
- AC/DC converter.
- Electrical power source (Battery)

The block diagram in Figure 7-8 conveys the mutual relations and interactions between the system components of the actuation system. In summary, the state of the rails is estimated by sensors which then feed the actuation system commander. This ultimately gets its commands from the GNC, but to conform to regulations manual control is possible. Prior to translation between the rails, the locking/braking mechanism has to be released to allow the motor to translate the payload with respect to the aeroshell. This is a loop since actuation may be required to be incremental, where the locking/braking mechanism is released and the rails are displaced, then the rails are locked again and the loop is repeated until the desired offset is achieved.

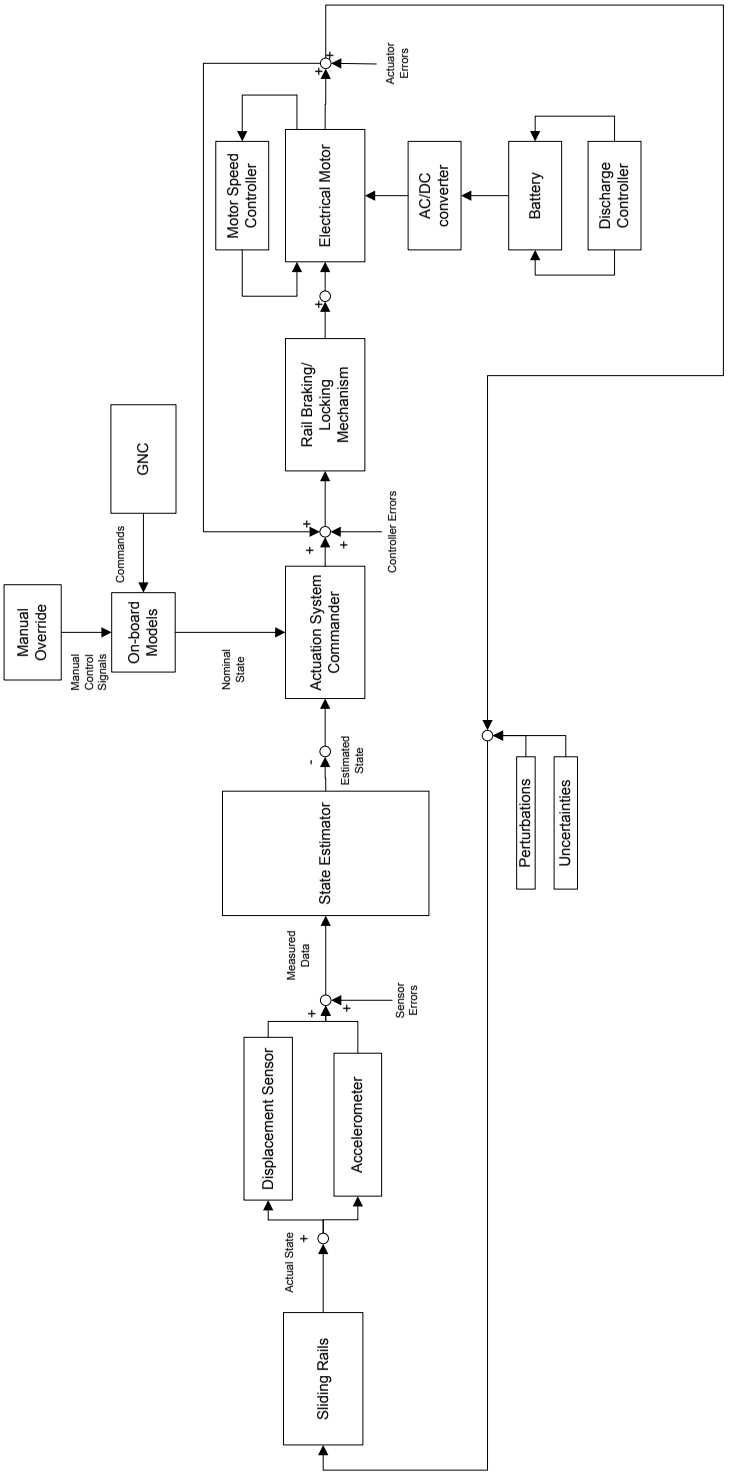

Figure 7-8: Hardware Block Diagram

7-3 Expected Loading

This section involves modeling the forces experienced by the entire spacecraft during the entry and descent to landing maneuvers. The resulting forces are represented on a free body diagram and the resulting internal shear force, internal normal force and internal moment at the actuation system are determined. The maximum internal force and moments are determined from trajectory calculations and a recommendation will be given to design for these maximum loads. EDL is used over aerocapture because it was determined in the trajectory analysis to encounter the largest deceleration and therefore the internal shear force, normal force and moment will be highest for EDL.

In a simplistic approach, the external forces acting on the aeroshell, payload and actuation system can be respectively identified as either a resultant vector or a distributed force. The forces acting on the payload and actuation system are only the centrifugal force and weight. The aeroshell has both the centrifugal force and weight acting as distributed loads with the addition of lift and drag acting as resultant vectors at the center of pressure. Since the spacecraft is using the Martian atmosphere to decelerate, the sum of forces is not equal to zero. Instead, the sum of forces is equal to the product of the mass and the acceleration along the specific position along the trajectory. The principle of D'Alembert is applied where the resultant $m_t a_t$ is applied as an equal but opposite force on the spacecraft free body diagram.

Primary Assumptions

PA5 Uniform mass distribution over payload, actuation system and aeroshell.
PA6 All forces are transferred through the actuation system's connections.
PA7 The model is only valid for equilibrium of forces (i.e. trim conditions) and does not take into account dynamic perturbations.
PA8 Aerodynamic forces on the aeroshell are introduced to the payload through the aeroshell adapter.
PA9 Aerodynamic forces are not exerted on payload.

The complete spacecraft is modeled in a free body diagram given in Figure 7-9, where the respective forces are all shown as resultant vectors for illustrative purposes. When modeling, all the forces are distributed forces except for the Lift and Drag which are applied as point forces. Note that flight path angle γ is the angle between the free stream flow and the local horizontal. α is then the angle between the free stream flow and the body axis.

To analyze the forces acting on the actuation system, it is convenient to decompose all forces into the body reference frame of the spacecraft. This is conveyed in Figure 7-10 for illustrative purposes, where in calculations the forces are simply multiplied by a rotation matrix given in Equation 7-1. With respect to forces in the actuation system, although the aerodynamic forces act at the center of pressure of the aeroshell, they are introduced to the actuation system via the aeroshell adapter. Therefore, in Figure 7-10 the aerodynamic forces are placed along the aeroshell adapter and a moment is produced as a result of the translation of these forces.

$$T = \begin{bmatrix} cos(\alpha) & sin(\alpha) \\ -sin(\alpha) & cos(\alpha) \end{bmatrix} \tag{7-1}$$

If the internal shear force is modeled along the spacecraft, three sections can be distinguished; the aeroshell, the actuation system and the payload. Equations for the distributed load (δn) of the spacecraft as a function of the axial length are given in equations 7-2, 7-3 and 7-4. This distributed

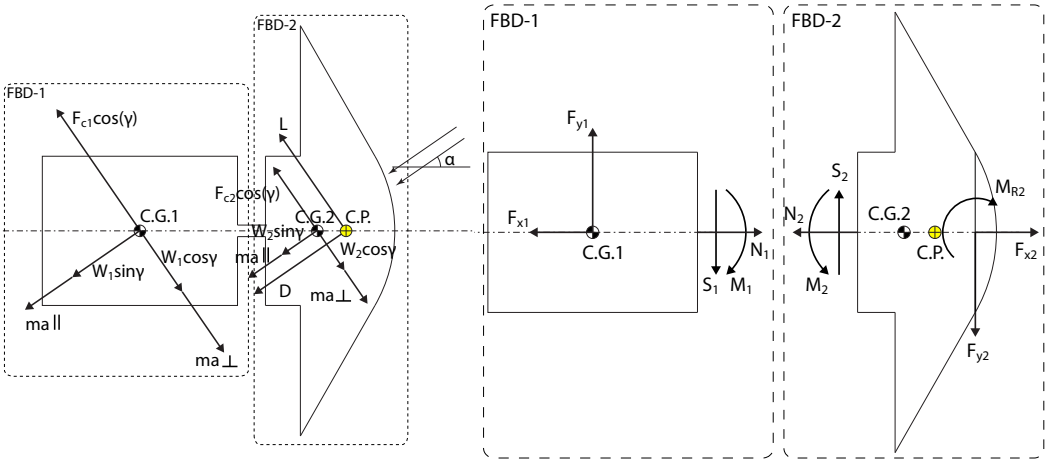

Figure 7-9: Free Body Diagram of Spacecraft in Trim Conditions

Figure 7-10: FBD of Spacecraft in trim conditions in body axis

load takes into account the centrifugal force acting on the body of mass (δm).

$$\delta n_{payload} = ((g - \frac{V^2}{R})cos(\gamma) + a_{\perp}) \cdot \delta m_{payload} \tag{7-2}$$

$$\delta n_{actuator} = ((g - \frac{V^2}{R})cos(\gamma) + a_{\perp}) \cdot \delta m_{actuator} \tag{7-3}$$

$$\delta n_{aeroshell} = ((g - \frac{V^2}{R})cos(\gamma) + a_{\perp}) \cdot \delta m_{aeroshell} \tag{7-4}$$

The internal shear force (v) along the spacecraft can be determined by integrating the distributed loading along the axial length of the spacecraft. This is given by Equation 7-5. The internal moment (M) along the spacecraft can similarly be determined by integrating the internal shear force equation, given by Equation 7-6.

$$v = \int_0^{x_1} \delta n_{aeroshell} + \int_{x_1}^{x_2} \delta n_{actuator} + \int_{x_2}^{x_3} \delta n_{payload} \cdot dx \tag{7-5}$$

$$M = \int_0^{x_3} v \cdot dx \tag{7-6}$$

When analyzing the normal/axial force (N) an identical procedure is followed that results with Equation 7-7.

$$N = \int_0^{x_3} (-gsin(\gamma) - a_{\shortparallel}) \cdot \delta m \tag{7-7}$$

7-3-1 Results and Conclusions

When determining the internal shear, internal normal force and internal moment distribution along the spacecraft, the aerodynamic forces along the trajectory path were used. This effectively analyses the internal moment and forces at every point along the trajectory for varying angles of attack. Only the maximum shear force and normal force distributions will be given. These are not indicative for the maximum stresses because superposition between the forces and moments may cause a maximum stress to occur where shear forces and moment may not individually be maximum. For maximum stresses further analysis of the exact structural shape of the actuation system is required.

The maximum forces and moments are summarized in Table 7-6.

Table 7-6: Maximum Loads Encountered on EDL

Shear [kN]	28.76	$\alpha = 19.0\ deg$
Normal [kN]	375.12	$\alpha = 9.5\ deg$
Moment [kNm]	-258.57	$\alpha = 19.0\ deg$

For illustrative purposes the shear and normal force distribution is given in Figure 7-11. Note that left-to-right on the $x - axis$ corresponds to the payload end to aeroshell tip - the orientation displayed in Figure 7-10. The first kink in both shear and normal force diagrams at $4.25m$ corresponds to the location of the aeroshell adapter. The second noticeable fact is that due to the assumption PA8 (aerodynamic forces are transferred at the connection point between aeroshell and payload) the loads after this location are relatively small.

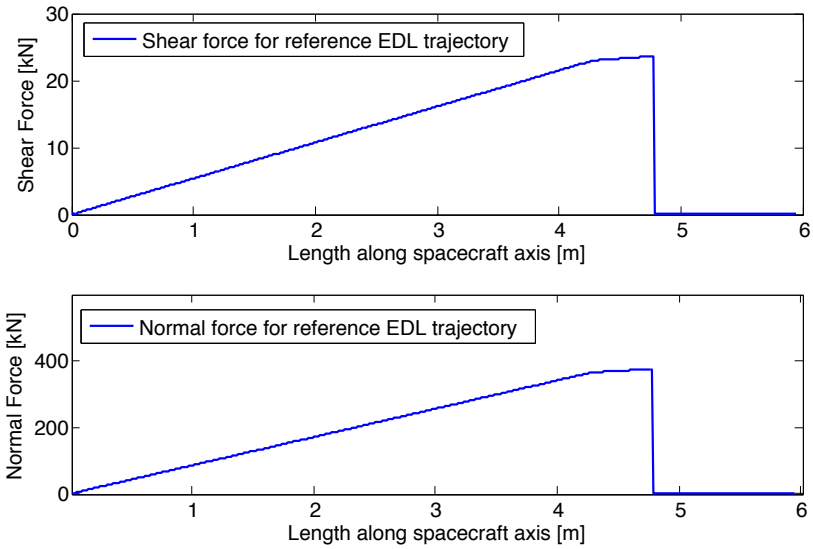

Figure 7-11: Maximum Shear and Normal Force Distribution Along Spacecraft Body Axis

7-3-2 Limitations, Risk and Sensitivity

Due to limited experimental analysis that exists on related inflatable re-entry vehicles, validation data cannot be obtained for the design loads presented in subsection 7-3-1. Lack of validation data for design loads increases technical risk and must be mitigated by experimental testing. Unfortunately, this must be left for future endeavors. A simple, smaller verification check can be performed by inspecting whether the internal normal and shear forces are zero at both ends of the spacecraft, of which they are. Although we know the maximum internal shear, normal force and moment, the physical design of the structure has to take into account the superposition of stresses. The maximum loads to design for are not the maximum values presented in subsection 7-3-1 since superposition of lower loads may lead to the highest overall stresses.

The assumption of uniformly distributed mass is an idealization that would practically be difficult to produce. Therefore, the loading distribution and resulting stresses obtained from these results will differ slightly in reality. This concerns mainly the internal moments, since the shear force only depends on the total mass and not its distribution. This sensitivity analysis cannot be currently performed because it depends on finalizing the spacecraft design so that the mass of every element can be exactly positioned and is further limited to the producibility of the design.

The assumption of equilibrium of forces does not always exist as the spacecraft cannot always be in trim conditions. Perturbations and maneuvers will cause a deviation from trim conditions and loading during those phases is not included/considered in the design loads. Additionally, forces and stresses do not always transfer efficiently or equally resulting with stress concentrations. Thus a safety factor will be applied to the design loads to ensure that the likelihood of failure remains low, thus lower the overall technical risk.

Design loads are wholly dependent on the trajectory of the EDL maneuver. Therefore, the magnitude of the loading experienced on the spacecraft is very sensitive to the steepness of the descent of the maneuver. However, if angle of attack (α) or flight path angle (γ) is varied, the internal forces/moments are less sensitive to these changes since relatively small angles are encountered (α varies from $\approxeq 9.5$ to $19deg$).

7-3-3 Control Mechanism Mass Feasibility Study

After basic comparison between the different center of gravity offset options and the recommendation of the double-cg-offset rail system, a simple structural analysis is performed to check whether this option is actually feasible. The purpose of this section is not to present the optimal structure of this control mechanism concerning weight and cost, but to investigate its feasibility given mass constraints and applied loads. In this analysis a general set of assumptions are taken as stated below:

PA10 Each rail mechanism carries the full loads as calculated at the midpoint on the outside surface of the aeroshell inflation system cap. Since, in reality, there will be two (or more) rails placed far apart to reduce the effects of bending this is a valid assumption and will result in a conservative estimate.

PA11 Highest loads act simultaneously. This provides a good safety factor since the highest loads do not occur at one point in the trajectory.

PA12 An additional safety factor of 10% is added to each load because of the uncertainty of this design phase.

Sizing Method

The initial values for some of the dimensions of the mechanism are set intuitively with analysis performed to recalculate said values and make the resulting load-bearing structure sufficiently strong. Figure 7-12 shows the cross-section of the rail and t-beam. The forces in the figure are as they act on the aeroshell side of the connection. For the case of the rail connected to the aft body cap the shear force will act 'into the page' and will therefore result in smaller stresses on the rail and the sliding mechanism because of the greater moment of inertia. It is advised to remember which color corresponds to which part and how the sections are named.

The starting width of the t-beam (blue) that slides in the rail (red), is chosen to be $5cm$, its thickness $2cm$ and its length $10cm$. Titanium is the material of choice due to its favorable properties with regards to density and strength [42]. The design loads will not be taken from the highest shear force, normal force, and bending moment encountered from the final reference trajectory presented in subsection 7-3-1. Instead the highest loads are calculated using the non-optimized trajectory, EDL3 presented in Section 5-5. This results in a shear force of $63kN$, a compressive normal force of $360kN$ and a moment of $240kNm$. These loads are taken to estimate the required dimensions and resulting mass of the mechanism. The rationale of using the loads encountered in the non-optimized trajectory is to design with a safety factor to increase reliability. In the event that perturbations cause the spacecraft to deviate from the reference trajectory, the structural design should still perform without failure or damage under the higher loads. The shear force is of the greatest concern and is 119% higher for the non-optimized trajectory while the normal force and moment are only 4% and 7% lower respectively.

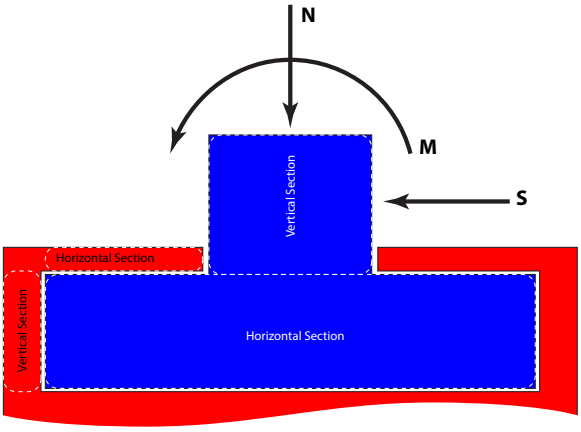

Figure 7-12: Cross-section of control mechanism; the sliding t-section beam is shaded blue and the guiding rail is shaded red.

The first step in the sizing process then, is to consider the stresses on the rail with respect to its thicknesses using basic stress formulas. The first main formula is the Euler-Bernoulli (symmetric) bending formula in Equation 7-8, where M is the moment about a cross section, y is the distance from the neutral axis which is chosen to be the maximum distance in analysis, I is the moment of inertia about the neutral axis (parallel to the moment vector):

$$\sigma = \frac{M \cdot y}{I} \tag{7-8}$$

The laterally uniform shear stress distribution formula [43] is stated in Equation 7-9, where F is the shear force on a cross section. If the shear force vector is vertical then b is the width of the cross section, d is the height of the cross section and y is the vertical distance from the neutral axis to the shear stress location. During analyses y is equated to zero to obtain the maximum shear stress value:

$$\tau = \frac{6F\left[\left(\frac{d}{2}\right)^2 - y^2\right]}{b \cdot d^2} \tag{7-9}$$

The third main formula used in the thickness estimation is the force-per-area formula for direct normal stresses in Equation 7-10 where F is the direct normal force and A is the area of the cross section on which the force is acting:

$$\sigma = \frac{F}{A} \tag{7-10}$$

After sizing the structure for stresses, the buckling of the vertical section of the t-beam (blue) is checked. Also its natural frequency is analyzed to prevent excitation due to acoustic vibrations at entry. The final step is to determine the power required to actuate the mechanism and the mass associated therewith.

Sizing Process

To begin with, we determine what the thickness of the vertical part of the rail should be to withstand the shear load. It is assumed that at maximum extension the overlap between the t-beam and the rail is only $10cm$. This parameter will be varied in later stages to see how the mass of the entire mechanism changes. The resulting thickness was relatively small compared to

the starting dimension, but the normal stresses in this part as a result of the shear force creating a moment on the lower corner of the vertical section of the rail require a larger thickness. To calculate this moment it is assumed that the resultant of the shear load distribution on the vertical section of the rail acts through its middle. Applying Euler bending results in a minimum thickness of $4.5cm$. Since this dimension seems to be too large compared to the width of the horizontal section of the t-beam (blue), the thickness of the horizontal is increased from $10cm$ to $20cm$ at this stage.

The next step is to check the required thickness of the vertical section of the t-beam. The combination of a direct compression load and a 'compressive moment' will require a thickness of $12.4cm$ for the beam not to fail under compressive stress at the edge of its vertical section. The shear stress due to the shear force with this thickness is below yield stress. The length of the horizontal section of the rail is then known since it is constrained by this dimension. The length of each horizontal section of the rail (red) is then $3.8cm$.

The bending moment on the t-beam will cause distributed loads on the rail and floor. A distributed load couple will be directed up and down, located left and right in the rail respectively (directions are consistent with Figure 7-12). It is assumed that the resultant of the left-up force distribution acts at half of the distance of the horizontal section of the rail. This force will create a moment about the corner of the rail and thus normal stresses. Applying Euler-Bernoulli gives a thickness requirement of $15.6cm$. It is also noticeable that due to this moment the same forces are applied on the horizontal section of the t-beam (blue) (Newton's Third Law) and so the same thickness is required for the horizontal section of the t-beam. It should be noted that in reality not only the horizontal sections will take the distributed loads due to the bending moment but also the vertical sides and the floor since the sliding mechanism is now far from being thin-walled. This outcome should be reconsidered in further analyses.

In the first step the vertical section of the rail was sized based on a height of $2cm$. However, this dimension has changed and we must use the new height (15.6 cm) to obtain the new thickness. Based on this new height the new thickness of the vertical section of the rail is $8.6cm$. This is obvious since a longer web will encounter a larger moment at its corners due to the shear force. For each section of the rail shear analysis is again performed and it can be shown that with these thicknesses the rail does not fail due to shear.

The vertical section of the t-beam will not be fully constrained by its sides (the two horizontal sections of the rail). Therefore an analysis on its buckling is performed using Euler's beam buckling as seen in Equation 7-11, where L is the length of the beam, F is the buckling normal force, I is the lowest moment of inertia of the cross section of the beam, E is Young's modulus of titanium, K is the constant which specifies the condition of the boundaries of the beam. Even though the part is a fixed-fixed beam, for extra safety a pinned-pinned beam is assumed and thus $K=1$. Inserting the highest compressive load results in a maximum length of $19m$. This means buckling will not be an issue.

$$F = \frac{\pi^2 \cdot E \cdot I}{(K \cdot L)} \tag{7-11}$$

The same vertical section is also analyzed for vibrations. Its natural radian frequency is calculated by modeling the part as a beam with lateral stiffness with natural frequency given in Equation 7-12:

$$\omega_n = \sqrt{\frac{k}{m}} \tag{7-12}$$

Here it is assumed that the analyzed part is massless and that the vibrating mass (m)is the total spacecraft mass. In Equation 7-12 k is the deflection stiffness of a cantilever beam. Its length is chosen to be the thickness of the horizontal section of the rail ($15.6cm$). The resulting natural frequency is $153Hz$. The resistance to vibration loads should be developed further in future

analyses by checking how the mechanism withstands launch vibrations. This is because if the structure is able to survive launch vibration loads, it will be able to survive the entry acoustic vibrations [44].

The power that is required to drive the actuation mechanism depends on a) the forces that have to be overcome, b) the speed at which the t-beam has to be displaced and c) the nature of the actuation mechanism. The forces that have to be overcome by the motor in the direction of the motion of the t-beam are the maximum shear force and the maximum friction force. The required displacement speed is $10cm/s$ as calculated in the control section of this report. To calculate the friction force it is assumed that friction is independent of area and velocity[45]. This friction is caused by the maximum compressive normal force. The coefficient of friction is taken from friction table of titanium on titanium [46]. Taking a simple rack-and-pinion system where the t-beam is actuated through a cutout in the rail by means of a solid gear connected to an electrical motor yields a required power of approximately $2.7kW$. Most electrical motors provide high rpm and low torque so a reduction mechanism would be necessary and the total mass of one engine-reduction system would be circa $20kg$. So, taking two engine-reduction systems per cap gives a total of four engine-reduction systems and the added mass of $80kg$.

Results and Discussion

To have a clearer picture Figure 7-13, Table 7-7, Table 7-8 and Table 7-9 summarize the results of this conservative design approach. Thicknesses are indicated with the letter t and a number index and critical locations are indicated with numbers.

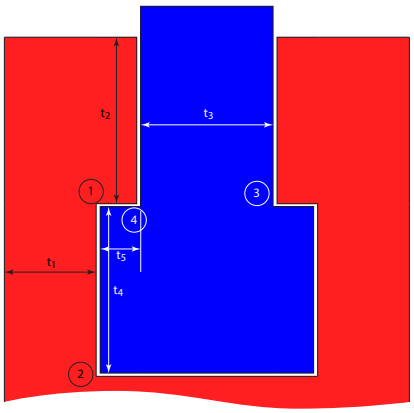

Figure 7-13: Cross section of the rail and sliding mechanism.

Table 7-7: Dimensions of the rail and t-beam produced by a single sizing iteration

Symbol	Name	Dimension [cm]
t_1	Rail Vertical Section Thickness	8.6
t_2	Rail Horizontal Section Thickness	15.6
t_3	T-beam Vertical Section Thickness	12.4
t_4	T-beam Horizontal Section Height	15.6
t_5	Rail Horizontal Section Length	3.8

The mass of the rail is calculated assuming a rail length of 65 cm. The motor mass is typical for the chosen type of motors that deliver the power calculated in the sizing section.

As can be seen from the results the masses are very large given the constraint of $1000kg$ for the complete control and decelerator system. However, it must be emphasized that this analysis is extremely conservative. The large resulting mass is a direct outcome of the accumulation of such assumptions as:

Table 7-8: Stresses on the critical locations of the produced by a single sizing iteration

Location Number	**Shear Stress** $[MPa]$	**Normal Stress** $[MPa]$
2	24.2	1045
1, 4	172	1070
3	16.8	1062
Titanium Strength (yield)	760	1070(compression)/1100(tension)

Table 7-9: Masses of the Control System

Part Name	**Mass** $[kg]$
(1) Rail	189
(1) T-beam	13.8
(1) Electrical motor + reduction system	10
Total control mechanisms + motors	891

SA1 Any single rail + t-beam couple can carry the full loads.
SA2 Peak loads are applied simultaneously.
SA3 Both sides of the connection (aft body-cap- and aeroshell-cap-mounted) have to be able to withstand maximum loads.
SA4 Thickness is uniform and therefore maximal for every section.
SA5 Only a small part of the rail (the overlap between the t-beam and the rail) takes the loads.
SA6 The initial values for the dimensions are picked intuitively, which may result in a higher overall mass than if another set of initial values is taken. This is especially true for the length of the overlap since it is assumed to be constant throughout actuation.

As a consequence of the conservatism of these assumptions, especially the latter, the same sizing procedure was performed with a number of different starting values for the overlap, now requiring that each rail-beam couple only carries half the loads (the loads are still taken at the midpoint of the aeroshell cap, so that the effects of the bending moment are still ultra-conservative). Imposing simple constraints for the minimum lengths of the t-beams given their actuation with a rack-and-pinion method and the maximum required longitudinal and lateral center of gravity offsets, taken formSection 8-6 led to a **minimum** mass of $370kg$ for the entire system (mass of motors and reduction systems included.) More than halving the mass while relaxing only two of the conservative assumptions leads us to believe that with more time and appropriate optimization methods the mass of the entire system can be brought down to approximately $200kg$. The requirement of a $1000kg$ deceleration and control system might then likely be met.

Limitations and Uncertainties

There are certain limitations to this approach. The most glaring limitation is the lack of verification and validation. Due to time constraints the method described above has not been presented to a specialist for feedback and approval. The inability to prove this method's accuracy by experiment or through verification with other proven models make the conclusions not very reliable.

Another noticeable limitation is the neglect of failure theories (i.e. Distortion Energy Theory, Strain Energy Theory) which are crucial [47]. Another phenomenon that is not taken into account are stress concentrations at edges and corners. Furthermore, the locking mechanisms that would hold the t-beam in place and the means of attaching the rails to the aeroshell/aft body caps are also not taken into account.

Distributed forces in the rail created by the moment on the t-beam have been treated as two concentrated forces with approximate lines of action where the two forces apply. The relevant line of action (the one acting on the rail) was assumed to be through the middle of the horizontal rail

part. Assuming a concentrated force through that line of action may have been acceptable at the beginning of the small iteration when the lateral dimensions were large compared to height. When the height dimension increased, however, the same method may deviate significantly from reality. This makes the method less reliable still.

Risk and Sensitivity

The concept of shifting the center of gravity to control the system may seem simple but has a high consequence if certain structural and actuator failures occur. Failure in the motor results in the loss of control of the entire spacecraft. Losing control of the vehicle jeopardizes the mission. The likelihood of this occurring is decreased by using two motors at each interface where each motor is able to produce the required power.

Failure in the rails and connections is even more catastrophic. This is because such failure will cause the shield to detach. For this reason the analyses performed on the structure considered only one of the two rail mechanisms at each interface. This will then provide redundancy.

Though the connection of the control structure to the aeroshell and aft body caps is not considered in this stage of the analyses, it is of great importance since its failure would lead to the detachment of the aeroshell and disintegration of the vehicle at hypersonic velocities. The control structure in its current definition does not provide any strategies on how to tackle this risk.

The analysis of the control structure is sensitive to load cases and thereby to the chosen trajectory. Flying steeper trajectories will induce higher loads on the control structure. If the changes in the loads are significant then this will influence the mass and architecture of the structure. However, small deviations in loads will not be lead to significant changes in design or final mass estimate since they are already taken into account with safety margins and the underlying conservatism of the approach.

Chapter 8

Guidance and Control

The primary aim of this chapter is to develop a controller capable of following the aerocapture and EDL trajectories specified in Chapter 5. A second aim is to determine the feasibility of the control concept. The third objective is to provide actuator requirements that are needed to design the center of gravity offset mechanism. The dynamic system is first explored in Section 8-1, after which a linear model is developed to gather an initial understanding of the changing conditions in the system. Thereafter a control strategy is developed and a controller is designed. The last sections deal with testing the controller and the longitudinal performance of the system through a Simulink® simulation, which allows the implementation of a non-linear system.

8-1 Theory

This sections introduces the theory used throughout the remainder of the chapter. The relevant frames of reference, assumptions, and equations of motion used for both the linearized and the non-linearized approaches are defined. An analysis on the effects of center of gravity offset on the system during flight is presented.

8-1-1 Frames of Reference

The inertial reference frame used is centered about Mars, and is depicted in Figure 8-1. This inertial frame defines the angles and dimensions necessary to describe the position of the spacecraft with respect to the center of Mars. Figure 8-2 shows a longitudinal kinematic diagram and a free body diagram of the spacecraft. The direction of forces as well as the relevant attitude angles are defined. All forces and angles are displayed in positive direction. The subscript b refers to the body frame, subscript s refers to stability frame and m denotes the Martian frame.

8-1-2 General Assumptions

The assumptions used throughout this chapter are:

PA1 The vehicle is assumed to be entirely symmetric with respect to the body axis X_b. According to this assumption $I_{xy} = I_{yz} = I_{xz} = 0$. The equations for these terms are given in Equations 8-1 to 8-3. Due to the very small expected changes in c.g., these values can be neglected.

$$I_{xy} = m \cdot \Delta x \Delta z = m \cdot \delta cg_{x,aft} \delta cg_{z,aft} \tag{8-1}$$

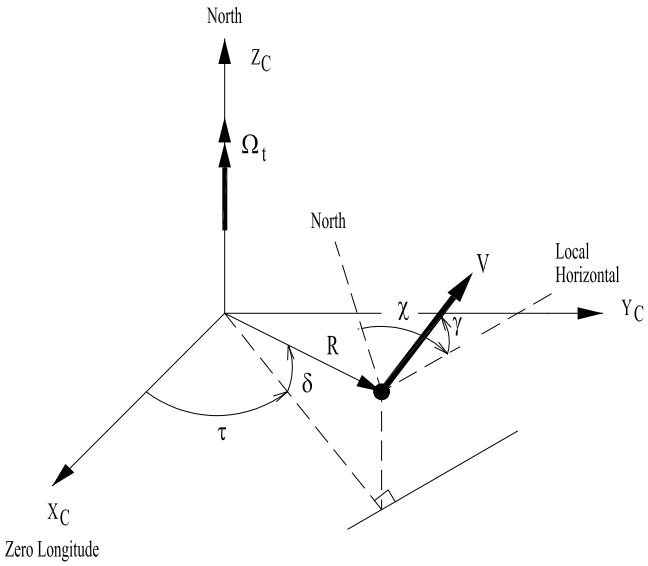

Figure 8-1: Representation of Inertial Frame of Reference [48]

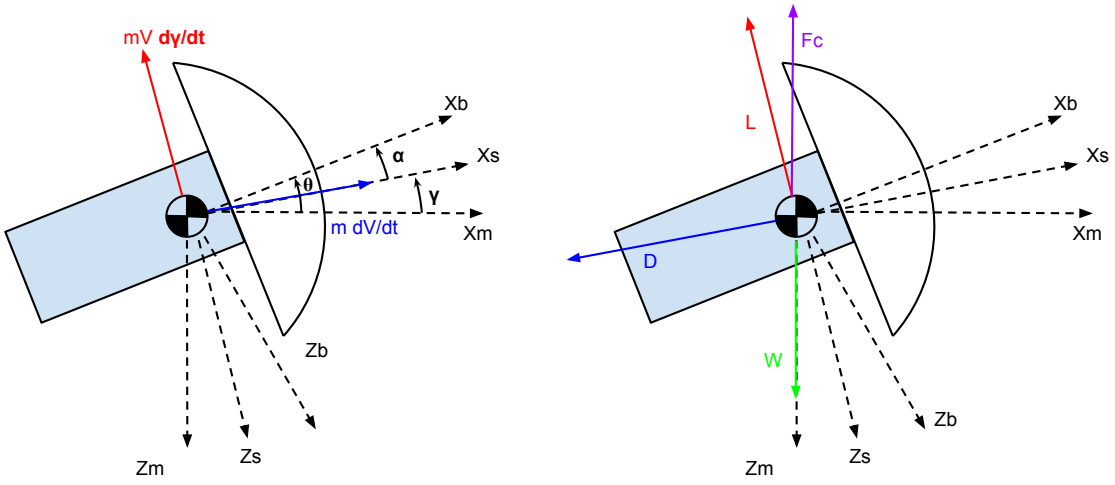

Figure 8-2: Longitudinal Kinematic Diagram (left) and Free Body Diagram (right)

$$I_{yz} = m \cdot \Delta y \Delta z = m \cdot \delta cg_{y,aft} \delta cg_{z,aft} \tag{8-2}$$

$$I_{xz} = m \cdot \Delta y \Delta x = m \cdot \delta cg_{y,aft} \delta cg_{x,aft} \tag{8-3}$$

PA2 Mars is non-rotating, $\Omega_t = 0$. This assumption allows the model to neglect Coriolis Force and centripetal accelerations induced by the motion. The assumption is valid due to the high velocity of the return vehicle with respect to the rotation of Mars.

PA3 Mars is spherical and has a uniform mass distribution. This simplification allows the application of the model anywhere on the Martian surface, independent of its exact location. The J_n effects are ignored.

PA4 The spacecraft is flying along the equator, $\delta = 0$**,** $\chi = 90°$. This assumption simplifies the equations of motion further and narrows the problem to a situation whereby the spacecraft travels along the equator.

PA5 The dynamic coefficients are linearly dependent on α **and** β. This assumption allows for a simpler representation of the force and moment coefficients, as derived in Section 4-4.

8-1-3 Equations of Motion

The equations of motion used throughout this chapter have been extracted from [48] and are listed in this section. The equations follow from the assumptions in subsection 8-1-2. Together, these equations can describe the motion of the spacecraft throughout re-entry so that it can be modeled, and a controller can be simulated.

Equations 8-4, 8-5 and 8-6 are the **dynamic equations for translational motion** for a general body of mass. The first two result directly from the kinematic diagram and free body diagram presented in Figure 8-2. Equations 8-7 to 8-9 are the **kinematic position equations** that track the position of the spacecraft relative to the center of Mars, illustrated accordingly in Figure 8-1. The **rotational motion equations** about the body axis (roll, pitch, and yaw) are given in Equations 8-10 - 8-12. Finally, the **attitude equations**, which describe the angle of attack (α) (for which the longitudinal equation can be derived from the kinetic diagram in Figure 8-2), the sideslip angle (β), and the bank angle (μ) are provided in Equations 8-13 - 8-15.

$$\dot{V} = -\frac{D}{m} - g \sin \gamma \tag{8-4}$$

$$\dot{\gamma} = \left(\frac{V}{R} - \frac{g}{V} \right) + \frac{(L \cos \mu - S \sin \mu)}{mV} \tag{8-5}$$

$$\dot{\chi} = \frac{V}{R} \cos \gamma \tan \delta \sin \chi + \frac{(L \sin \mu - S \cos \mu)}{mV \cos \gamma} \tag{8-6}$$

$$\dot{\delta} = \frac{V \cos \gamma \sin \chi}{R \cos \delta} \tag{8-7}$$

$$\dot{\tau} = \frac{V \cos \gamma \cos \chi}{R} \tag{8-8}$$

$$\dot{R} = V \sin \gamma \tag{8-9}$$

$$\dot{p} = \frac{M_x}{I_{xx}} + \frac{I_{yy} - I_{zz}}{I_{xx}} qr \tag{8-10}$$

$$\dot{q} = \frac{M_y}{I_{yy}} + \frac{I_{zz} - I_{xx}}{I_{yy}} pr \tag{8-11}$$

$$\dot{r} = \frac{M_z}{I_{zz}} + \frac{I_{xx} - I_{yy}}{I_{zz}} pq \tag{8-12}$$

$$\dot{\alpha} = q - (p\cos\alpha + r\sin\alpha)\tan\beta - \frac{L - mg\cos\gamma\cos\mu}{mV\cos\beta} \tag{8-13}$$

$$\dot{\beta} = p\sin\alpha - r\cos\alpha - \frac{S + mg\cos\gamma\sin\mu}{mV} \tag{8-14}$$

$$\dot{\mu} = -\frac{p\cos\alpha + r\sin\alpha}{\cos\beta} - \frac{L - mg\cos\gamma\cos\mu}{mV}\tan\beta + \frac{L\sin\mu + S\cos\mu}{mV}\tan\gamma \tag{8-15}$$

Following assumption 4 from section 8-1-2 ($\delta = 0$, $\chi = 90°$), and the observation that they are decoupled from the other equations, equations 8-6, 8-7 and 8-8 will not be used for modeling.

8-1-4 Effect of Aft Body Shift and Moment Coefficients

Shifting the aft body shifts the center of gravity of the entire spacecraft ($c.g._{total}$), generating a moment. This analysis is performed assuming that the forces are in equilibrium in the trim condition, by acting through the center of gravity as depicted in Figure 8-3 for a c.g. shift in the xz-plane. Upon shifting the center of gravity to a new location, moments are generated until a new trim condition is reached. These moments are described in Equation 8-16, and the relative roll, pitch and yaw rates generated can be calculated using Equation 8-17. The moment analysis given in Equation 8-16 is similar to Petsopoulos [49], as well as the one from Reagan [19].

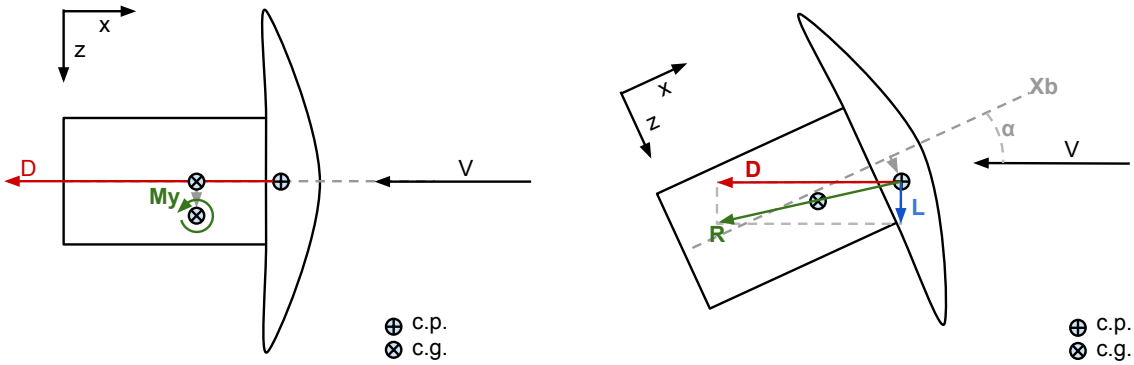

Figure 8-3: Depiction of trim conditions with forces acting at the center of pressure

$$\boldsymbol{M_{cgnew}} = \begin{bmatrix} I_{xx}\dot{p} \\ I_{yy}\dot{q} \\ I_{zz}\dot{r} \end{bmatrix} = \frac{m_{shifted}}{M_{total}} \begin{bmatrix} (\delta cg_{y,aft})N + (\delta cg_{z,aft})S \\ (\delta cg_{z,aft})A - (\delta cg_{x,aft})N \\ -(\delta cg_{x,aft})S - (\delta cg_{y,aft})A \end{bmatrix} \tag{8-16}$$

$$\begin{bmatrix} \dot{p} \\ \dot{q} \\ \dot{r} \end{bmatrix}_{cgshift} = \begin{bmatrix} 0 & \frac{N}{I_{xx}} & \frac{S}{I_{xx}} \\ -\frac{N}{I_{yy}} & 0 & \frac{A}{I_{yy}} \\ -\frac{S}{I_{zz}} & -\frac{A}{I_{zz}} & 0 \end{bmatrix} \begin{bmatrix} \delta cg_{x,aft} \\ \delta cg_{y,aft} \\ \delta cg_{z,aft} \end{bmatrix} \tag{8-17}$$

These equations use the Normal Force (N) and Axial Force (A), which are translated from the lift and drag by the rotational relationship about the Y_b axis given by Equation 8-18.

$$\begin{bmatrix} N \\ A \end{bmatrix} = \begin{bmatrix} \cos\alpha & \sin\alpha \\ -\sin\alpha & \cos\alpha \end{bmatrix} \begin{bmatrix} L \\ D \end{bmatrix} \tag{8-18}$$

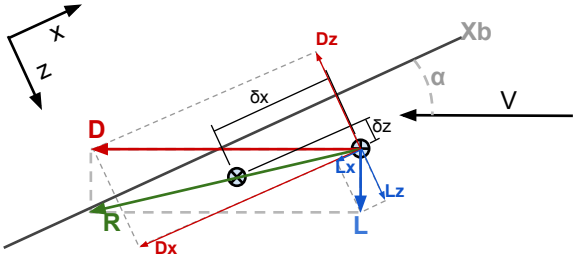

Figure 8-4: Forces acting through the center of pressure

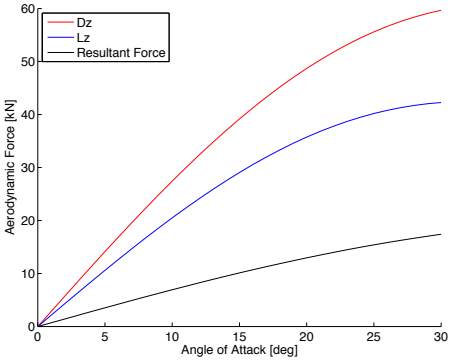

Figure 8-5: L_z, D_z and the resultant force in z-direction plotted for a change in angle of attack

The moment coefficients can be determined from the moment equation presented in Equation 8-16. The roll, pitch and yaw moment coefficient equations are given respectively in Equation 8-19, Equation 8-20, and Equation 8-21. Trim conditions for the spacecraft are defined when $C_m = 0$. This results in an equilibrium position that is illustrated in Figure 8-3, whereby the center of gravity is shifted such that the resultant force is acting through it.

$$C_l = \frac{m_{shifted}}{M_{total}} \left[\frac{\delta cg_{y,aft} - \delta cp_y}{l_{ref}} C_N - \frac{\delta cg_{z,aft} - \delta cp_z}{l_{ref}} C_S \right] \tag{8-19}$$

$$C_m = C_{m_0} + C_{m_\alpha}\alpha = \frac{m_{shifted}}{M_{total}} \left[\frac{\delta cg_{z,aft} - \delta cp_z}{l_{ref}} C_A - \frac{\delta cg_{x,aft}}{l_{ref}} C_N \right] + C_{m_\alpha}\alpha \tag{8-20}$$

$$C_n = C_{n_0} + C_{n_\beta}\beta = \frac{m_{shifted}}{M_{total}} \left[\frac{\delta cg_{x,aft}}{l_{ref}} C_S - \frac{\delta cg_{y,aft} - \delta cp_y}{l_{ref}} C_A \right] + C_{n_\beta}\beta \tag{8-21}$$

With a change in angle of attack, the center of pressure will shift, this effect is included in Figure 8-3. The aerodynamic forces are acting through the center of pressure causing a moment due to the moment arms δx and δz, this moment is given by Equation 8-22 and depicted in Figure 8-4. In Figure 8-5 it is given that D_z is more dominant than L_z, due to the high resultant force in z-direction it is important that dx is not overly large. This is included in the stability ratio of 0.3 that is discussed in subsection 7-1-1, which limits the center of gravity position in x-direction with respect to the nose and therefore with respect to the center of pressure in the x-direction.

$$M_{y_{cw+}} = D_x\delta z - D_z\delta x + L_x\delta z + L_z\delta x \tag{8-22}$$

However the moment analysis given by Petsopoulos [49] and Reagan [19] assumes that the center of pressure coincides with the initial center of gravity position, therefore assuming that δx and δz are zero. This assumption also holds for the applied approach. However, since C_{m_α} is calculated by the aerodynamic model with respect to the initial center of gravity, the effect of this assumption is diminished. The moment caused by the center of pressure around the initial center of gravity is applied within the Simulink model, therefore taking δx into account. Since δcp_z is assumed to be zero, the δz that is used in the Simulink model is affected and therefore only C_{m_0} will be affected by the remaining δz due to the c.p. shift. The same approach is valid for δz, δcp_y and C_{n_β} for a lateral center of gravity shift. Due to the symmetry of the spacecraft, C_{m_α} is equal to C_{n_β}, which is computed by the aerodynamic model given in Chapter 4 to be $-0.1603 rad^{-1}$.

8-1-5 Force Coefficients

The forces acting on the aeroshell are Drag (D), Lift (L), and Sideforce (S). These are calculated based on the force coefficient curves developed in Chapter 4, Aerodynamic Characteristics. The relationships are linearized below:

$$C_L = C_{L0} + C_{L_\alpha}\alpha \tag{8-23}$$
$$C_S = C_{S0} + C_{S_\beta}\beta \tag{8-24}$$
$$C_D = C_{D0} + C_{D_\alpha}\alpha + C_{D_\beta}\beta \tag{8-25}$$

Due to the symmetry of the spacecraft: $C_{L_\alpha} = C_{S_\beta}$, and $C_{D_\alpha} = C_{D_\beta}$. The values for the aerodynamic coefficients were taken from Section 4-4, and are given in Table 8-1. These values are used in both the Linear Model and in the Non-linear Model.

Table 8-1: Aerodynamic characteristics used throughout this chapter.

C_{L_α} [-/rad]	C_{D_α} [-/rad]	C_{L_0} [-]	C_{D_0} [-]	C_{S_0} [-]
-1.1952	-1.1739	0	1.6525	0

8-1-6 Moments of Inertia

The calculations for moment of inertia around the X_b, Y_b and Z_b axis are adapted from [50] and presented in Equations 8-26 - 8-29. The payload structure was approximated as a cylinder with uniformly distributed mass (subscript 'aft') attached to a hollow cone (the aeroshell). It is assumed that the aeroshell's center of gravity is always on the X_b axis. The dimensions used are illustrated in Figure 8-6 for the X_b-Y_b plane, and provided in Table 8-2.

$$I_{xx} = \frac{3}{10}m_{as}\left(R_{out}^2 - R_{in}^2\right) + \frac{1}{2}m_{aft}R_{sc}^2 + m_{aft}\left[\left(\delta cg_{y,aft}\right)^2 + \left(\delta cg_{z,aft}\right)^2\right] \tag{8-26}$$
$$I_{yy} = \frac{1}{10}m_{as}\left(h_{out}^2 - h_{in}^2\right) + \frac{3}{20}m_{as}\left(R_{out}^2 - R_{in}^2\right) \tag{8-27}$$
$$+ m_{as}\left(x_{cg,as}\right)^2 + \frac{1}{12}m_{aft}h_{aft}^2 + \frac{1}{4}m_{aft}R_{aft}^2 + m_{aft}\left(\delta cg_{z,aft}\right)^2$$
$$I_{zz} = \frac{1}{10}m_{as}\left(h_{out}^2 - h_{in}^2\right) + \frac{3}{20}m_{as}\left(R_{out}^2 - R_{in}^2\right) \tag{8-28}$$
$$+ m_{as}\left(x_{cg,as}\right)^2 + \frac{1}{12}m_{aft}h_{aft}^2 + \frac{1}{4}m_{aft}R_{aft}^2 + m_{aft}\left(\delta cg_{y,aft}\right)^2 \tag{8-29}$$

Table 8-2: Spacecraft Dimensions used for Moment of Inertia Calculation

h_{out}[m]	h_{in}[m]	R_{out}[m]	R_{in}[m]	$x_{cg,as}$[m]	R_{aft}[m]	h_{aft}[m]	m_{as}[kg]	m_{aft}[kg]
3.1234	1.8220	6	3.5	2.2163	4.2737	2.5	1000	9000

8-2 Open-loop Testing with the Linearized Model

Prior to developing a control strategy, the system is linearized and analyzed at different heights to gain insight on its natural stability and the expected responses for a given center of gravity offset. This section proceeds to extract the expected eigenvalues of the system, its stability and its performance over singular maneuvers. Since the motions are expected to be non-linear, the methods in this section are only valid for short time spans where it can be assumed that the system's parameters are constant. The maximum time span observed in this section is therefore 5 seconds.

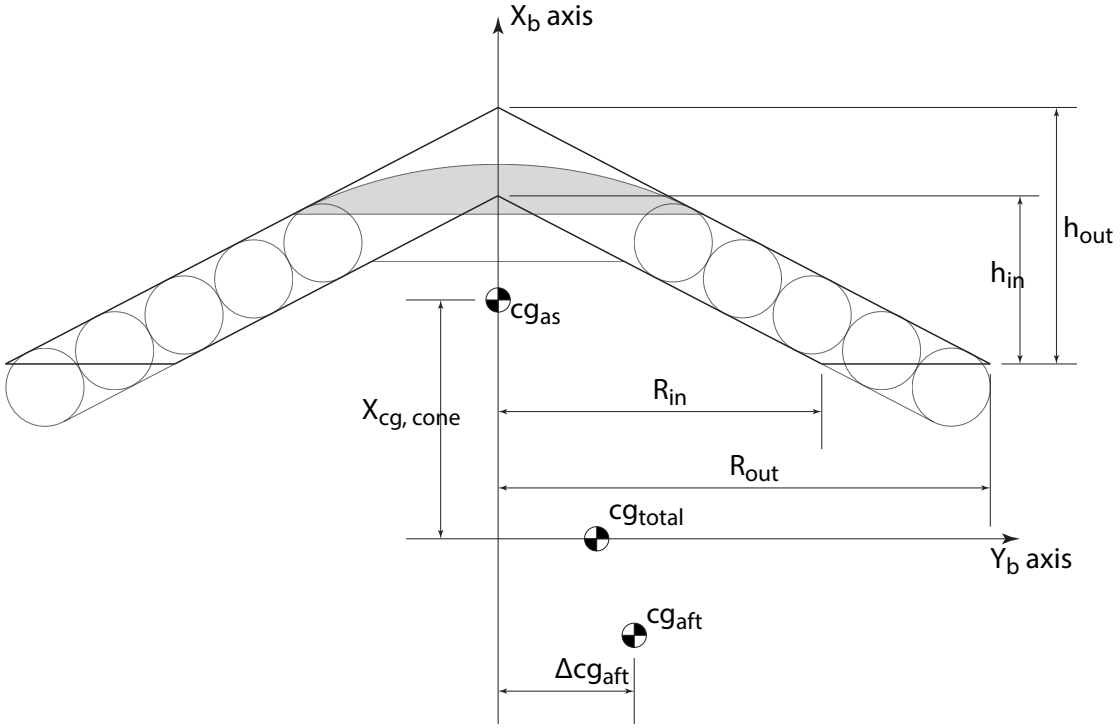

Figure 8-6: Dimensioning for Moment of Inertia Calculation

8-2-1 Linearized Equations of motion

The equations of motion have been linearized to a state-space format, so it can be analyzed with MatLab®. The linearization process is based on a first order Taylor expansion; the equations of motion presented in subsection 8-1-3 have been linearized to the format shown in Equation 8-34. The full extensive result of linearization process can be found in [48].

The linearized state-space format is presented in Equations 8-30 to Equation 8-31. Matrix A, the state matrix, is the result of a first order Taylor linearization. Matrix B, the control matrix, makes use of Equation 8-17 to affect $\dot{p}$, $\dot{q}$ and $\dot{r}$. Matrix C is an identity matrix and matrix D, the feedforward matrix, is set to $\mathbf{0}$.

$$\Delta\dot{\boldsymbol{x}} = A\Delta\boldsymbol{x} + B\Delta\boldsymbol{u} \tag{8-30}$$

$$\Delta\boldsymbol{y} = C\Delta\boldsymbol{x} + D\Delta\boldsymbol{u} \tag{8-31}$$

$$\boldsymbol{x} = \boldsymbol{y} = [V, \gamma, R, p, q, r, \alpha, \beta, \mu]' \tag{8-32}$$

$$\boldsymbol{u} = [\delta cg_{x,aft}, \delta cg_{y,aft}, \delta cg_{z,aft}]' \tag{8-33}$$

The general Taylor expansion to the first order is:

$$\boldsymbol{Y} = f(\boldsymbol{X_0}) + f_{x1}(\boldsymbol{X_0})\Delta x_1 \tag{8-34}$$

8-2-2 Eigenvalue Analysis

The open-loop eigenvalues of the system have been analyzed at different moments in the EDL trajectory and are presented in Figure 8-7 and Table 8-3. It can be seen that the eigenvalues consistently feature one conjugate imaginary pair and one real pair. The remaining eigenvalues are

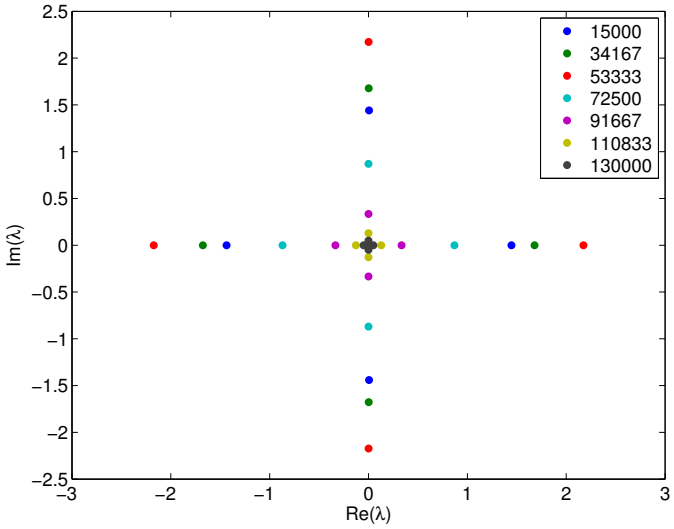

Figure 8-7: Plot of Eigenvalues of Matrix A at different altitudes (h) during EDL

Table 8-3: Table of eigenvalues of Matrix A at different altitudes (h) during EDL

h = 14986 $[m]$	h = 53294 $[m]$	h = 72437 $[m]$	h = 91622 $[m]$	h = 129910 $[m]$
0.0063 + 1.5942i	0.0014 + 2.4043i	0.0002 + 0.9622i	+ 0.3698i	+ 0.0543i
0.0063 - 1.5942i	0.0014 - 2.4043i	0.0002 - 0.9622i	- 0.3698i	- 0.0543i
1.6005	-0.0065	-0.0009	-0.0004	0.0006
-1.5879	-0.0006	-0.0004	-0.0001	-0.0004
-0.0218	0.0005	0.0004	0.0005	-0.0001
-0.0062	-2.4029	0.9624	-0.3697	0
0.0003	2.4057	0	0.3698	0
0	0	0	0	0.0543
-0.0014	-0.0001	-0.9620	0	-0.0543

either 0 or negligible. The eigenvalues separate further from the center as the altitude decreases; a maximum is reached at about 50 km altitude after which the eigenvalues decrease in magnitude. Eigenvalues that are larger in magnitude indicate that the system is more responsive to changes, so at very high altitudes the system is going to feature slow responses.

Following the relationships for Period (P) and Time to Half Amplitude ($T_{\frac{1}{2}}$) in Equation 8-35 and Equation 8-36, general remarks on the behavior of the responses can be made. The eigenvalues indicate that all motions are going to be either very aperiodic, or perfectly periodic; natural damping of motions is not to be expected, which means that the control system has to act to correct the oscillations, and the system cannot be expected to go back to an equilibrium state once an input is given.

$$P = \frac{2\pi}{Im(\lambda)} \tag{8-35}$$

$$T_{\frac{1}{2}} = \frac{ln\left(\frac{1}{2}\right)}{Re(\lambda)} \tag{8-36}$$

8-2-3 Step Input Tests

Maneuvers have been analyzed to gain an insight into the responsiveness and behavior of specific state variables during flight. To test the system at its maximum responsiveness, it was analyzed during the EDL trajectory at an altitude of 50km.

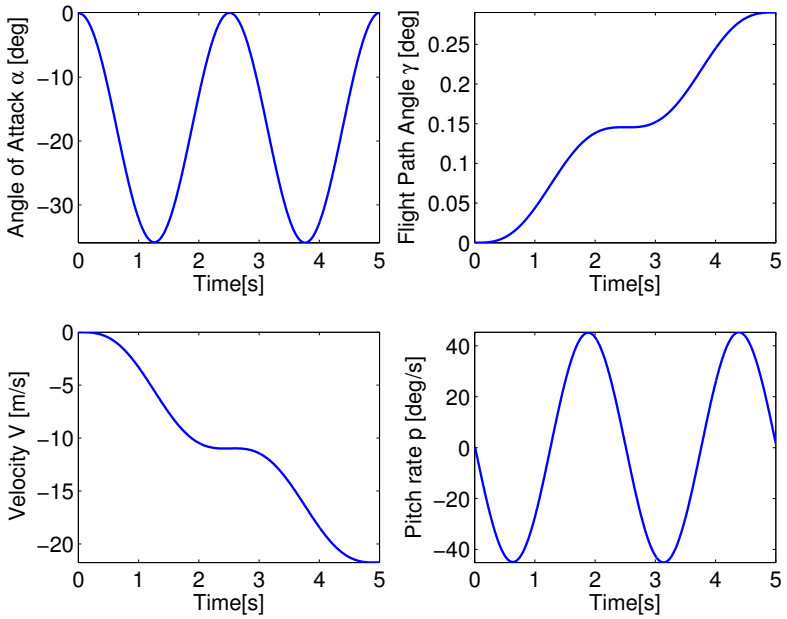

Figure 8-8: Angle of attack (α), flight path angle (γ), velocity (V), and pitch rate (p) response to $\delta cg_{z,aft} = -0.4m$ at $h = 50km$

Figure 8-8 shows the change in α, γ, V and p with a step-input of $\delta cg_{z,aft} = -0.4m$. It can be seen that α and γ show a fully periodic, undamped oscillation. The magnitude of the oscillation reaches $\alpha = 35deg$ within slightly more than 1 second, indicating that it is an eigenmode of the system. Aperiodic yet oscillatory responses are seen for Velocity and Flight path angle. The change in flight path angle is increased due to the lift that is produced with the implemented angel of attack. This increase in flight path angle then reduces the velocity.

Figure 8-9 displays the change in β, μ with a step-input of $\delta cg_{y,aft} = 0.1m$. Here, the change in the lateral orientation measurements indicate fully aperiodic motions. β increases to approximately $23deg$ within the first second. This indicates that the system is unstable which follows the conclusion drawn from the eigenvalue analysis of the A-matrix of the steady state model in subsection 8-2-2. Considering that this shift is only a quarter of the shift in α from Figure 8-8, it can be seen that the system is far more responsive laterally. This behavior can be verified by observing the attitude equations (Equations 8-13 to 8-15). Unlike α, however, the change is aperiodic and thus keeps on increasing rapidly if it isn't counteracted. This shows that a smaller center of gravity shift is needed in the Y_b axis than in the X_b axis to achieve the wanted results. Furthermore, it is noted that the change in μ is approximately a sixth of the change in β, indicating the relative responsiveness of the two factors.

8-3 Sensors & Data Handling

In order for the controller to work, the dynamic system must be capable of measuring the actual parameters of its trajectory during flight such that they can be compared to the ones of the desired trajectory. The sensor options that are to be used in the system, for the purpose of navigation and control, can be.

- **Inertial Measurement Unit (IMU) -** . The IMU is capable of measuring the accelerations acting on the spacecraft as well as its angular velocity [51]. Based on these raw values, the

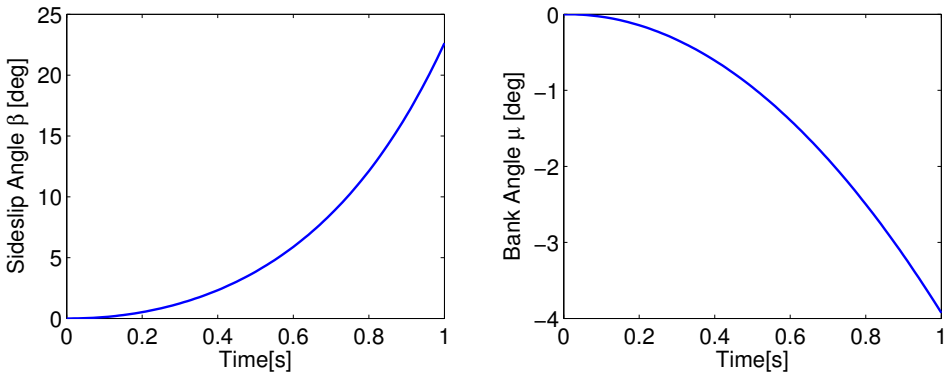

Figure 8-9: Sideslip Angle (β) and Bank Angle (μ) response to $\delta cg_{y,aft} = 0.1m$ at $h = 50km$

speed (V), orientation (γ) of the spacecraft can be determined, provided that initial conditions are given. The height (h) of the spacecraft can also be estimated by measuring the gravitational pull.

- **Mars Entry Atmospheric Data System (MEADS) -** . Used by MSL, MEADS is able to determine the spacecraft's orientation in a flow via pressure sensors placed on the shell. MEADS also provides atmospheric information, making it possible to determine the dynamic pressure (q_∞) [52]. The knowledge of the spacecraft within the flow can proveide information on the angle of attack (α) and the sideslip angle (β).
- **Rail Displacement Sensor -** This sensor, integrated within the structure, measures the relative position of the payload module with respect to the aeroshell and can thus determine the center of gravity of the spacecraft.

The three aforementioned systems should suffice in providing the controller with the information required for guided entry. As the emphasis is on a human precursor mission, no Mars based systems (such as on-ground station for radar control or GPS-like systems) are taken into account. Figure 8-10, the Data Handling Block Diagram, explains how these sensors are to be integrated in the controller.

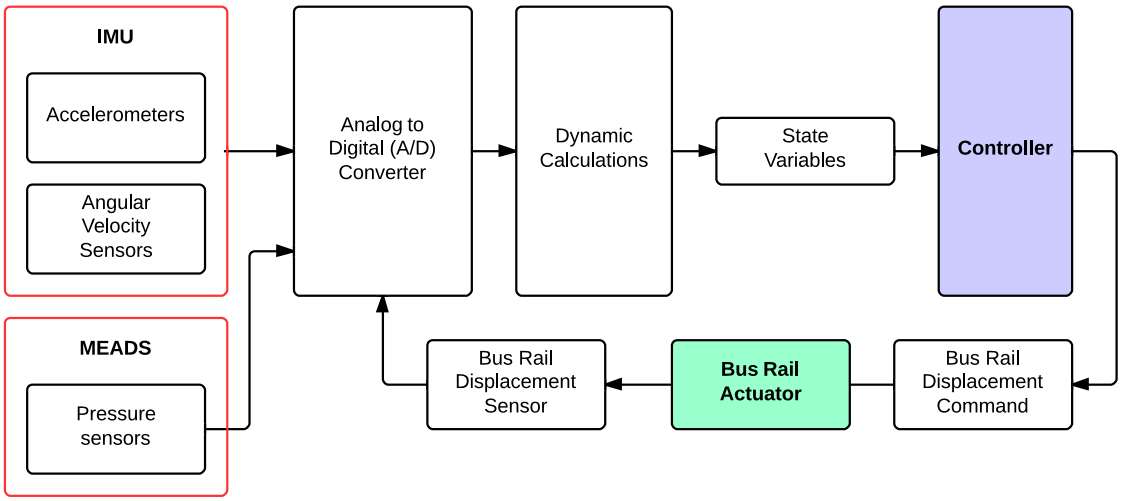

Figure 8-10: Data Handling Block Diagram

8-4 Control Strategy

Following the results from subsection 8-1-4, it is possible to see that the direct influence of the center of gravity offset is on roll, pitch, and yaw rate. This section defines the strategy that was followed to design a controller that can control the variables that are most important, using a double c.g. shift. The longitudinal and lateral cases were decoupled. The aim of the longitudinal controller is to eliminate the necessity for banking maneuvers by controller the lift vector using a changing angle of attack. The aim for the lateral controller is to keep the space craft going in a straight line when encountering atmospheric perturbations, using a side-slip angle to generate a side force. Based on these aims, the main parameters for longitudinal and lateral control were defined.

8-4-1 Main Parameters for Longitudinal Control

The main variables to control the space craft longitudinally vary during the different phases of the mission. To reach the final target apoapsis, aerocapture must ensure that the spacecraft exits the atmosphere with a specific combination of velocity (V) and flight path angle (γ). These two parameters are considered equally important. This is explained in more detail in Section 3-2. During the EDL phase, however, it is determined that the most important parameters to track are velocity (V), distance to center of mars (radius) (R), and ground-track (x_{gt}). In order to assure correct tracking both position and velocity have to be implemented in the controller logic. However, the velocity V is considered more important than the position h, x_{gt}. If these three parameters are successfully tracked then the spacecraft will hit the desired target-box. The main control parameters are summarized in Table 8-5, together with their order of importance.

Table 8-4: Main longitudinal parameters during Aerocapture and EDL

Phase	Main Parameters
Aerocapture	$V(1)$, $\gamma(1)$
EDL	$V(1)$, $R(2)$, $x_{gt}(2)$

8-4-2 Main Parameters for Lateral Control

In both EDL and Aerocapture the lateral controller has the job of ensuring that the latitude (δ) remains equal to 0° and the heading (χ) remains equal to 90°, such that the spacecraft remains on its trajectory on the equator. This logic is valid for both Aerocapture and EDL. Assuming that the entrance is correct, the controller's job is to correct for any instabilities that may occur. For this reason, it is decided that the most important parameters to be kept to zero are the lateral ground track (y_{gt}) and the bank angle μ. From these two, the position error y_{gt} is considered to be more important, since this determines if the target box is reached.

Table 8-5: Main lateral parameters during Aerocapture and EDL

Phase	Main Parameters
Aerocapture	$y_{gt}(1)$, $\mu(2)$
EDL	$y_{gt}(1)$, $\mu(2)$

8-5 Controller Design (S/W Block Diagram)

The controller aims to track the relevant parameters by affecting roll, pitch and yaw. It is built through a combination of Proportional-Integral-Derivative (PID) controllers. This section provides schematics of the controller designs that can be implemented in the system. Following the control

strategy, the longitudinal and lateral controller are decoupled. However, they can be combined in a global controller which acts in the two planes through one actuator and dynamic system. This system is expected to fly along the equator, and the longitudinal controller should only act to correct deviations. A discussion on the performance of the controllers can be found in Section 8-6 (Non-Linear Simulation).

8-5-1 Longitudinal Controller

The longitudinal controller tracks V, γ, R, and x_{gt}, which have been established to be the most important parameters. The errors observed in these parameters are not directly comparable, and the controller is designed to follow an order to translate between errors. The order is based on the general linearized trajectory control loop from [53]. The controller follows the logic order below:

$$x_{gt}, R \longrightarrow V, \gamma \longrightarrow \theta \longrightarrow \delta cg_{z,aft} \longrightarrow \text{Actuator} \longrightarrow \text{Dynamic System}$$

A schematic of the longitudinal controller is presented in Figure 8-11. The required x_{gt} and R are translated into gamma requirements via two separate PID controllers. The two are compared to the gamma output of the dynamic system, and the error in real gamma. All three errors are fed through a Switch Logic, which calculates a global error in γ. This error, in parallel with the actual error in γ measured by the system, goes through a PID controller and is translated into a desired θ command. The errors in θ, then go through a Switch Logic that outputs a final error. With a PD controller, this is translated into a final requirement for $\delta cg_{z,aft}$. This requirement then goes through the actuator, which acts as an amplitude limiter and a rate limiter, such that the controller acts within the physical limits of the rail system designed in Chapter 7. Since for aerocapture only V and γ are important, for this part of the mission the x_{gt} and R controllers are switches of using the switch logic. For the EDL these controllers are then switched on again.

8-5-2 Lateral Controller

The lateral controller follows a similar order as the longitudinal, but only lateral parameters are observed. The key parameters to control have been identified, as in subsection 8-4-2, as y_{gt} and μ. These parameters build up the controller, but they are treated independently, and their relative effect is only combined at the end. A Switch Logic is used to evaluate a final $\delta cg_{y,aft}$ to be used by the system. The commanded y_{gt} and μ are always 0, such that this system, ideally, should be able to correct for all errors, and keep the aircraft longitudinal. The form is given in the figure below. The controller can be seen in Figure 8-12. The logic used is:

$$\begin{aligned} y_{gt} &\longrightarrow \psi \longrightarrow \delta cg_{y,aft} \longrightarrow \text{Actuator} \longrightarrow \text{Dynamic System} \\ \mu &\longrightarrow \delta cg_{y,aft} \nearrow \end{aligned}$$

The lateral controller will be switched on in both the aerocapture, and the EDL.

8-5-3 Switch Logic

The switch logic presented in Figures 8-11 and 8-12 can be treated with four separate strategies, listed below.

- **Switch Logic Option 1: Maximum error**
  $err_{out} = max(err_{in})$. The largest error is selected. This forces the system to correct as much as possible to constantly minimize all errors.

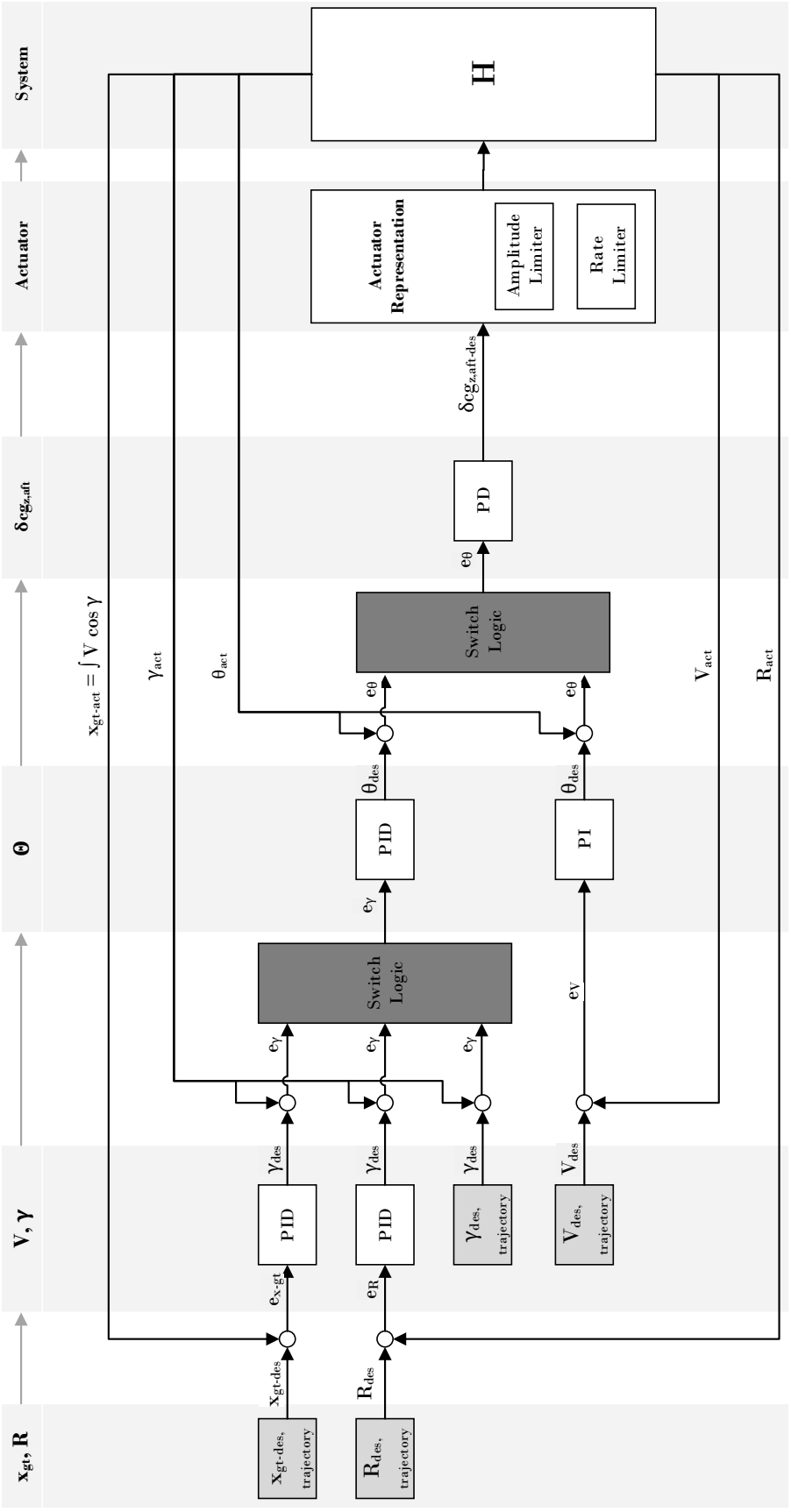

Figure 8-11: Longitudinal Controller

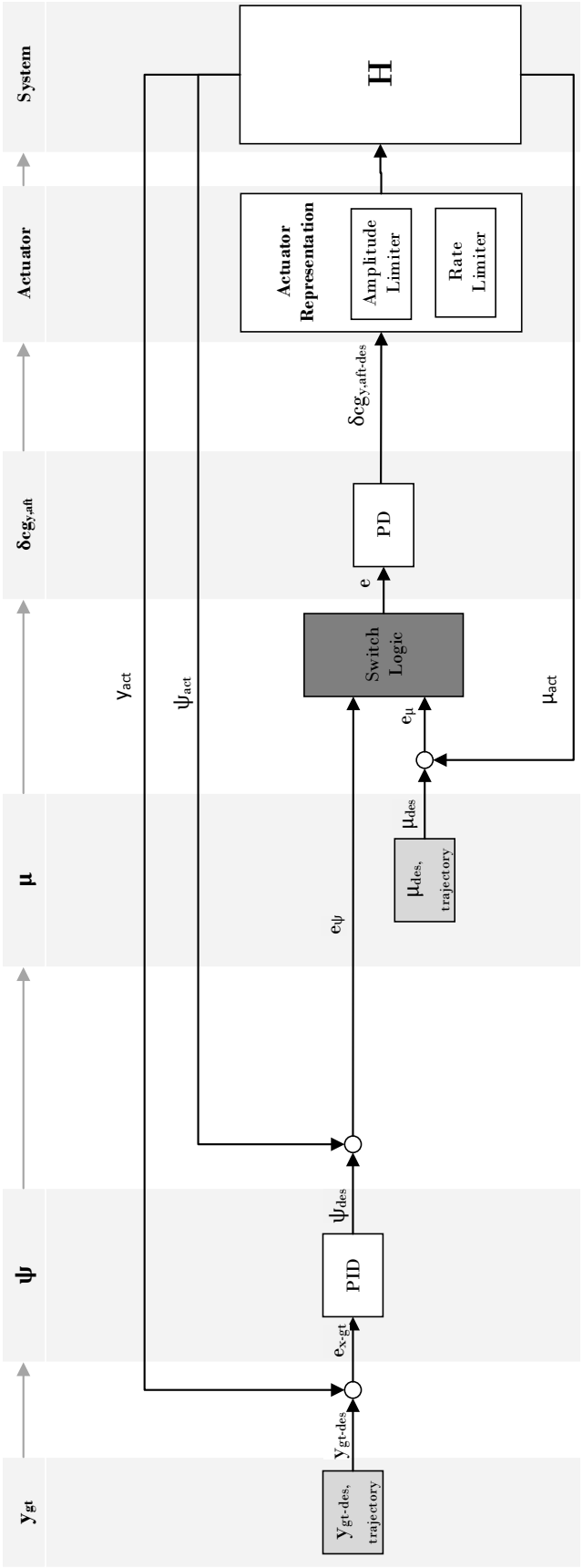

Figure 8-12: Lateral Controller

- **Switch Logic Option 2: Weighted maximum error**
  $err_{out} = max(weights \cdot err_{in})$. The largest error is selected, but the errors are weighed such that errors from more important variables are given more emphasis. This means that the controller focuses on the most important parameter unless the error in another parameter becomes large enough to require correction.
- **Switch Logic Option 3: Average error**
  $err_{out} = average(err_{in})$. An average of the three errors is calculated, this minimizes an issue whereby a large error in only one parameter forces the system to overreact.
- **Switch Logic Option 4: Weighted average error**
  $err_{out} = average(weight \cdot err_{in})$. This logic uses a weighted average whereby err_{out} is calculated. This allows to decide which parameter is most important to the controller, without fully neglecting the other ones. More complex versions of this switch logic can be implemented throughout different phases of flight (weight scheduling) to change the emphasis from one variable to another.

In Switch Logic Options 2 and 4 the weights of the errors have to be tuned, this makes it more difficult to backtrack errors in the controller should it not work properly. The advantage of including weights, however, is that a more general controller can be designed, and then set weight of parameters that do not need to be tracked to 0. Therefore, Switch Logic Option 2 is selected due to its simpler implementation than option 4; including an average error makes backtracking even more difficult.

8-6 Non-Linear Simulation

A non-linear dynamic system along with the controller described in Figure 8-11 have been set-up and implemented in Simulink®. They are to be used, as in Section 8-1, to evaluate the performance of the system. This section details the implementation. The system is verified and validated in its open loop condition to ensure that it was correctly integrated. After verification, the controllers are implemented. Due to time constraints, only the γ- and V- longitudinal controllers are implemented in Simulink. The reason is that the overall purpose is to provide requirements for the actuator mechanism and to asses the feasibility of the control concept, as opposed to determining the quality of the controller.

8-6-1 Dynamic System Implementation

In Simulink®, the spacecraft was represented using a dynamic system created using:

- The equations of motion from Section 8-1, Equation 8-4, Equation 8-5 and Equation 8-9 to Equation 8-15.
- The atmospheric model discussed in section Section 5-1.
- The relevant spacecraft dimensions described in Section 7-1.
- The aerodynamics characteristics from section Section 4-4.
- The equations for the moment of inertia, dependent on the CG shift, subsection 8-1-6.
- The effect of the centre of gravity shift on the moment coefficients as expressed in Equation 8-19 - Equation 8-21.

The result of this implementation was a non-linear dynamic system, with nine state variables as output, and a 3-axis center of gravity offsets as input.

$$input = [\delta cg_{x,aft}, \delta cg_{y,aft}, \delta cg_{z,aft}]'$$
$$output = [V, \gamma, R, p, q, r, \alpha, \beta, \mu]'$$

8-6-2 Verification of the Simulink® Model

The open-loop nonlinear model must be verified and validated to ensure it behaves correctly. In addition, this procedure provides a better understanding of the behavior of the spacecraft as a dynamic model. Verification is performed via two methods: by testing the system's behavior to a ramp input and by comparing the system to its linear counterpart.

Verification with a Ramp Input Signal

The test input signal is chosen to be a gradual centre of gravity offset in the negative Z_b direction, as displayed in Figure 8-13. At $t = 150s$, a ramp is introduced in the input signal. The final value of the input signal is $-0.4m$, which is the the expected center of gravity offset needed to create a trim angle of attack of roughly $20deg$ (as computed using Equation 8-37, a simplified form of Equation 8-20).

$$\delta cg_{z,aft} = -\frac{C_{m_\alpha} \alpha l_{ref}}{C_{D_o}} \tag{8-37}$$

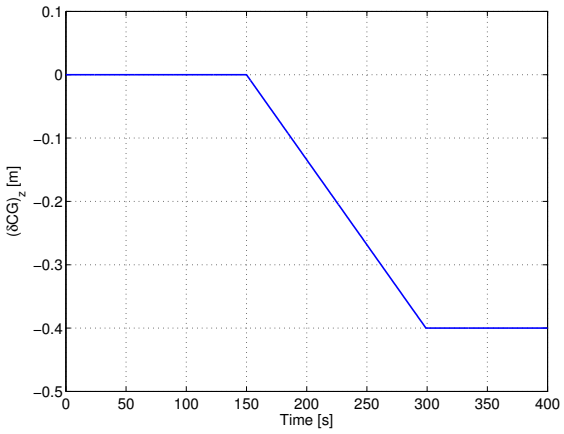

Figure 8-13: Input for a test simulation in the Simulink model.

V	γ	R	p	q	r	α	β	μ
4715 [m/s]	-10 [deg]	3519500 [m]	0	0	0	0	0	0

Table 8-6: Initial conditions for the test simulation.

The initial conditions used in this simulation are presented in Table 8-6. It is expected that the output trajectory and velocity resemble a ballistic EDL trajectory until the center of gravity offset is introduced, after which an angle of attack, and thus a lift force, is present. In turn, the lift force affects the flight path angle and the altitude. Figure 8-14 shows the speed and altitude during the test simulation. It can be seen that the space craft hits the denser layers of the atmosphere at $t = 100s$, and touches down at $t = 400s$.

Figure 8-15 and Figure 8-16 show the angle of attack, the flight path angle and the forces and moments acting on the spacecraft. All the variables displayed have a sign and an order of magnitude as expected from the defined direction of forces and rotations in Section 8-1. However, the angle of attack and especially the pitch moment generated show large fluctuations, which indicate that there is an instability present in the model.

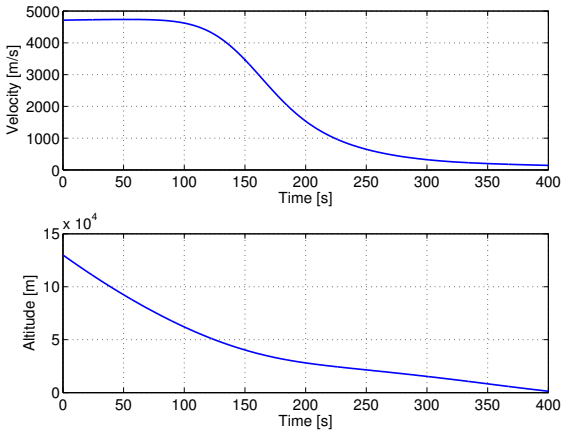

Figure 8-14: Output of the velocity and altitude.

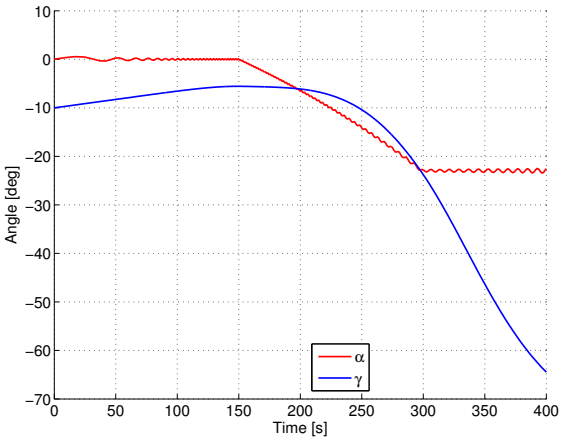

Figure 8-15: Simulation results for the angle of attack and flight path angle to test simulation input stated above.

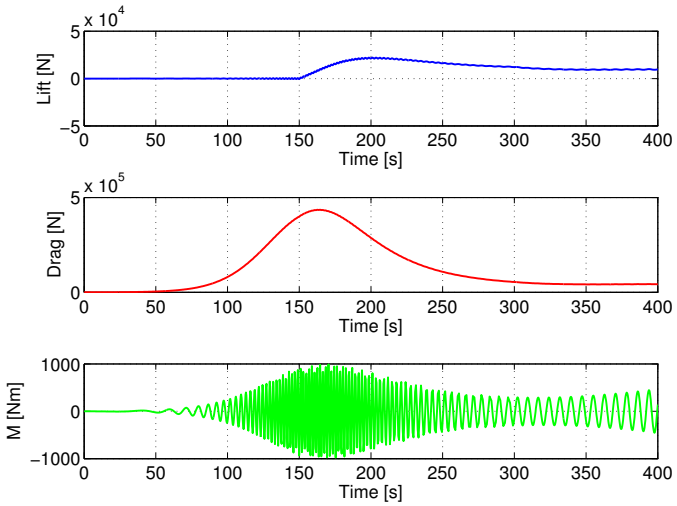

Figure 8-16: Simulation results for the lift, the drag and the pitch moment to test simulation input stated above.

Verification with a Step Input Signal

To verify the model further, a comparison with the linearized model is set up to match the results from the Open-loop Testing with the Linearized Model section. A simulation for $5s$ is made with a step input of $\delta cg_{z,aft} = -0.4m$. The initial condition are taken from the EDL reference trajectory, as described in Section 5-5, at an altitude of 40 km. Figure 8-17 shows the response of the angle of attack of the linearized model compared to the response from the Simulink® system; the two models show comparable fluctuations. For the first $0.5s$, the linearized response matches the non-linearized response well. After $0.5s$, the non-linearized model deviates from the linear path and settles for an oscillation with a smaller period and amplitude than the linearized counterpart. A similar pattern is observed in the flight path angle response in Figure 8-18, where it can also be seen that the non-linear response increases at a higher rate. Figure 8-19, the velocity response, shows the same oscillatory behavior as α and γ. However, in the non-linear model, the velocity decreases much faster than the linearized response.

From this comparison it is concluded that the oscillatory behavior from the non-linear model in

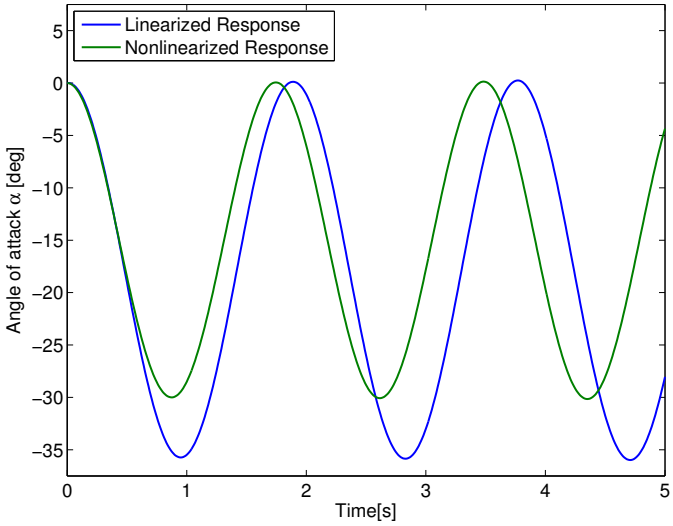

Figure 8-17: α response for the linear and non-linear model $\delta cg_{z,aft} = -0.4m$ at $h = 40km$

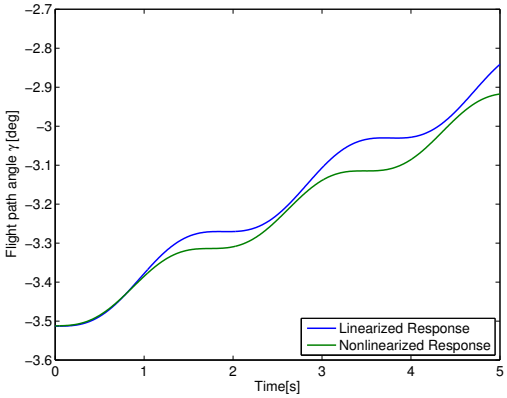

Figure 8-18: γ response for the linear and non-linear model $\delta cg_{z,aft} = -0.4m$ at $h = 40km$

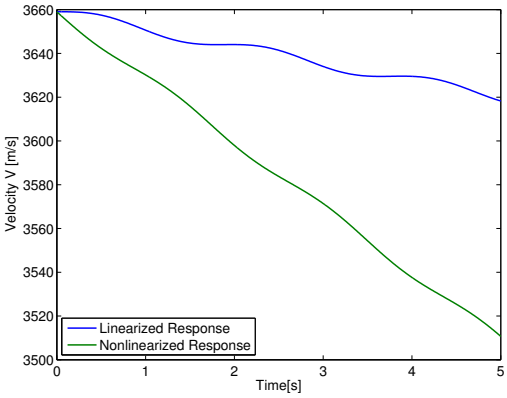

Figure 8-19: V response for the linear and non-linear model $\delta cg_{z,aft} = -0.4m$ at $h = 40km$m

the first verification method is not an error in the implementation of the dynamic system, as the linearized model features similar oscillations. The differences present between V, γ and α step input is explained in the following:

- The changing atmospheric conditions are not taken into account for the linear model. Whereas the density increases for the dynamic model, the conditions stay the same for the linearized system.
- The linear plots represent only deviations from the initial condition, but fails to represent trajectory effects. The faster decrease in speed of the dynamic model in Figure 8-19 is due to the simulated deceleration of the spacecraft within the atmosphere.

Through these two test simulations, the dynamic model output was judged based on expected behavior and the output of the linearized system. Based upon the results presented, the dynamic model is considered verified.

8-6-3 Validation

The model's ballistic trajectory presented in Figure 8-14 was compared to the trajectories determined from the predictor model in Chapter 5, Atmospheric Trajectory Design. The two trajectories display very similar characteristics, meaning that Simulink model manages to replicate the result of another model in this report that was validated. The Simulink model is thus indirectly validated.

8-6-4 Implementation of the γ-controller

Figure 8-20 shows a screenshot of the γ-controller in the final set-up. The θ-controller was tuned before the γ-controller. The changes in θ occur relatively quickly. The minimum gain was found by shifting the poles of the eigenvalues of the linear model along the root locus. It was determined that the θ-controller had a K_p of 10 and a K_d of 30. Through trial and error, it was also found that θ was tracked better when applying a K_i of 0.3. The γ has a slower response time than θ, and due to the non-linearities involved the linear system could not be used, and the gains were experimentally obtained. As $cg_{z,aft}$ is defined positive downwards, the controller should have an inverse logic: when a increase in flight path angle is needed, the space craft should provide positive lift, and therefore a negative center of gravity offset. The result of this inverse logic is that gains are negative. K_p was found to be -13, K_d to be -4 and K_i to be -0.7.

8-6-5 Implementation of the V-controller

Figure 8-21 shows a screenshot of the V-controller in Simulink. This controller also uses the same θ-controller as the γ-controller, applying the same gains. The same inverse logic (i.e. negative gains) applied to γ-controller is valid, but the gains are smaller since the error is measured in meters, as opposed to degrees. K_p was found to be -0.05 and K_i to be -0.01. There is no differential control with respect to V; it was seen that,as soon as a differential control was applied, the speed was not correctly tracked. Table 8-7 details the gains used during both aerocapture and EDL.

Table 8-7: Summary of all gains as used for the $\theta-$, $\gamma-$ and the $V-$ controllers

Type	Gain for aerocapture	Gain for EDL
θ-controller		
K_p	10	10
K_d	30	30
K_i	0.3	0.3
γ-controller		
K_p	-13	-13
K_d	-4	-4
K_i	-0.7	-0.7
V-controller		
K_p	-0.05	-0.05
K_i	-0.01	-0.01

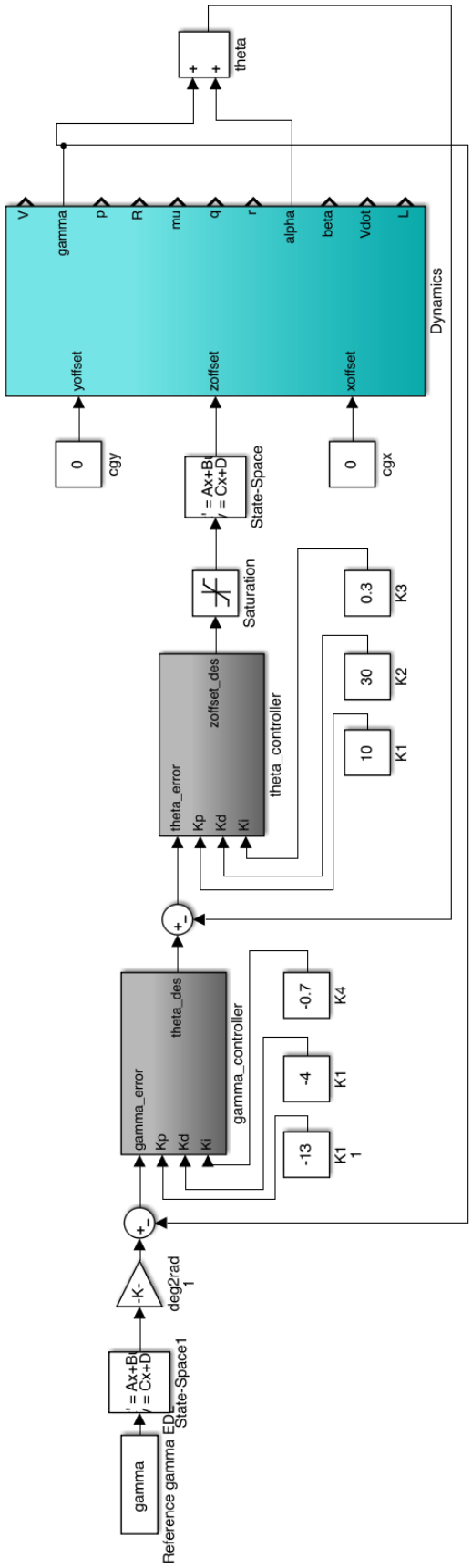

Figure 8-20: The γ-controller as depicted in Simulink

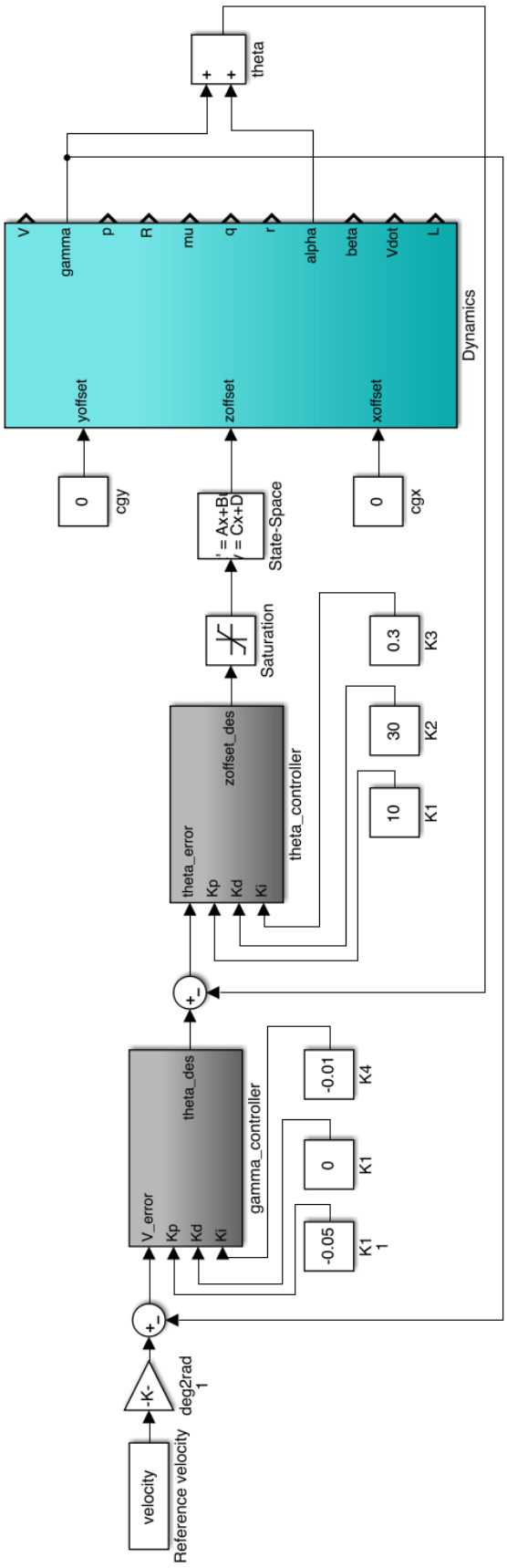

Figure 8-21: The V-controller implemented in Simulink

8-7 Simulating Aerocapture and EDL

Once the dynamic system is verified and the controller is implemented and tuned, a full simulation of a longitudinal controlled aerocapture and EDL is performed. A performance simulation is done for two reasons: to provide requirements for the structural design of the actuator and to asses the feasibility of the center of gravity shift as a control concept. The actuator designed in Chapter 7, Structural Design, has to provide the necessary $\delta c.g._{z,aft}$ and the velocity and acceleration needed to achieve the displacement within the required time. Four controller simulations were set-up and are discussed in this section:

- Aerocapture with the γ-controller.
- Aerocaputre with the V-controller.
- EDL with the γ-controller.
- EDL with the V-controller.

Table 8-8 shows the initial conditions used for aerocapture and EDL simulations; only the entry velocity and the flight path angle differ.

For the sake of brevity, this section only details two most important parameters per simulation. The tracking is be assessed with a plot of the desired γ or V against the actual value and an accompanying error plot; the actuator position and acceleration are also shown. All other parameters, such as angle of attack, altitude or g-loads are not be presented.

Table 8-8: Initial conditions for aerocapture and EDL simulations

	V	γ	R	p	q	r	α	β	μ
Aerocapture	7000 [m/s]	-11.5 [deg]	3519500 [m]	0	0	0	-19 [deg]	0	0
EDL	4715 [m/s]	-11.75 [deg]	3519500 [m]	0	0	0	-19 [deg]	0	0

8-7-1 Input Reference Trajectories

Reference trajectories obtained as explained in Chapter 5 are used; note that the trajectories used in this chapter are not necessarily the final trajectories outlined in those sections. In Figure 8-22, the input trajectories are displayed in combination with their respective derivatives. All reference trajectories are smooth curves, except from the $EDL-\gamma$ reference trajectory, which features two kinks (at $t = 130s$ and $t = 250s$). These kinks are present because the reference trajectory is designed with step changes in lift; these kinks in γ cause the controller to oscillate. The steps are smoothened by including a first order filter in the system. This filter is implemented before the error in flight path angle is computed, as in Figure 8-20.

8-7-2 Results for Aerocapture with γ-controller

In Figure 8-23 it can be seen that the γ-controller tracks the desired γ with a maximum error of $-0.18deg$. This is considered a sufficient accuracy. The actuator does not show any oscillations, apart from the first 20 seconds. Figure 8-24 shows the actuator performance. The offset fluctuates between -0.6 and +0.1 m. The acceleration seems to stay between +0.1 and -0.1, with a spike in the first 10 seconds. This spike is by caused by inaccuracies in the beginning of Figure 8-23.

8-7-3 Results for Aerocapture with V-controller

Figure 8-25 shows the results of the performance of the V-controller. It performs equally well as the γ-controller. The error is at maximum 1.5 m/s, as can be seen from the second subplot in Figure 8-25. The actuator performance graph, in Figure 8-26, shows however rapid oscillations in $\delta c.g._{z,aft}$. These oscillations translate in larger oscillations in the actuator velocity graph.

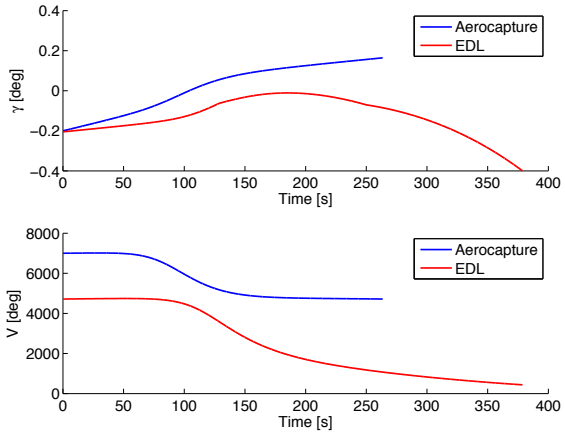

Figure 8-22: Input for the V-controller and the γ-controller.

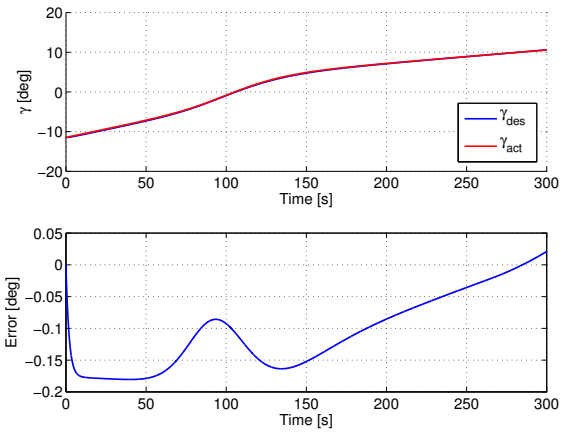

Figure 8-23: Aerocapture tracking performance for the γ-controller

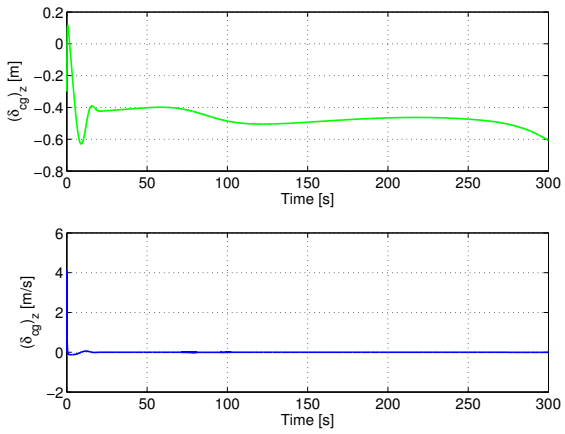

Figure 8-24: Actuator position and speed for the γ-controller for aerocapture

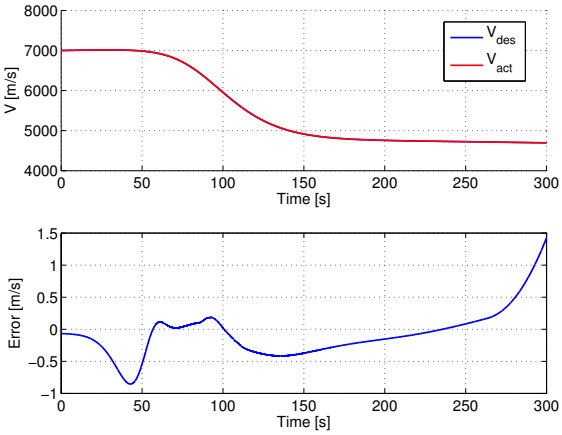

Figure 8-25: Aerocapture tracking performance for the V-controller.

Results for EDL with γ-controller

In Figure 8-27, the tracking performance for the EDL mission is displayed. The tracking is less accurate than for the aerocapture, this will be elaborated on in subsection 8-7-4. The maximum error in for this simulation is $0.5deg$, which is considered high. The accompanying actuator performance in Figure 8-28 hints as to why the tracking is less accurate: it can be seen that after the two jumps in the input signal at $t = 130$ and $t = 250$, oscillations are present in the actuator. This is discussed further in subsection 8-7-4.

Results for EDL with V-controller

A simulation for the EDL is made using a V-controller. The results are similar to the tracking performance of the aerocapture. The controller tracks the desired trajectory with a maximum error of $2m/s$. Unfortunately, the same oscillations present in Figure 8-26 show up in Figure 8-30. After $t = 120$ the oscillation occur in both the velocity and position of the actuator.

8-7-4 Discussion of Results

From the results it can be concluded that the controller is capable of tracking the flight path angle and velocity with sufficient accuracy. However, there are three significant issues that have to be

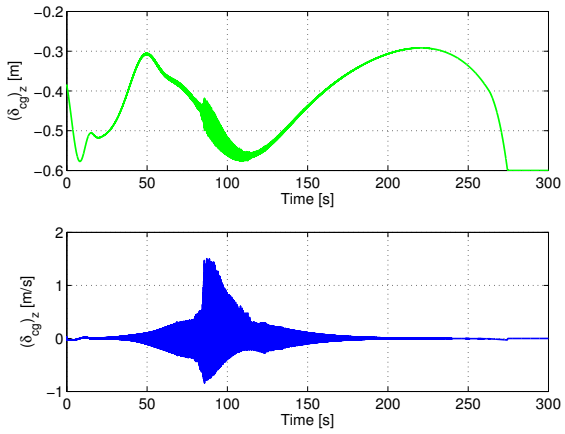

Figure 8-26: Actuator position and speed for the V-controller for aerocapture

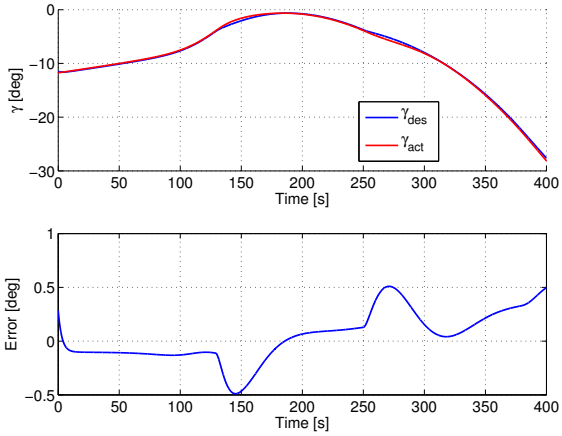

Figure 8-27: EDL tracking performance for the γ-controller

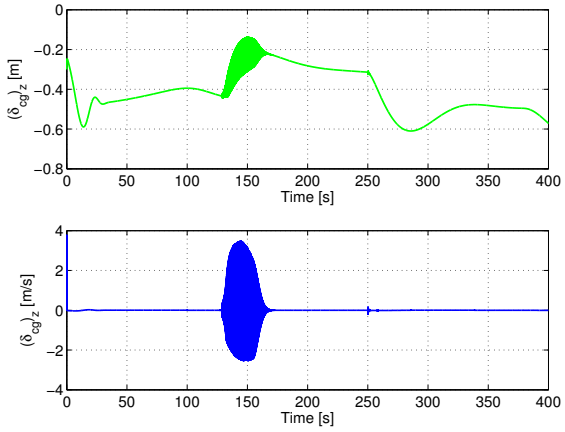

Figure 8-28: Actuator position and speed for the γ-controller for EDL

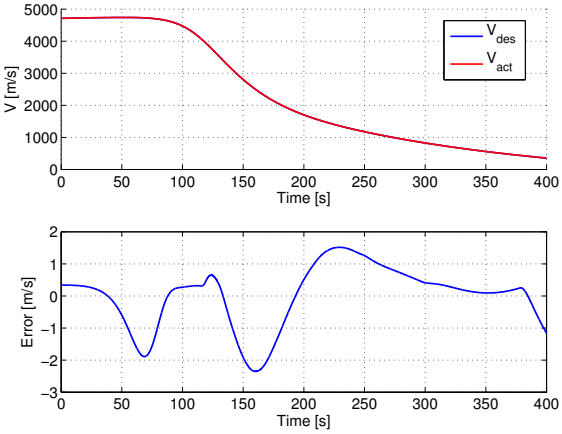

Figure 8-29: EDL tracking performance for the V-controller

solved before the controller design process can continue as proposed in Section 8-5.

- In all four simulations there are oscillations in the actuator deflection in the first 20 seconds. These oscillations are related to the θ-controller. Figure 8-31 shows the tracking of θ for the γ-controller on the EDL reference trajectory. The controller first overshoots, then undershoots, and finally stabilizes. At first glance it seems that the initial conditions are off, and therefore a small step input is given. However, careful analysis shows that the initial condition of θ for the desired trajectory and the actual trajectory match. Furthermore, the initial c.g. shift matches the initial trim angle off attack of $-19deg$. At this point there is no clear observable explanation as to why the θ-controller causes oscillates in the first 20 seconds. However, from the spike in the error at $t = 0s$ in Figure 8-31, it must be concluded that there must still be some offset in the initial conditions that is seen as a step input by the controller. Since the θ-controller is a PID, this error is most likely related to wrongly assigned initial values for the integration.
- Oscillations are present in the γ-controller and the V-controller for the EDL trajectory. Zooming in on Figure 8-28, it can be seen that the controller at $t = 130$ shows rapid oscillation with a frequency of about $5Hz$; there exist no actuator mechanism that can provide such oscillations. However, since the γ-controller does not show these kind of oscillations in the aerocapture sim-

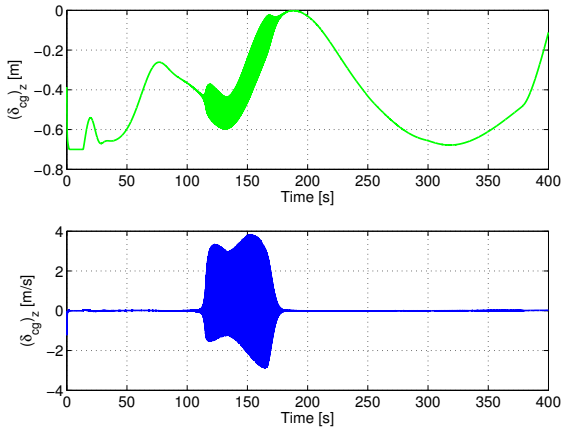

Figure 8-30: Actuator position and speed for the V-controller for EDL

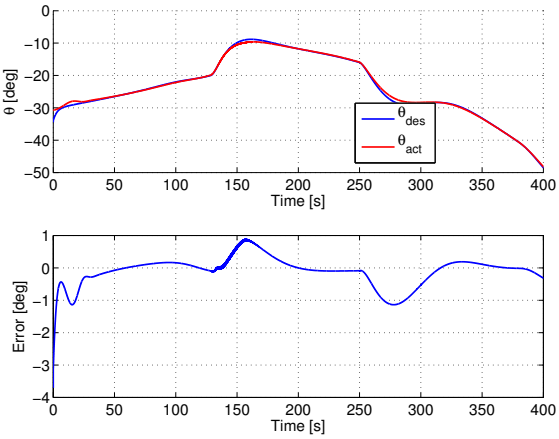

Figure 8-31: EDL θ tracking performance for the γ-controller

ulation, the cause is investigated in the input reference trajectory. Figure 8-32 shows the input γ and the corresponding derivative $\dot{\gamma}$. It can be seen that there are sudden changes in the slope of the flight path angle. The oscillations present are concluded to be caused by these sudden jumps in the derivative of the flight path angle $\dot{\gamma}$. The V-controller shows these oscillations at the exact same time. Therefore, both controller would perform better without any jumps in the input trajectory. Ideally the input trajectory should be smoothened to eliminated sudden changes in $\dot{\gamma}$. However, due to time constraints, it is not possible to do that in this analysis.

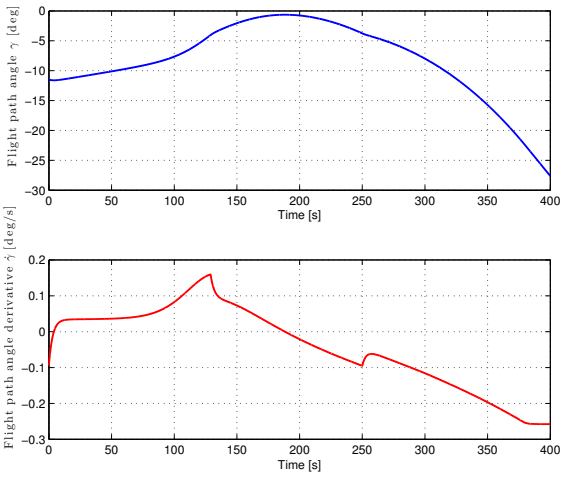

Figure 8-32: Reference EDL trajectory for the γ-controller.

- The V-controller shows oscillations in the aerocapture, larger than the oscillation discussed in the previous item. These oscillations are related to the input reference trajectory signal. It is possible that better PID tuning could improve the results. As the aerocapture trajectory is tracked well with the γ-controller, it may also be that the velocity is not an optimal parameter to control the system. Since oscillation build up gradually, indicated an unstable controller in $t = [0 - 100]s$, gain scheduling can be applied to minimize or even resolve this problem.

Besides these issues, three main limitations to the accuracy of the Simulink® model have been identified:

- **Aerodynamic Coefficients:** A limitation of the control simulation is that it is based on the aerodynamic model described in Chapter 4; the simulation is limited to the assumptions introduced thereafter. Furthermore, the simulation uses linear relationships for the aerodynamic coefficients and thereby introducing linearization errors.
- **Atmospheric Irregularities:** The simulation is run with the same atmospheric conditions as the reference trajectories. In reality the spacecraft will encounter other conditions and atmospheric irregularities and perturbations. The controller is not tested to track the reference trajectory for different conditions. In future investigations, a Monte Carlo analysis is recommended.
- **Controller Type:** The purpose of the tested controller is to show the feasibility controllability via a c.g. offset. Attention is paid to the behavior of the control system. Therefore, a linear system of PID controllers is used as opposed to more advanced methods. Sensor based controllers are available which is especially advantageous to non-linear systems.

8-8 Conclusion

Requirements for the structural analysis of the actuator can not directly be extracted from the actuator position and speed graphs. Assuming that the initial deviations in the actuator position and speed, together with the large oscillations can be avoided with a better control system, the requirements as stated in Table 8-9 were taken for the actuator system.

Table 8-9: Table of the defined requirements for the longitudinal c.g. actuator.

$\delta c.g._{z,aft,min}$	$\delta c.g._{z,aft,max}$	$\dot{\delta c.g.}_{z,aft,min}$	$\dot{\delta c.g.}_{z,aft,max}$
-0.7 [m]	0.2 [m]	-0.1 [m/s]	0.1 [m/s]

For the lateral actuator requirements are provided based upon the step input analysis from subsection 8-2-3. From Figure 8-9, a smaller center of gravity shift is needed in the Y_b axis than in the Z_b axis in order to achieve similar attitude rates. The requirements for the lateral controller are detailed in Table 8-10.

Table 8-10: Table of the defined requirements for the lateral c.g. actuator.

$\delta c.g._{y,aft,min}$	$\delta c.g._{y,aft,max}$	$\dot{\delta c.g.}_{y,aft,min}$	$\dot{\delta c.g.}_{y,aft,max}$
-0.1 [m]	0.1 [m]	-0.1 [m/s]	0.1 [m/s]

It is the view of the group that, although the simulation showed the problems described above, the center of gravity offset mechanism should still be considered a feasible control concept. The simulation showed that that the flight path angle and velocity could be tracked using a longitudinal controller. The problems indicated seem to be related to the fact that the controller is underdeveloped, as opposed to any there being a flaw in the concept.

Part III

Design Review

Chapter 9

Resource Allocation and Budget Breakdown

This chapter evaluates the mass and power required for the main subsystems. It is a continuation of the investigation performed for the baseline report [2]. First a general mass breakdown is presented, followed by more in-depth analyses of the four main components: the aeroshell, the thrusters, the control system and the payload.

9-1 Mass Budget

There are two requirements on spacecraft mass that have a large influence on the design. The first requirement limited the entry mass to $10,000kg$. The second requirement limited the mass of the deceleration system to 10% of entry mass.

An investigation into typical mass ranges for critical subsystems was performed. The results are listed in Table 9-1, based on values from [54] and [55]. The percentages do not add up to 100 % because these are ranges of mass percentages. However, in this approach an attempt is made determine the estimates of the main elements of the mission which add up to circa 100 %. Table 9-1 will be used to verify whether or not the values are within the ranges given in reference literature to check the overall consistency of the mass approximation.

Table 9-1: Literature-based mass budget

Element	Typical Mass Range
Payload	15-50% of M_{dry}
Aeroshell	10% of M_{mem}
Structural	15-25% of M_{dry}
Thermal	2-5% of M_{dry}
Power	32% of M_{mem}
GNC Handling	0.6 % of M_{mem}
Communications	1.3% of M_{mem}
Novelty margin	25%
Uncertainty margin	5%

Table 9-2: Summary of the most important resource allocations

Vehicle Element	Mass estimate [kg]
Aeroshell system	1250-1600
Thruster system	186
Control system:	
-*Structure*	200
-*Power*	47.5
Payload	8300-8000
Total	**10,000**

The maximum entry mass, M_{mem}, is the total mass including the dry mass and the propellant mass. The dry mass M_{dry} is defined as the mass of all spacecraft subsystems, including mass growth allowance [54]. The payload, structure and thermal subsystems of the spacecraft are allowed to have a maximum value of 50%, 25% and 5% of the dry mass, respectively. These values were established empirically. The maximum value for the mass of the hypersonic deceleration system is 10% of M_{mem}, given by the design constraint.

The mass estimate for the power subsystem is approximately 32% of M_{mem} of the spacecraft. This data is obtained with an assumption of a total mission duration of 730 days (2 years) and a crew size of 5 [55]. However, since the crew will likely consist of three people, the mass of the power subsystems will decrease, as less power is required for life support systems. Knowledge about the scalability of this system with respect to the number of crew members is not available, so the extent of mass savings is unknown. Determining the actual mass fraction of the power system is left to further research.

The electronics do not have a high mass, which is why this system only comprises 0.6% of M_{mem} [54].

Communications include typical X-band, S-band and Ku-band communications subsystems [54]. The mass of the communications subsystems is circa 1.3% of M_{mem}.

9-2 Subsystem Budget Breakdown

Aeroshell System A mass estimate of the aeroshell was established by adapting values found in the NASA EDL Systems Analysis Phase 2 Report [56]. The mass of an aerocapture and entry HIAD is $1059kg$, with a $14m$ diameter HIAD and an aerocapture into a $500km$ orbit. A correction based on engineering judgment resulted in an estimated mass of $1250kg$ for this mission. This correction was determined by scaling the design down to $13m$ diameter and accounting for higher peak heating and dynamic pressure. A similar approach was used on [57], which used the same HIAD concept but landed a payload that was larger. In this case, an estimated aeroshell mass of $1600kg$ was the result.

The mass range of the aeroshell is thus from $1250kg$ to $1600kg$. This can be attributed to the fact that the budget was created before any investigation into the mass of the inflatable structure and flexible TPS had been performed.

The accuracy of the mass range is limited. This is because both reports considered missions very different from the mission that is addressed in this project. The first estimate [56] was based on a total vehicle mass of just over $7000kg$, which was aerocaptured into a lower orbit with a larger aeroshell than considered for this project. This would impose significantly different requirements on the TPS and supporting structure. For the second report, [57], the aeroshell used as a reference was meant for an entry mass that is an order of magnitude larger than the entry mass considered herein. The resulting error could thus be much larger. In Section 6-7 the final mass of the TPS was conservatively estimated to be $1500kg$ and to determine the mass of the full aeroshell the inflatable mass system should be included. Using [56], the inflatable mass system is estimated to be $200kg$ and adding this to the estimated TPS mass results in a total aeroshell mass of $1700kg$. As explained in Section 6-7, the mass estimate for the TPS system is conservative, but it can be concluded that the required system for control and deceleration will have a mass fraction above 10% ($1000kg$), which therefore does not meet the mass requirement.

Thrusters - Orbit Raisers Traditional thrusters are required for three reasons. First, to augment the mass shifting control system with more fine-tuned control and possible prevent any transient effects. Second, to orient the spacecraft before the atmosphere is entered. And finally to provide a certain amount of ΔV to raise and lower the periapsis of the transfer orbit. A choice was made to use 16 thrusters, divided into four blocks, similar to the Apollo service module's RCS layout.

During its entry into the Martian atmosphere, MSL was expected to used approximately 14 kg of RCS fuel [58]. As the spacecraft is larger than the MSL, but uses RCS only as an augmentation to its primary control system, the fuel mass was taken as $15kg$ based on engineering judgment.

The requirement that was driving for the size of the thruster was the size of the periapsis lower maneuver. Based on two assumptions a total fuel mass of $138kg$ is required. First, $13m/s$ of ΔV had to be provided, as determined in Section 3-2. By stretching this maneuver over 10 minutes and using four aft-pointing thrusters, each thruster would have to provide $55N$ of thrust. It was found in [54] that typical thrusters that provide $55N$ have a mass of $0.5kg$ and a specific impulse of $220s$. Second, it was determined that there should be a total ΔV capacity of $30m/s$, from Section 3-2.

An estimation of the total mass of the thruster subsystem is $186kg$. That incorporates $153kg$ of fuel, $8kg$ for the thrusters, $15kg$ for tanks (based on Apollo tanks [59])and an estimated $10kg$ for fuel lines and valves.

Control System The control system can be divided into two parts. They are the control mechanism (the actual mechanical linkage and electrical motors that allow the aft body to be translated with respect to the centerline of the aeroshell), and the power system that provides enough electricity for the actuators.

Control Mechanism As is stated in Chapter 7, the mass of the mechanism following detailed optimization is predicted to be circa $037kg$. The current estimate of $370kg$ is extremely conservative and rough and should, with the appropriate tools, be brought down to much lower values. The expected optimized value should be closer to $200kg$ which remains the current most optimistic estimate. Thus, the control structure contributes 2% to M_{mem}.

Control Power The trajectory control analysis required the payload module to be translatable at a maximum speed of $0.1m/s$ which, in combination with the structural loads that have to be countered by the actuation, led to a required power for each electrical motor of $2.7kW$. Since the payload can be moved in two directions, in the worst-case scenario, at most $5.4kW$ may be required at one time. The duration of aerocapture and entry flight phases are 300 and 400 seconds respectively. If full power were required continuously, a total of $3.8MJ$ of energy would have to be provided.

During aerocapture and entry the power is to be supplied by batteries since the power required in this phase exceeds the power required in all other mission phases. Additionally, solar panels cannot be used in these phases, and a radioisotope thermal generator (RTG) able to provide peak power of $5.4kW$ would be unreasonably heavy. For comparison, the generator aboard the Curiosity rover, the most recent application of RTG in space, provides $120W$ of electricity and has a mass of $45kg$ [60].

Batteries are hence required, and preliminary sizing was performed using the Quallion QL075KA [61]. The required amount of these cells came from the maximum power that has to be delivered since maximum discharge current is limited. For supplying $5.4kW$, approximately $38kg$ of batteries would be required. $38kg$ of batteries would also hold more than $19MJ$ of energy, much is more than enough. If a margin of 25% is applied to account for wiring and additional batteries for a margin in deliverable power, the secondary power supply subsystem will have a mass of $47.5kg$.

Payload Everything behind the control actuation mechanism is considered as payload. The mission payload mass was constrained at $9000kg$ of the $10,000kg$ by the general requirements. However the estimated mass of the decelerator, control systems and orbit raising range between 17.3 % and 20.3 % of the maximum entry mass. This means that the remainder of the mass - everything housed in the aft body - now ranges between $7970kg$ and $8270kg$ at entry. This remaining mass includes the structural mass of the payload module, the scientific/human payload, the propulsion system and required propellant for retropropulsion in the final EDL stages.

Chapter 10

Operations and Logistics of Final Concept

The Operational and Logistic structure determines how information and hardware are transferred between design and operational segments, between ground control and the spacecraft in the course of the mission. This section is divided into two segments. The first will address the logistics of hardware. The second is focused on mission support infrastructure after launch.

10-0-1 Hardware Logistics

Hardware logistics is engaged in providing and shipping all required hardware to the locations where they are needed, when they are needed [54]. This applies to the assembly of the spacecraft, before launch. It is an operation, during which strict deadlines have to be set and adhered to to ensure that the launch date can be met. The aft body, c.g. offset mechanism and aeroshell (together with inflation system and the respective bus) will be built separately, then transported to a location were they can be assembled. That would be followed by placing the assembly into a launcher fairing, which in turn has to be placed on top of the launch vehicle. After each step, tests must be performed to ensure that everything was done correctly. This operation must be completed on time for launch, as the launch window must be met. Failure to do so will postpone the mission by 26 months, until the next time Earth and Mars have the same relative position.

Hardware logistics does not end at the pre-launch phase, however, given the mission at hand. The spacecraft as it is designed is likely to be a human precursor mission, since the total vehicle mass is $10,000kg$, which is estimated as being too low to carry all equipment in one mission. Most likely multiple spacecraft will be needed to bring humans to Mars, provide a life-sustaining habitat on Mars and ensure that there is a spacecraft (or architecture) ready to bring the astronauts home. Although the calculated launch mass of $271.000kg$ is a rough estimation, it confirms the multiple needed precursor missions.

10-0-2 Mission Support Infrastructure

During the mission, there will be continuous communication between Earth-based controllers and the spacecraft. Information transfer from spacecraft to ground control on the status of the payload, on-board systems and trajectory is necessarily an omnipresent requirement. In the event that the vehicle carries a crew, these communications include messages to earth. Based on the information received from the spacecraft, ground control can decide on a course of action. That action can range

from diagnosing and troubleshooting any system failure to executing course corrections. When the vehicle is physically isolated, i.e. during the transfer orbit to Mars, and communications with Earth are delayed, a degree of autonomy is required. That includes a power source and on-board decisions in situations where it is not possible to wait for an answer from Earth, such as the aerocapture and EDL phases.

An important task of the mission operations is also the determination of the trajectory of the spacecraft. This defines the total duration of the mission and the propulsion requirements. Optimizing the suitable orbits and trajectory will have a significant effect on design. Examples of parameters to consider are: crew health, hardware status (in particular radiation levels and the continuous monitoring of subsystems that could be affected by the environment of deep outer space), life support system health and required power levels, ΔV budget, etc.

Figure 10-1 shows the operational and logistic diagram for each phase of the mission.

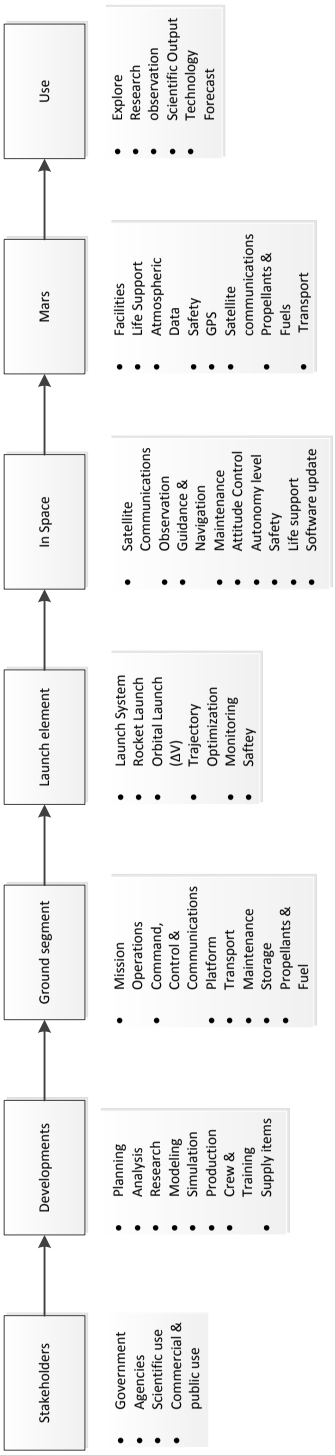

Figure 10-1: Operation and Logistic diagram for each phase of the mission

Chapter 11

Performance Analysis

11-1 Sustainability Analysis of Final Design

The original concept chosen at the end of the conceptual design phase (documented in the Midterm Report) featured advantages concerning sustainability that made it favorable compared to the other designs. The aft body offset mechanism was preferred concerning mass and fuel consumption. More information about the sustainability characteristics can be found in Section 2-2. This section evaluates the strengths and weaknesses of the final design concerning sustainability with a particular emphasis on the materials used and the power system.

Thermal Protection System The aeroshell is designed to be used in both aerocapture and EDL so its Thermal Protection System is designed to protect the aft body from the heat loads by insulating/radiating heat energy (see Chapter 6) - no ablative materials are used. Though it is expected that the aeroshell is reusable after aerocapture for EDL, this expectation should be further explored in the future. If the inflatable aeroshell is found to be unusable after aerocapture, a second aeroshell will have to be carried on-board. And though several mechanism could be re-used (e.g. control mechanism, inflation system, packaging), the mass of the vehicle would increase greatly. Furthermore, discarding the first aeroshell in orbit would contribute to space debris.

Actuation and Control Mechanism The actuation mechanism, described in Section 7-2 (Design Logic), is developed to minimize weight and minimize the power needed. The controller imposed a requirement on the speed and maximum lateral and longitudinal displacements of the center of gravity which can be found in Section 8-8. It is thus estimated that 4 motors, each with power of $2.7kW$ and weight of $20kg$ are needed to guide aerocapture and EDL. The motors are electrical and the system will require approximately $10kW$ of power. This result is considered sustainable concerning the design. The mechanism that is driven by the aforementioned electrical motors is, however, currently assumed to be made of $290kg$ of solid titanium which, in all likelihood is not the most sustainable design choice.

Safe-Life There are two popular philosophies of design: fail-safe and safe-life. In fail-safe, redundancies are used to ensure that another part of the design can take up the load in case of failure. This philosophy can be used when the exact life-time of the structure is unknown, and the need for safety drives the design in a more conservative direction. Safe-life follows an approach whereby the system is designed to not fail throughout its life-time. This approach is favorable to systems where the life-time is better known. This is the case for the system designed, and it would thus

be optimal to follow such a strategy. Aerocapture and EDL force the aeroshell mechanism to be active for a specific amount of time, which is known prior to the mission. Another reason to avoid using the fail-safe approach in this mission is the need to decrease mass, and redundancies come at the cost of higher mass. Reducing mass by employing the safe-life design philosophy improves the sustainability aspects of the spacecraft.

11-2 Sensitivity Analysis of the Final Design

Sensitivity analysis indicates how the system reacts to changes in system requirements, and tests how robust the system is to those changes. Sensitivity analysis is performed per discipline and the outcome of these multiple analyses is summarized in the section that follows. This is done by identifying the key drivers for each discipline and how changes of those affect the overall system.

Astrodynamic Trajectories The sizing of interplanetary travel found that the following design parameters have the greatest influence on the system: flexibility of mission duration, the time spent in outer space and maximum aerocapture entrance speed. Since the efficiency of the interplanetary trajectories depends on the relative position of the two planets, constraints on the mission duration can result in a high fuel and efficiency penalty. Also, the more time the system has for its interplanetary travel to and from Mars, the lower the overall delta-V budget but, the higher the required radiation shielding. Longer transfer times require better protection for the human-rated payload from the hostile outer space environment. The maximum aerocapture entrance velocity determines how much of the interplanetary trajectory velocity the system has to lose using propulsive deceleration before entering with the specified maximum aerocapture entrance velocity. A higher entrance velocity will allow carrying less propellant.
The final target orbit is very sensitive to the accuracy of the aerocapture maneuver. The recommendation of the orbit was aiming for energy efficiency, however small inaccuracy of the exit conditions cause a steep increase in fuel needed to correct for any deviations from nominal conditions.

Aerodynamic Model For the calculation of the aerodynamic characteristics of the aeroshell two main drivers are identified: the surface area and the half-nose angle. Increasing the surface area has very little influence on the coefficients but will influence the overall resultant forces since the aerodynamic forces are functions of the surface area. The second key driver is the half cone angle - the more the aeroshell resembles a flat plate (larger half-nose angle) the higher the magnitude of the aerodynamic coefficients. At the same time the lift over drag ratio is slightly increasing with the given change in half cone angle.

Atmospheric Trajectories The aerocapture maneuver is highly sensitive to changes in the entry conditions, surface area and mass of the system. Because the limiting factor for the aerocapture maneuver is the performance of the TPS, the sensitivity analysis is expressed with respect to the maximum heat flux. An increase in mass, and/or a decrease in the overall surface area results in the deeper penetration of the atmosphere and exposes the system to higher heat flux. (A similar relationship is found when entering with a steeper entry or a higher velocity).
For the final descent the g-loads and target conditions are found to be the design drivers, so that changes in mass, surface and entrance conditions are analyzed with respect to these design drivers. Increasing the ballistic coefficient (higher mass, lower surface area) will result in a decrease of deceleration loads but the target conditions are impossible to meet without a major design change. Steeper entry or higher entrance velocity force the system to decelerate quicker, exposing it to higher deceleration loads.

Thermal Protection System The dimensions of the TPS are dependent on the maximum heat flux and the duration of the atmospheric maneuvers. A higher peak heat flux would affect the thickness of the outermost layer assuring proper protection while a longer duration of flight in the atmosphere would affect the insulator layer of the TPS responsible for keeping the ambient temperature for the actuation mechanism and payload below the operational maximum. The nose radius, which, when maximized, is a derivative of the half-nose angle and launcher fairing diameter, is found to be a system driver since an increase in the nose radius reduces the heat flux that the system is exposed to.

Control Mechanism Designing the mechanism for the control of the aerodynamic forces showed that the simplicity of the design shaped the final choice. If the complexity of the mechanism was to increase, this could result in a more mass-efficient design, at the expense of higher risks. The maximum acceleration determined the size and dimensions of the final rail system so that the material would not yield in operation. Higher deceleration loads required greater thicknesses along with greater safety margins to avoid any plastic deformation.

Vehicle Sizing The two main factors sizing the overall shape of the spacecraft were found to be: the diameter of the aeroshell and the half-nose angle. The spacecraft's stability is a function of the aeroshell diameter and the length of the aft body bus. Increasing the aeroshell allowed for a greater distance between the center of gravity of the entire vehicle and the tip of the aeroshell. The TPS analysis required the stagnation point to remain on the curved section of the aeroshell and he half-nose angle is the determining factor in this relationship since a larger half-nose angle will result in a lower maximum angle of attack. At the same time, however, this allows for a larger nose radius - beneficial for the TPS.

Guidance, Navigation and Control The main parameters that influence the performance of the Guidance, Navigation and Control design are: the aerodynamic coefficients, the actuator performance, the amount of mass that is shifted and the error in the initial conditions for the reference trajectory. First, the controller is sensitive to a change in aerodynamic coefficients. The greater the aerodynamic coefficient, the greater the aerodynamic forces, the better the controller will be able to track the desired trajectory. Second, the actuator performance influences the controller. If larger actuation velocity can be provided, the tracking of the trajectory will be more accurate. Third, the controller manipulates the displacement of the aeroshell with respect to the aft body (or vice versa), so the mass ratio between those two parts of the vehicle is identified as a design specification. If less mass is displaced with respect to the aeroshell, larger displacement of the center of gravity from the actuator will be required to compensate. Also, a total increase in mass will not be beneficial for the controllability of the vehicle. With a larger mass, the spacecraft will need a larger lift force to make it change direction. Finally, the system is very sensitive to errors in the initial conditions. From the simulation it was seen that an offset in the initial conditions has a large effect on the tracking performance. Therefore an accurate reference trajectory should be provided.

Conclusions The design process revealed how interrelated the disciplines are, and that changes in the main design parameters tend to influence a large number of subsystems. A larger surface area offers the advantages of larger aerodynamic forces that can be used by the controller to stay on track with the reference mission, and at same time assure that the EDL phase will reach its target condition. This, however, would require the control mechanism to be scaled up to meet the higher deceleration loads during reentry. On the other hand, changes in total entry mass were found to have the opposite effect, with higher mass resulting in worse controllability. This would also lower the peak deceleration loads and allow for a lighter actuation mechanism. Last but not least, increasing the half-nose angle would result in higher aerodynamic forces given constant surface area, at the expense of a lower maximum angle of attack.

11-3 Risk Analysis of Final Design

The greatest risks (and, where applicable, means of minimizing the associated probability and impact) within each discipline are identified and summarized in this section. The individual risks are numbered and displayed in a risk map in Figure 11-1.

Astrodynamic Trajectories The two major risks identified for interplanetary travel are: (1) insufficient protection from space environment, and (2) inaccurate Mars arrival conditions. The human-rated aft body has to be protected from the highly hostile space environment (namely the high radiation and the effects of weightlessness). To limit the risk of exposure the maximum time spent in outer space is limited to 210 days, with a final interplanetary travel time of 209 days. Regarding the inaccuracy of the transfer aerocapture modeling showed that high accuracy for aerocapture entry conditions is required. Therefore trajectories which induce high uncertainties (e.g. a fly-by) are avoided and a Type-1 transfer is chosen.
The greatest risk for the target/transfer orbit is (3) any inaccuracies in the aerocapture maneuver. The analysis showed that the target orbit is highly sensitive to changes in the aerocapture exit conditions, with large deviations having critical consequences for the mission. To minimize these risks, a safety margin of 25% for the velocities is included to correct for uncertainties, along with high emphasis on accurate tracking of the aerocapture maneuver. This risk also includes the chance of escaping from Mars, which was avoided by leaving the atmosphere significantly slower ($275 m/s$) than Mars' escape velocity.

Aerodynamic Model The simulation of trajectories, TPS and the controller rely on the aerodynamic analysis. Any uncertainties in this analysis have critical consequences for the reliability of the subsequent modeling and analyses. The first sizable risk that was identified is related to (4) the deficiency of the moment coefficient calculations due to limited knowledge of the effects at the edges of the aeroshell. This has an impact on the reliability of the controller which always targets trim conditions ($Moment = 0$). The second factor with critical consequences for the design is (5) the validity of the Modified Newtonian Method in the supersonic regime. Both the trajectories and the controller are to some degree functions of the aerodynamic coefficients. To decrease the development risk reference data for the Mars Pathfinder was used to scale the coefficients to more accurate values.

Atmospheric Trajectories The Martian atmosphere is highly variable, resulting in a high risk of (6) the spacecraft not being capable to produce the expected aerodynamic forces to follow the reference trajectory. Should the spacecraft leave the atmosphere after the aerocapture far from its target conditions, it won't be able to proceed into its target orbit which has fatal consequences for mission success. This risk is reduced by avoiding flying with the maximum angle of attack, so that the reference trajectories aim for a maximum angle of attack of 19^o compared to the 27.5^o physically possible. The second measure that was added to reduce the risk was the skip-out margin, i.e. the spacecraft is entering with the maximum buffer in entrance flight path angle - midway from the limits defined by the entrance corridor. The second risk that was identified is that (7) the thermodynamic loading might exceed TPS limits with critical consequences for the EDL phase.
In the EDL phase the variability of the atmosphere can cause higher than expected g-loads with (in extreme cases) an uncontrolled-skip out. Since the descent to Martian surface shares similar concerns with aerocapture with respect to the aerodynamic forces, the same measures are taken to limit the likelihood of the risks. A separate risk that was identified is (8) not meeting the target conditions in terms of velocity. This is tackled by increasing the aeroshell radius and optimizing the re-entry trajectory.

Thermal Protection System Three different risk are identified for the TPS: (9) heating at the edges of the aeroshell, (10) the degradation of the TPS during mission and (11) operational heat loading exceeding market-maximum specifications. The analysis of the TPS is focused on

obtaining the loads at the stagnation point, neglecting possible high-temperature effects caused by intersecting shockwaves at the edge of the aeroshell. Since the aeroshell, at this point in the design, is reused for the EDL any potential damage to it during aerocapture and/or time spent in the target/transfer orbit, have critical consequences for the EDL phase. The TPS currently operates at a higher heat flux than the maximum heat flux that can be resisted by materials available on the market which translates into high development risks for the TPS.

Actuation System The loads on the system are directly related to the accelerations acting on the system, such that (12) the structure must be able to withstand the encountered g-load peak. Minimization of this risk is achieved by designing for no single point failures and redundancies (four rails instead of two). (13) Failure of the actuation device would result in the uncontrollability of the system, so the motors that drive the c.g. offset mechanism are doubled-up and reliable/proven electrical motors are used to reduce the risk of failure or malfunction. Lastly, the effectiveness of the system as a whole was deemed to be a major risk. Said risk was addressed by choosing a design that has already been flight-tested (to some degree) limiting both development and operational risk.

Guidance, Navigation and Control The control logic of the design would ideally assure both a safe trajectory and accurately meeting the target conditions. The development of this control showed two major development risk. The first risk is associated with (14) the high-frequency fluctuations that have yet to be explained which point to a less-than-perfectly tuned controller. However, this could also be caused by a problem with Simulink integration, or could indicate that the design is not feasible. To achieve a more detailed picture the initial conditions were refined, the input signal was smoothed and the controller gains were optimized. The likelihood that this is caused by the infeasibility of the design is low, yet the consequences are fatal for the design. The second major development risk is (15) in assuming that the lateral and longitudinal controllers can be considered decoupled. This may oversimplify the design, neglecting critical coupling effects.

Risk Map The aforementioned risks are evaluated with respect to their likelihood/probability and consequence/impact using input from the lead designers of the team. Figure 11-1 and Figure 11-2 show the individual relationships between the risks' defining parameters, and indicates the areas that further research has to be concentrated on to reduce the total risk further to an acceptable failure level for the overall mission of 0.0005%.

This list gives a brief explanation of the placement of the individual risks on the risk map. The likelihood determines how high the chances of failure are, with a successfully proven product having low failure probability and one that would require further research to function having higher failure probability.

Risk 1 Long duration stays on the ISS have provided valuable insight into the protection of humans from the space environment.
Risk 2 Previous Mars missions have accomplished successful entry into Martian atmosphere.
Risk 3 Since aerocapture is a novel discipline, it has only been proven feasible in theory, yet with promising results.
Risk 4 The calculation of the moments rely on a simplified aerodynamic model lacking windtunnel test validations.
Risk 5 A windtunnel test of the HIAD can give insight into its aerodynamic properties and validate simulations.
Risk 6 Atmospheric fluctuations can influence the vehicle's lift generation capabilities, yet safety margins decrease the consequence.
Risk 7 Trajectory analysis showed that thermodynamic loading is critical and should not be exceeded.
Risk 8 The model predicted meeting target conditions, yet the model requires validation, increasing the likelihood of this risk.
Risk 9 Windtunnel tests would give further information on the heating at the edges of the aeroshell.

	Likelihood of Event				
Proof in Process				13,15	10, 14
Proven in Theory				6,7,8	3
Proven in Laboratory				11	
Proven in Windtunnel			9,4	5	
Proven on Fligh Test on Earth			1	12	
Proven in Full Mission				2	
		Consequence of Event			
		negligible	**marginal**	**critical**	**catastrophic**

Figure 11-1: Risk Map of the Final Design

Astro	1. Insufficient space enviroment protection
	2. Inaccurate Mars arrival conditions
	3. Inaccurate aerocapture exit conditions
Aero	4. Inaccurate moment coefficient calculations
	5. Model inaccuracy in supersonic regime
Tra	6. Deviation from expected aerodynamic forces
	7. Thermodynamic loading exceeds TPS limits
	8. Risk of insufficient deceleration during EDL
TPS	9. Risk of critical heating at aeroshell edges
	10. Permanent degradation of TPS from aerocapture
	11. Operational heat loading exceeds market maximum specs
STR	12. G-Loads exceed structural design limits
	13. Failure of actuation mechanism
GNC	14. Risk of untuned controller
	15. Risk of coupled lateral and longitudinal controller

Figure 11-2: Risk Table of the Final Design

Risk 10 Further research has to focus on the state of the TPS during and after aerocapture. The magnitude of the associated impact make this risk extremely potent and require that it be treated at the highest risk level.
Risk 11 Laboratory tests would reveal the heat loads that the TPS can withstand.
Risk 12 The IRVE-3 flight test showed that a rail system can withstand the deceleration loads.
Risk 13 The detailed design of the actuation system requires further research making it high-risk.
Risk 14 If the high frequency fluctuations result in infeasibility this has catastrophic consequences for the design.
Risk 15 The effects of decoupling the controller require further research making the likelihood of this event high.

11-4 Reliability, Availability, Maintainability and Safety Summary

This chapter will summarize and restate the design philosophy used throughout the design process with respect to reliability, availability, maintainability, and safety.

Reliability As defined in subsection 7-2-4, system reliability reflects the ability to perform and maintain functions in both routine and unexpected circumstances. The reliability of the spacecraft overall is largely dictated by the redundancies applied, the technological maturity of system components and the compatibility/integration of individual components in systems during production. At the current design stage the use of technologically mature systems/components is prioritized where possible. The redundancy in the design and whether a fail-safe or-safe life design philosophy was followed, largely determines the overall reliability. The spacecraft is designed for a precursor mission and though it would ultimately be desirable to design a vehicle that is both recyclable and reusable, a safe-life design approach was taken. This means that the spacecraft is designed to survive the design life with a chosen reserve. This also means that structural redundancy should not be exaggerated since the design loads occur for very short periods during launch, aerocapture and EDL. However, attention should be paid to eliminate and actively prohibit the occurrence of any single-point-failures in the design.

Availability Availability, defined in subsection 7-2-4, is the degree to which a system is ready and in a committable state at the start of the mission. Design availability is determined by the technology readiness level and technological maturity of the system, components and techniques used. Due to the nature of space design, systems may not be readily available and new technologies are often developed out of necessity. System components were chosen where available off-the-shelf technologies and techniques existed. This is reflected in the design of the TPS where SIRCA-15 was a principle material for recommendation. It was also reflected in the actuation system design where a double rail system similar to the one used on IRVE3 was chosen. Additionally, the controller was built around existing and available sensors (e.g IMU, MEADS, Rail Displacement Sensor from Section 8-3) to produce a feasible and producible controller design.

Maintainability Maintainability was defined in subsection 7-2-4 as the ease with which the system can be maintained. Due to the adoption of a safe-life design philosophy, the design of the spacecraft was aimed to survive only the design life with a chosen reserve. In summary, an outline of scheduled and non-scheduled maintenance activities was not performed since no maintenance is required prior to the retirement of the spacecraft. Furthermore, maintenance cannot be practically implemented once the spacecraft commences operations.

Safety The definition of safety-critical functions was provided in subsection 7-2-4. They are functions introduced into a system to prevent or stop the development of undesirable events, unacceptable risk of physical injury or damage, either directly or indirectly to systems or individuals. Safety-critical functions are needed for the harsh space environment during the interplanetary

flight phase and the high aerodynamic loading experienced in aerocapture and EDL maneuvers. For the spacecraft as a whole, the safety-critical functions that were considered while designing are presented in subsection 7-2-4 but are restated below for clarity:

- Physical systems to take into account vibrational loads that will be experienced and mitigate these to avoid the discomfort of passengers and structural damage or fatigue.
- The structural elements should be designed with materials with good thermal properties to avoid significant degradation of material properties with varying temperature. If heat were to penetrate the TPS more than expected it should not weaken the system's structure nor heat up the payload. This may require specialized coatings or thermal insulation.
- Physical systems should be implemented to take into account the effects of the space environment. Vacuum conditions may require certain out-gassing mitigation measures and low temperatures may cause certain metals to have unacceptably low fracture toughness.
- Radiation and ionization should be taken into account to avoid damage to both the aeroshell and payload (scientific equipment and crew). This may also require avoiding the use of certain composites that can be damaged by free radicals.
- Redundancy policy where extra structural elements are included that provide alternative load paths in case of unexpected loading or damage to existing structure.
- Safety factor where load-bearing capabilities are designed with a safety margin applied to the design loads (thermal, mechanical and vibration).
- Sensors should be included so that the health of the spacecraft can be monitored. (e.g. If the actuation system is damaged during aerocapture, crew can know not to immediately proceed with EDL). These may include strain gauges and displacement and temperature sensors.

Furthermore, many of the mission requirements impose restrictions for reasons of safety and reliability. These were taken into account since the spacecraft was specifically designed to meet these requirements. Compliance of the requirements is presented in Section 11-5.

11-5 Compliance Matrix

This section goes back to the key requirement analysis from Section 1-3. The key requirements are re-explored to determine how far the design has come in satisfying them. A full compliance matrix for all requirements is available in B, while Table 11-1 is a compliance matrix that shows the key requirements only. The compliance levels have been split into 4 , and a level of certainty is assigned to each requirement to indicate the level of confidence with which the compliance was assessed.

1. **Requirement met**. This status indicates that the current design meets this design specifications successfully. All requirements that are so marked also carry a Certainty level.
2. **Requirement met, but altered with customer's approval**. These requirements have been met by the design, but have been altered throughout the design process with customer's approval. These changes arose in the course of discussion and negotiation with the customer on the matter of the given requirement being unreachable or the possibility of satisfying other requirements with the alteration of the requirement in question. All requirements that are so marked also carry a Certainty level.
3. **Requirement's compliance not yet determined**. The compliance of the system to these requirements has not been explored in sufficient detail to be able to draw conclusions.
4. **Requirement not met**. These requirements have not been met by the current design.

Since the design is still in its preliminary phase, the statuses described above are also given a Certainty Level. The aim is to specify the level of certainty with which the requirement is met. The levels are given based on corresponding risk analysis and sensitivity analysis featured in this report. There are 3 levels:

1. **Certainty Level 1** indicates a high level of certainty that design conditions have been met.
2. **Certainty Level 2** indicates that there are doubts, generally regarding the accuracy with which the requirement was met.
3. **Certainty Level 3** indicates that the requirement appears to be met given the current analysis, but that further analysis should be performed.

11-6 Discussion on Compliance of Key Requirements

Table 11-1 lists the key requirements of the design with their scores for compliance and certainty. The scores are explained and further clarified in this subsection. All requirements except Req. 5 (not explored) and Req. 32 are satisfied with an acceptable Certainty Level; the final design is considered successful with respect to requirement analysis.

- **Req.1**: The EDL target box specified is met by the controller and the simulation provided. Though there are errors (i.e. fluctuations) in the result, these can be explained and the requirement is met. The uncertainty on whether it can be met accurately remains.
- **Req.2**: This requirement is met well with the current design. However, the system remains untested for any fluctuations in the atmosphere.
- **Req.3**: This requirement is key to the success of the aerocapture maneuver and the current model shows that it can be tracked with small errors. Once again, some uncertainty remains with regards to the accuracy.
- **Req.4**: This key requirement of the aerocapture mission seems to be met by the current design. However, the requirement requires a high level of accuracy that, though currently achievable, has not been fully investigated given possible atmospheric irregularities.
- **Req.5**: Though a lateral controller was designed the limited time and resources did not allow for a detailed exploration.
- **Req.6**: This requirement specifies the entry condition for the aerocapture maneuver, for which the interplanetary orbit is sized. The conditions are met in full by the current interplanetary trajectory design.
- **Req.19**: This requirement establishes a constraint on the design of the control system. This was fully met by the very nature of the design, which features an automated controller.
- **Req.27**: The current maximum acceleration experienced is $4.1g$. This requirement was met with sufficient margin to be given a high certainty level.
- **Req.28**: The current orbit around Mars is sized at 1 Sol, providing the spacecraft with 10 opportunities to perform EDL. This requirement is therefore met successfully.
- **Req.30**: The mass of the vehicle at entry will never exceed 10,000kg. This requirement is met with a high certainty.
- **Req.31**: The launcher fairing diameter was taken to be $5m$ when the system was sized. This allowed to maximize the lateral dimensions of the vehicle while conforming to the requirement. All other properties were sized according to this requirement. This requirement is thus fully met with a high certainty.
- **Req.32**: This requirement is not met with the current design. The mass of the HIAD and the control mechanism are estimated at 17.3% to 20.3% of the full entry mass (10,000kg). The main problem is with the TPS, which currently weighs 1505.6kg. The design follows a very conservative procedure to ensure that the heat load and heat flux are withstood by the vehicle.
- **Req.33**: This requirement was changed from the original value of $12m$, in agreement with the customer. The aeroshell diameter was increased so as to facilitate satisfying Req. 1. With the current trajectory, this requirement is met with a high certainty.
- **Req.41**: The highest heat flux expected is $68W/cm^2$ and the total heat load is $6214.2J/cm^2$ for aerocapture and $2401.8J/cm^2$ for EDL. The current design of the TPS predicts that this requirement is met. That the TPS is reusable after aerocapture, however, should be tested experimentally to increase the certainty level.

Table 11-1: Compliance matrix for key requirements

Req. Number	Type	Requirement	Date	Level	Key	Status	Certainty
1	AER	The spacecraft is to perform Entry, Descent and Landing to a target velocity of Mach 1.8 at 13 km	26/05/13	H	K	1	2
2	AER	The spacecraft is to guide the Entry, Descent and Landing along the determined downrange with a final accuracy of ±150m at 13km altitude	26/05/13	H	K	1	2
3	AER	The aerocapture must allow for dissipation of enough energy to leave the martian atmosphere with 4715 m/s	29/05/13	H	K	1	2
4	AER	The GNC must allow for an aerocapture exit flight path angle of 9.08 deg	18/06/13	H	K	1	2
5	AER	The spacecraft is to guide the Entry, Descent and Landing along the determined crossrange with a final accuracy of ±37.5m at 13km altitude	26/05/13	H	K	3	N/A
6	AER	The spacecraft is to enter the atmosphere at a speed of 7 km/s with a flight path angle of -11.05 deg	02/05/13	S	K	1	1
19	GNC	The system must employ an automated control system which can perform the landing on Mars autonomously	02/05/13	H	K	1	1
27	HUM	The accelerations on the spacecraft must not exceed 5.2g	26/05/13	H	K	2	1
28	HUM	The time between aerocapture and EDL must not exceed 10 days	03/06/13	S	K	1	1
30	STR	The mass of the vehicle must not exceed 10 000 kg	02/05/13	H	K	1	1
31	STR	The diameter of the fairing must not exceed 5 m	02/05/13	H	K	1	1
32	STR	The mass of the hypersonic atmospheric assisted decelerator must not exceed 10% of the vehicle's entry mass	02/05/13	H	K	4	N/A
33	STR	The diameter of the aeroshell must not exceed 13 m	02/05/13	S	K	2	1
41	TPS	The TPS system of the aeroshell must be able to withstand the heat flux during aerocapture and EDL	29/05/13	H	K	1	2

	Type	Status	Certainty
Legend	GE = General HUM = Human DEV = Development Requirements AER = Aerodynamics AST = Astrodynamics GNC = Guidance, Navigation & Controll TPS = Termal Protection System	1 = Requirement met 2 = Requirement met, but altererd with customer's agreement 3 = Requirement's compliance not yet determined 4 = Requirement not met	1 = High certainty 2 = Low certainty regarding accuracy 3 = Overall low certainty
	Level	**Key**	
	H = Hard Requirement S = Soft Requirement	K=Key requirement	

Part IV

Future Development

Chapter 12

Future Outlook

This chapter describes the future outlook, it starts with the design and development logic. Thereafter a development and a production cost estimation is made. Last a market analysis is performed to identify potential markets.

12-1 Design & Development Logic

As early as in the beginning of the past century proposals have been made for missions to put humans on Mars. To develop the current technologies to the level where they would enable the safe delivery of humans to the Martian surface, many steps need to be taken. This chapter discusses these steps, where the distant future is shown in Section 12-1, Design Steps, and a full description of the plan for the foreseeable future that can be implemented to improve the design will be given in Section 12-1, Project Future Outlook.

Design Steps

The detailed development phase follows the preliminary design review. The first main milestone is to perform successful guided aerocapture and EDL at Earth to validate the detailed design. The general process of the detailed design up to this test is split into eight phases which are shown in Figure 12-1. As can been seen in Figure 12-1, every phase has a feedback loop going back to the previous phase. Information obtained in a later phase can lead to more accurate design decisions in previous phases, also new phases can start before a previous phase is completely finished. Dates of milestones are an estimation, and many factors influence the time required for completion of the determinedphases, most importantly the amount of resources dedicated to the project.

The first step of the detailed design will be to apply system engineering to plan the remainder of the project in much greater detail. The mission plan will specify which resources will be available, and the time span of the design, build phases and the mission itself. Though the test flight will be performed in the Earth atmosphere, another important detail that will be specified in this planning phase is the scientific mission or other relevant objective that will be carried out on Mars. This will drive certain requirements for the aerocapture and EDL design phases, producing exact coordinates of the landing site and will allow the determination of the payload's characteristics. The first phase is planned to start in the third quarter of 2013, right after the DSE has ended.

Taking the (intermediary) results of the first phase into account, the second phase can kick off in the fourth quarter of 2013. this phase includes the detailed design of the interplanetary trajectory.

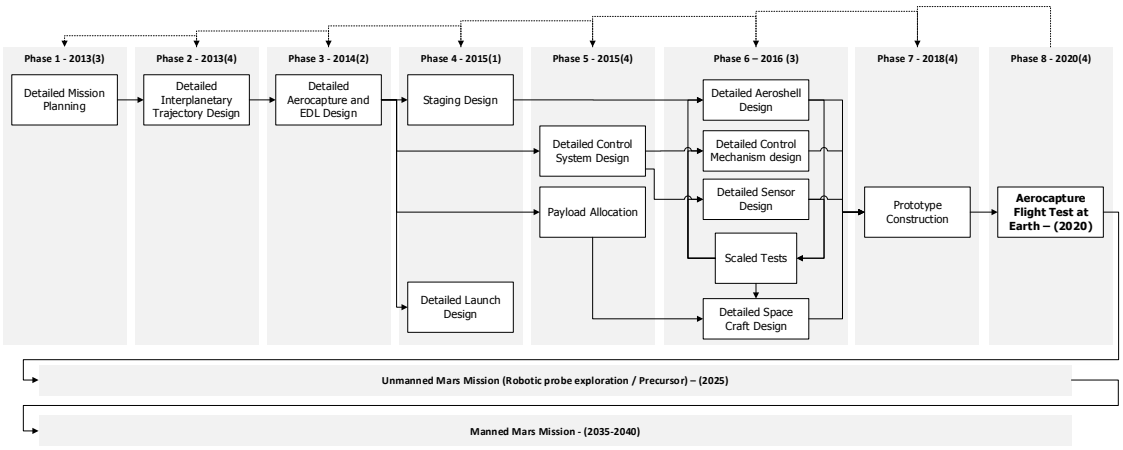

Figure 12-1: Future Outlook of the Global Development

It is expected that the first two phases can be completed quickly as these phases do not require any new knowledge or technology to be developed.
In phase three the design of phase one and two will be used to define the final aerocapture and EDL trajectories. Phase three is planned to start at the second quarter of 2014. Possible additional requirements for the ΔV budget can be established in this phase with respect to maneuvers in the target orbit. After that, both the staging and the launch can be worked out in detail in phase four, this is expected to start in the first quarter of 2015.

Phase five carries on with the spacecraft's detailed design by designing the control system and by distributing/fixing the payload in the vehicle. Allocating payload includes selecting what will be on board to fulfill the mission, as well as how much mass is reserved for each component and how the components will be packed. This process will start in the fourth quarter of 2015.

The previous five phases are required to determine the final design of the spacecraft which begins in phase six. This phase is the critical part of the design procedure. It designs the aeroshell in detail, taking aerodynamics, load-bearing and the thermal protection system into account. Phase six, starting in the second half of 2016, also yields a detailed design of the control system - the sensors that track the attitude and position of the spacecraft, the c.g. offset mechanism and the logic of the GNC computer. To reduce the risks of the Mars mission a scaled re-entry on Earth can be used to test the control system of the spacecraft, for which the previous IRVE missions can be used as a starting point for the test phase. Furthermore, NASA has a flight planned with the HEART concept test to return 5000 kg in 2016 [62]. It is likely that multiple scaled tests are required to validate the designs and to get more insight into the behavior of the aeroshell and the control system.
Successful tests will raise the technology readiness level (TRL) to a flight-proven design for the HIAD for EDL. At this moment, late 2018, a prototype of a full-scale spacecraft can be built. This prototype will be used in the last phase - phase eight - to perform in-flight validation of the control system effectiveness by simulating an aerocapture mission in the Earth atmosphere. Building a working prototype, performing the test flight and analyzing data from the test flight is a process that can very well take several years to complete. This to-scale test phase can incorporate multiple tests on Earth to better understand the loads that the aeroshell and relevant mechanisms need to withstand. It is expected that this phase will be completed before 2020.
If these tests are successful the HIAD can be used in the Martian atmosphere. Since the behavior of HIAD with respect to the Martian atmosphere is not fully known the first mission will likely be in combination with a robotic probe exploration or a precursor mission with a soft landing. The multiple needed precursor missions give a good opportunity to optimize the design and to gather more information about the Martian atmosphere. After the first successful precursor missions the

design for a human mission will start. It is expected that the first Martian aerocapture will be performed circa 2025.
After multiple proven Martian and Earth aerocapture missions, the TRL of the design should be high enough to get the spacecraft human-certified. A human mission will be designed further, it is expected that the first human attempt will be made between 2035 and 2040.

Project Future Outlook

As explained in previous chapters, assumptions have been used in the course of the design of the spacecraft. These assumptions result in uncertainties in performance and these uncertainties needs to be eliminated in the detailed design phase. A more detailed design and more comprehensive models will result in higher reliability and therefore higher success rate of the mission. In this section, a proposal for a "phase two study," with a similar group and time span (ten students and ten weeks), will be made.

Main Mission The main mission design includes the required steps to be taken before the spacecraft begins the aerocapture maneuver. This includes the logistics, communications, launch, and orbital travel. For this report, the most important part was the orbital trajectory design because the orbital trajectory was required to determine the feasibility of a human mission to Mars and get a feeling for the constraints. For the second phase the orbital trajectory could be designed with more accuracy by taking into account the eccentricity and inclination of the planet orbits. Other than that, the launcher could be sized and the effect of the vibration loads could be analyzed. During the inter- planetary travel, the influences of third bodies were neglected.
Another part of the main mission that would be interesting to investigate is the launch from Mars and the complete design of the return mission. This can be done by using the Apollo programs as reference [63]. For the Apollo mission NASA considered three possible mission configurations. The first configuration was a direct launch from Earth to Moon, a direct landing and a direct return from the Moon's surface with the same spacecraft. As a second option NASA considered the launch of two separate modules which would rendezvous in low earth orbit and, once docked, the spacecraft would travel to the Moon, and have a direct landing and direct take-off launch from the moon. The last option would be one where the spacecraft would be launched from Earth to a lunar orbit. A smaller spacecraft would then be used to descend to the surface of the Moon and return to the orbiting spacecraft. Similar options can be possible for the mission to Mars with, even, combinations of the trajectories considered for the Apollo program. For a phase two study these trajectories can be analyzed and it will result in a Delta-V that can be used to size the mission in more detail.

Aeroshell For the aeroshell two important aspects have been analyzed, the aerodynamic properties and the TPS. Because of the time constrains a model was made for the hyper sonic regime of the mission and scaled accordingly for the supersonic regime. As explained in 4-5 this resulted in some inaccuracies below Mach 5. For a more detailed study, a separate model should be made for the lower Mach numbers. To determine more accurate moment coefficients, an advances CFD model should be used. These improvements will result in a more accurate trajectory and a more accurate control system. The forces on the control mechanism will also be closer to reality with much more accurate body forces and moments to go on.
The TPS sizing can be done more extensively in the second phase by analyzing the flow between the shock wave and the TPS. Beside that, making a more detailed model for the relation of the temperature in front of the TPS and directly behind the TPS will help designing the layer thickness and weight of the TPS. Both the TPS system, and the aerodynamic model will benefit from a model that takes into account the effects of the flow at the edge of the aeroshell. Section 4-2 mentions the uncertainties that arise for the aerodynamic forces and moments and Section 6-7 notes how the thickness of the TPS at the edge of the aeroshell will (or should) increase as a result of higher heating due to shockwave interaction.

Structure The structural characteristics of the vehicle are perhaps the least developed at the present moment. Because there is little to no information regarding the payload make-up the mass distribution and, consequently, center of gravity are not accurately determined. Sizing the TPS, aeroshell, actuation system, and the spacecraft bus in more detail will give a more accurate center of gravity. This will result in more accurate moment coefficients and aerodynamic forces, and therefore result in a control system that is more accurate. For the current design of the actuating system only the forces in the EDL phase and the Aerocapture phase have been analyzed, but vibration load analysis is almost nonexistent. The highest vibration loads that the vehicle is expected to encounter in its lifetime are the vibration loads at launch. Incorporating these into the design of the structural elements of the vehicle will result in a more detailed design.

EDL & Aerocapture For the EDL and Aerocapture maneuvers Mars was assumed to be non-rotating. Relaxing this assumptio would make the reference trajectory more accurate. As explained in Section 5-1 the Martian atmospheric conditions fluctuate heavily between years and seasons. As explained in the same section, the atmospheric conditions are assumed to be constant, and these have been compared to other Mars missions. But for a second study the influence of arriving in different years and seasons will be interesting (and challenging) to model and incorporate.

Control The control system design for this report was meant to prove that the current design option is a feasible concept to guide the inflatable aeroshell during the EDL and Aerocapture phase. In a future study it would be beneficial to look into the optimization of the control system. Thic can be accomplished by implementing a trajectory predictor that will calculate the best trajectory after a deviation from the reverence trajectory in the control system. The control system architecture currently in place allows the spacecraft to be controlled in both lateral and longitudinal directions. The second phase could analyze the influence of actively controlling the bank and sideslip angles on accuracy in 3D trajectory tracking. The current control systems could also be modified and used to simulate the trajectories taking into account the fluctuations in the Martian atmosphere. Finally, a Monte Carlo simulation can be run to accurately determine the probability of meeting the target requirements of altitude, velocity, and physical location relative to the Martian surface.

12-2 Cost and Market Analysis

In this section a cost estimate is performed to estimate development and production costs of the inflatable aeroshell. Subsection 12-2 performs a market analysis for the inflatable aeroshell to establish potential market niches.

Production Cost Estimation and Break-down Structure of Development Cost

A cost break-down structure is an extremely useful tool to analyze future costs. Hundal (1997) states: "*The contributions to the cost of a product can be estimated in a variety of ways. These breakdowns are expressed in the forms of cost structures*" [64]. Thus the future development stage can be broken down into cost structures. In the current case, the cost structure consists of the development activities that need to be performed between the end of the DSE and the first operation mission. These cost activities are roughly described in Section 12-1 and are further detailed in Figure 12-2. Figure 12-2 is an AND diagram which identifies five main cost elements; Main Mission, Entry Mission, Aeroshell, Control and Structure. The Main Mission cost is the cost required for the development of the mission scenario and technology required for interplanetary flight from Earth to Mars, prior to entry. The Entry Mission consists of the cost required for further development of the trajectory analyses and athmospheric research for further precision. The aeroshell cost is the cost for developing the aeroshell's charastristics as listed in the diagram.

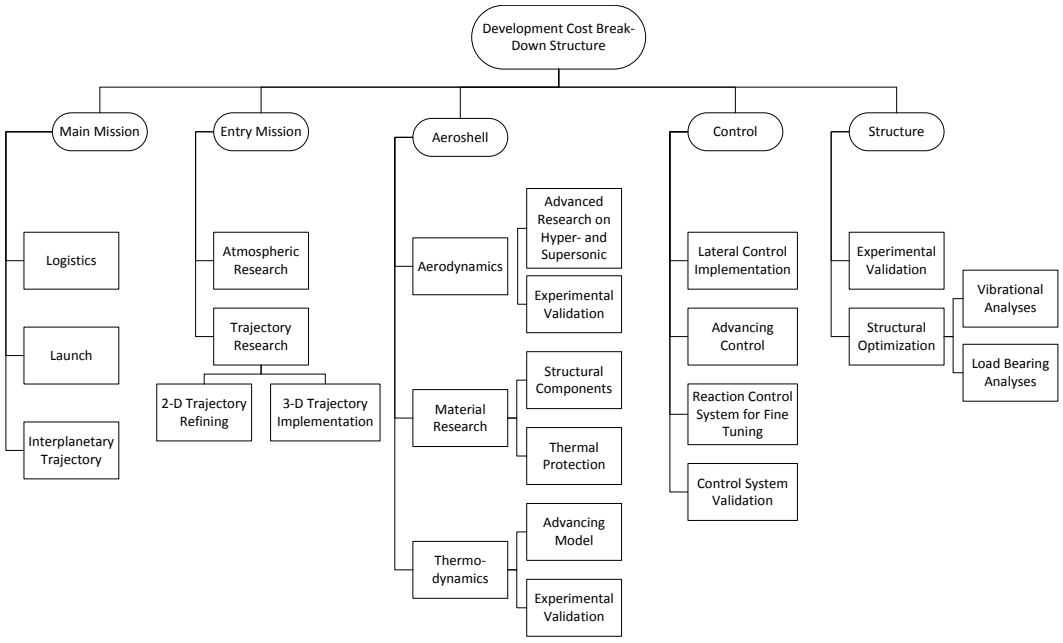

Figure 12-2: Cost break-down structure of the post-DSE developmental phase

For the production cost estimation, empirical data is used to estimate the first unit cost. The total mass of the design (aeroshell, control system and thrusters) ranges between *1730kg* and *2030kg*, calculated in Chapter 9. The dry mass is that amount minus the propellant for the thrusters, the dry mass ranges than between *1573kg* and *1873kg*. Empirical data relates the dry mass of crewed space systems to the first unit production cost, Figure 3-17 from Koelle's Handbook of Cost Engineering [65] shows that the estimated production cost ranges between 260 and 290 Man-Year. In the year 2000; a Man-Year equaled $200.000 USD. This was corrected for inflation to 2012 US Dollars (USD). From this the first unit production cost estimation ranges between 70 and 79 million USD and total spacecraft development cost estimated to be 4.6 to 4.9 billion USD. A NASA study into the cost of a manned mission to Mars estimated the development cost of the entire spacecraft to be 10.2 billion USD [66]. As will be discussed in Section 12-2, applications to transport cargo down from the ISS are considered for the aeroshell. Applying the inflatable aeroshell to the Cygnus spacecraft is estimated to have a first unit production cost of 43 million USD, also determined with methods from [65].

There is quite some uncertainty associated with this method. The reference spacecraft of [65] all flew close to Earth. Also, the novel technology to be used in the spacecraft designed in the DSE project increases the uncertainty in cost prediction as no similar spacecraft has ever been built. This is emphasized by the high difference between the development cost, namely $4.6 to $10.2 billion USD.

Although the first unit production cost are estimated to be high with the applied method, it is expected that the production cost of multiple aeroshell will be lower. This is invigorated by the production cost of IRVE-3, which was about 0.5 million USD [67]. Thereby is it expected that

Table 12-1: Market potential for different targets and mission types

Planet	Type	Market Potential
Mars	Robotic probe exploration	Small
	Human exploration - Precursor	Medium
	Human exploration - Manned	Medium
	Technology development & risk reduction for human Mars missions.	Medium
Other Planets	Robotic probe exploration	Small
	Human exploration - Precursor	Small
	Human exploration - Manned	Small
Earth	Robotic/Crew return	Medium-Large
	Garbage return	Medium-Large
	Booster/Launcher return	Medium-Large

the inflatable aeroshell reduces the overall costs of a mission due to the higher possible payload fraction. Therefore the HIAD could be attractive to third parties, in the next section there will be elaborated on market potential.

Market Analysis

Currently, robotic probes have only landed at low elevation to use the thickest part of the Martian atmosphere for aerodynamic deceleration. The limiting factor was the size of the aeroshell used. The radius of a rigid shell is limited by the radius permitted by the launcher fairing, advantageously, an inflatable aeroshell does not have this size limitation. It was shown in [3] that a HIAD of $15m$ diameter could slow down a mass comparable to MSL ($3.3tons$) to subsonic speeds at $20km$ altitude. This reveals the potential of inflatable decelerators to land heavy payloads on elevations that were previously inaccessible.
Based on [3] and [68] different mission applications are determined for the HIAD, these are given in Table 12-1 together with the expected market potential. The following sections will elaborate on the different mission types and their market potential. Three areas of application have been investigated - the Mars environment (being the primary focus of the design project), other planetary missions, and applications for cargo or vehicle return from Earth orbits.

Mars Market The Mars exploration market can be divided into three niches - robotic probe exploration, human exploration missions, and technology development & risk reduction for human Mars missions. The latter is for gathering knowledge during the necessary studies that have to be performed during development. This development and risk reduction information is valuable for parties that want to perform missions to Mars, resulting in a medium market potential.
Human exploration missions exist both for the manned mission itself and for multiple precursor missions that provide supplies for the stay and propellant for the return transfer. Since the project objective is to design a human rated HIAD, it is possible to perform both precursor and the manned missions with the same HIAD design. This increases the market size of the HIAD significantly. Thereby it is possible that once a manned return mission is performed successfully, private space companies will develop interests for performing human-rated missions. These companies form an emerging market of medium market potential. An example of a similar occurrence with a company is the Interplanetary Media Group with the Mars One program that offers a one-way trip to Mars [69].
Additionally, a spacecraft that is capable of soft landing heavy payload is also capable of landing robotic probe exploration missions. There are, however, very few missions to Mars. Only a handful of probes have attempted a soft landing in the history of space exploration. Therefore this market segment is small.

Other Planets Missions to planets that contain an atmosphere can make use of the HIAD. This market is similar to the market niches described for Mars. However, missions to Mars are more attractive due to the location of Mars within the solar system's habitable zone, and the relative shorter distance to Earth. Consequently, there is less interest in exploration missions to other planets that make this market niche small.

Earth Market Despite the project focus on aerocapture and EDL for Mars, the technology can also be applied to the Earth reentry market. The advantage is that there is a larger amount of potential missions to which the technology is applicable. This results with a medium to large market potential. Different mission types include robotic/crew return, garbage return and booster/launcher return.

Currently, the only vessel that can deliver cargo from the ISS to earth is the Dragon from SpaceX. The Russian Soyuz spacecraft has return capabilities, but the space on board is sufficient only for three astronauts during re-entry. The price of a full Dragon mission is 115 million USD [70], for which $3000kg$ can be landed. If their competitor in the private space sector, Orbital Sciences, would add a heat-shield to the Cygnus spacecraft with its cargo hold of $2000kg$ capacity, it could also perform cargo return. In the current contract with NASA, eight resupply missions to the ISS are performed for 1.9 billion USD [71], amounting to almost 240 million USD per mission. Not only would Orbital Sciences receive more income from returning cargo, but they could also re-use the same vehicle for multiple missions due to the heat protection of the aeroshell and thus reduce mission costs. As cost information for a Cygnus spacecraft is not public, no reliable estimate can be made for a marketable price of the aeroshell. Thereby, NASA can also design their own return vehicle to save cost. Evidence of this is the schedule for 2016 where NASA's HEART mission is planned to demonstrate a $5000kg$ return mission [62].
In addition to returning robotic/crew or garbage from space stations, cost savings can be achieved if launch vehicles are re-used; It is the goal of SpaceX to make their first and second stage fully reusable to achieve significant cost savings. Current plans have incorporated a rigid heat-shield on the second stage that reaches (near) orbital velocities. Conveniently, the inflatable aeroshell could also be used here and on other reusable launch systems.

Chapter 13

Conclusion

The report objective is the design and development of a controllable system architecture for the guided atmosphere-assisted deceleration of an aeroshell that allows an exploration-class precursor spacecraft to arrive at a target box with given specifications. The Final Review serves as documentation for the detailed conceptual analysis performed on the recommended design option for controllability - the external, double c.g. offset system. Analysis was performed in four major parts that supplement the conclusions drawn in the Midterm Review. These four parts consist of the General Overview, Design Analysis, Design Review, and Future Outlook and Final Comments.

General Overview - Throughout Section 1-1 to Section 2-2, the general overview lays out the groundwork for the whole report by clearly defining the problem statement, the spacecraft functions, the mission requirements and outlines preliminary work already performed and conclusions drawn. In Section 2-2, the final design was presented as a technical drawing for visualization of the final product. A summary was provided in A with the overall characteristics of the spacecraft detailing its most important properties. The whole report built towards this final design configuration and its characteristics through technical analysis and systems engineering.

Design Analysis - In Chapter 4, the aerodynamic characteristics were determined using the Newtonian method for hypersonic flow where the shape of the aeroshell was modeled to get the overall pressure distribution. The drag, lift and pitch moment coefficients (C_D, C_L, and C_m) where then determined for variations of Mach number, angles of attack, cone angle and radius of aeroshell. The nominal aerodynamic characteristics at trim conditions were determined to be $C_L = 0.36$, $C_D = 1.36$ and $C_m = 0.25$ at angle of attack $19deg$.

Astrodynamic trajectory modeling is found in Chapter 3. Using Kepler orbital mechanics (neglecting irregularities) and high energy type-I transfers, an interplanetary flight plan is recommended based on minimizing energy while complying with human-class regulations. The principle limitation of the approach is that it is only applicable for long duration missions to Mars (around 500 days). The recommendation for interplanetary travel involves a transfer time to Mars taking 199 days, a stay of 515 days and a return flight of 199 days which minimizes ΔV to only $22.10km/s$. This requires a launch mass of $595,000kg$ at Earth and $271,000kg$ at Mars.

In Chapter 5, a linearized Predictor-Corrector scheme was used to integrate over the equations of motions to determine the entrance corridor for the aerocapture and entry, descent and landing maneuvers. The entrance corridor is defined by a combination of skip-out conditions, thermal, mechanical and acceleration peak loads. Based on risk mitigation and optimization (with respect

to energy and loads), final reference trajectory are recommended for aerocapture and EDL. Requirements to meet the target box conditions proved too stringent for the EDL maneuver, forcing the diameter of the HIAD to be increased to $6.5m$.

The thermal protection system was designed in Chapter 6. This entailed using Fay and Riddell equations for thermodynamical analysis of 1 dimensional heat transfer through the thickness of the TPS. This modeling was done at an elementary level involving many simplifying assumptions. Analysis commenced with the determination of the stagnation temperature and heat loading at the aeroshell's stagnation point. The heat distribution over the entire aeroshell was then modeled, enabling material selection based on the highest temperature and heat occurring on the aeroshell. The global maximum temperature was determined at $638.3°C$ at the aeroshell stagnation temperature for the aerocapture maneuver while the heat flux peaked at the stagnation point with $68.1W/cm^2$.

Chapter 7 commenced with the gathering of reference data to calculate ratios that were used for interpolation to get values relevant to the mission spacecraft. Requirements and constraints related to geometry were considered and the overall spacecraft dimensions were sized. Possible actuation system designs were explored and a recommendation was made after analyzing the technical readiness level and RAMS characteristics. A double rail system was chosen to actuate the external, double c.g. offset system designed for controllability. Maximum characteristic loading was obtained using the reference trajectory that determined the maximum internal shear force, normal force and moment acting at the actuation system. These were $28.76kN$, $375.12kN$, and $258.57kNm$ respectively. In the feasibility study on the control structure design, the maximum loading cases for an extreme trajectory were used to size a basic rail system. Overall system mass was conservatively estimated to be $408kg$. The rail system was not optimized for mass nor cost but aimed to prove the feasibility of using such a concept. The study discussed the possibility to decrease the mass to an acceptable level but further analysis is still required before the concept can be proved feasible.

Presented in Chapter 8, the guidance and control analysis had three purposes. Firstly, to provide requirements for structural shifting of the aft-center body needed to control the trajectory. Secondly, to asses the feasibility of the control concept using double-axis, external center-of-gravity shift as a means for active control. Thirdly, to design the controller itself so that the natural motion of the spacecraft is analyzed and the reference trajectory can be followed with an allowable margin of error. The maximum required shift along the $z - axis$ determined a need of $0.7m$ of physical shift between the aft-center body and aeroshell. The corresponding max rate of translation is $10cm/s$. The design of the controller proved to be too extensive to finish entirely, thus efforts were limited to a velocity and flight path angle controller. The simulation showed that the flight path angle and the velocity could indeed be tracked using a longitudinal c.g. offset. However, at this stage, oscillation are present in the $\gamma - controller$ for the EDL and in the $V - controller$ for the EDL and the aerocapture. These oscillations seem to be related to the fact that tho controller is underdeveloped. Therefore, the design concept using double, external c.g. offset for longitudinal controllability was at this stage deemed feasible.

Design Review - Composing of Chapter 9 to Chapter 11, the design analysis proceeds further with studies that reflect the analysis of the design spacecraft with respect to market analysis, sustainability, operations and logistics, sensitivity, technical risk, RAMS, and mission requirements. The mass estimation for the TPS system was conservative, but it concluded that the required system for control and deceleration will have a mass fraction above the requirement limit of 10% ($1000kg$). At an estimated $1700kg$, the requirement for the deceleration system was consequently, unable to be met. The market analysis probed into the potential emerging markets it creates with enabling missions to Mars as well as its applications for other planets and Earth re-entry missions. The logistic analysis focuses on the logistics of the hardware during the pre-launch segment where strict deadlines are anticipated to ensure the hardware assembly does not miss the launch window or the consequence is a 26 month delay. Operations description concentrates on the mission support structure after launch where the spacecraft systems are expected to have a high level

of autonomy due to significant delays in communication with ground control. The sustainable development analysis outlines the compliance of the spacecraft design against the sustainability strategy and guidelines set by governing bodies. The performance analysis includes a sensitivity analysis which identifies which parameters influence the design the most and what the resulting affects are on their respective individual disciplines. Also included is a technical risk assessment which determines the most critical risk factors and ways to mitigate their likelihood and consequence. Additionally, a compliance matrix is included that checks what relevant requirements have been established and how far the current spacecraft design meets them.

Future Outlook and Final Comments - In Chapter 12, the future outlook is described by the project design and development logic. The steps needed to developed the current system design to the stage necessary to perform reliable Mars missions can be divided in steps required for the near and far future. Although much preliminary calculations have been performed, more detailed analysis is planned to further the design from the conceptual design phase to actual production and operation.

Overall, the Final Review was a successful exercise which did more than explore existing designs but gaged the feasibility of the potential design concept selected from the Midterm Report - using external, double center-of-gravity offset for controllability. The simulation did provide conclusive proof that center-of-gravity offset is indeed a feasible concept. However, it is the view of the group that the problems encountered during simulation can be solved given the right amount of resources. The mission need statement is still an existing need and will not be fulfilled until the design concept has reached an operational phase. However, the project objective has been fulfilled. We have designed a potentially, controllable system architecture that can follow a trajectory that decelerates the spacecraft (that is large and heavy enough for human-rating) from interplanetary flight at $7km/s$ to $1.8Mach$ at $13km$ above the Martian Surface. It has also been designed to decelerate in a trajectory with manageable aerodynamic loads and includes a controller to ensure it is followed with allowable deviations. Unfortunately, the mass fraction requirement for the deceleration system could not be met and mass saving comparisons with thruster systems have yet to be performed. Further iterations, corrections and analysis are still required to bring the design concept into realization, however, the fundamental groundwork has been laid for future endeavors to complete in the hope that mankind can finally break free from its earthly bounds.

Appendix A

Spacecraft specifications summary

This appendix gives all relevant design parameters. The parameters are structured in the following order:

1. Table A-3 summarizes the General Spacecraft Characteristics.
2. In Table A-1, the aerocapture parameters are presented.
3. In Table A-2, the EDL parameters are summarized.

Table A-1: Final Aerocapture specifications

Aerocapture Characteristics

Design Parameter	Variable	Magnitude	Unit	Reference
Trajectory Characteristics				
Entrance velocity	V_{en}	7000	m/s	Chapter 5
Exit velocity	V_{ex}	4715.7	m/s	Chapter 5
Entrance angle	γ_{en}	-11.05	deg	Chapter 5
Skip out margin		± 0.5	deg	Chapter 5
Exit angle		9.08	deg	Chapter 5
Angle of attack	α	-16	deg	Chapter 5
Maximum G-Load	g_{max}	3.3	-	Chapter 5
Time	t	271.3	s	Chapter 5
Minimum altitude	h_{min}	51.5	km	Chapter 5
Groundtrack distance	R	1520.5	km	Chapter 5
TPS				
Maximum heat flux	$\dot{q}$	68.13	$W/cm2$	Chapter 6
Total heat load	q	6214.2	$J/cm2$	Chapter 6
Temperature at wall	T_w	916.95	K	Chapter 6

Table A-2: Final EDL specifications

Entry Descent to Landing Characteristics

Design Parameter	Variable	Magnitude	Unit	Reference
Trajectory Characteristics				
Entrance velocity	V_{en}	4715.3	m/s	Chapter 5
Target Mach number	V_{ex}	1.8v	m/s	Chapter 5
Entrance angle	γ_{en}	-11.55v	deg	Chapter 5
Skip out margin		± 0.5v	deg	Chapter 5
Angle of attack	α	$-19 \rightarrow -9.5 \rightarrow -19$	deg	Chapter 5
Maximum G-Load	g_{max}	4.11	-	Chapter 5
Time	t	400.3	s	Chapter 5
Groundtrack distance	R	943.718	km	Chapter 5
TPS				
Maximum heat flux	$\dot{q}$	27.94	$W/cm2$	Chapter 6
Total heat load	q	2401.8	$J/cm2$	Chapter 6
Temperature at wall	T_w	763.65	K	Chapter 6

Table A-3: Summarized General Spacecraft Characteristics

Design Parameter	Variable	Magnitude	Unit	Reference
Spacecraft Dimensions				
Spacecraft mass	m_{sc}	1000	kg	Section 1-3
$X_{c.g.}$ vehicle	$X_{c.g._vehicle}$	3.6	m	Section 7-1
Payload length	$l_{payload}$	4.22	m	Section 7-1
Spacecraft radius	r_{sc}	5	m	Section 1-3
Control System				
Lateral c.g. shift (min)	$\delta c.g._{y,aft}min$	-0.1	m	Chapter 8
Lateral c.g. shift (max)	$\delta c.g._{y,aft}max$	0.1	m	Chapter 8
Lateral c.g. shift speed (min)	$\dot{\delta} c.g._{y,aft}min$	-0.1	m/s	Chapter 8
Lateral c.g. shift speed (max)	$\dot{\delta} c.g._{y,aft}max$	0.1	m/s	Chapter 8
Longitudinal c.g. shift (min)	$\delta c.g._{z,aft}min$	*-0.7*	m	Chapter 8
Longitudinal c.g. shift (max)	$\delta c.g._{z,aft}max$	*0.2*	m	Chapter 8
Longitudinal c.g. shift speed (min)	$\dot{\delta} c.g._{z,aft}min$	-0.1	m/s	Chapter 8
Longitudinal c.g. shift speed (max)	$\dot{\delta} c.g._{z,aft}max$	0.1	m/s	Chapter 8
Actuation mechanism mass	m_{mech}	370	kg	Section 7-3-3
Aeroshell				
Aeroshell radius	R_{as}	6.5	m	Section 5-5
Aeroshell half-nose angle	δ	62.5	deg	Section 7-1
Inflation volume	V_inf	36.6	m^3	Section 7-1
Nose radius	RN	5.41	m^3	Section 7-1
Thermo Protection System				
Outerlayer	$SIRCA-15$	5	mm	Chapter 6
Insulator	$Pyrogel$ 6650	52	mm	Chapter 6
Boundary	RTV $560-32$	17.5	mm	Chapter 6
Target Orbit Caracteristics				
Orbital Time	T	24.66	h	Section 3-2
Apoapsis altitude	ra	37307	km	Section 3-2
Periapsis altitude	rp	3589	km	Section 3-2
Closest Distance to Mars	ha	200	km	Section 3-2
Semi major axis	a	20448	km	Section 3-2
Eccentricity	e	0.8245	-	Section 3-2
Mission Caracteristics				
Total Duration	T_{total}	913	$days$	Chapter 3
Tranfer time to Mars	T_{E-M}	199	$days$	Chapter 3
Tranfer time to Earth	T_{M-E}	199	$days$	Chapter 3
Delta-V budget total	dV_{total}	22.1	km/s	Chapter 3
Mission time	$T_{Mission}$	515	$days$	Chapter 3
Launch mass at Earth	m_launch	595	ton	Chapter 3
Launch mass at Mars	m_launch	271	ton	Chapter 3

Appendix B

List of Requirements

This appendix presents the full list of requirements in Figure B-2 and Figure B-3. An explanatory legend in included in Figure B-1.

	Type	Status	Certainty
Legend	GE = General HUM = Human DEV = Development Requirements AER = Aerodynamics AST = Astrodynamics GNC = Guidance, Navigation & Controll TPS = Termal Protection System	1 = Requirement met 2 = Requirement met, but altererd with customer's agreement 3 = Requirement's compliance not yet determined 4 = Requirement not met	1 = High certainty 2 = Low certainty regarding accuracy 3 = Overall low certainty
	Level	**Key**	
	H = Hard Requirement S = Soft Requirement	K=Key requirement	

Figure B-1: Legend to the requirement list.

Req. Number	Type	Requirement	Date	Level	Key	Status	Certainty
1	AER	The spacecraft is to perform Entry, Descent and Landing to a target velocity of Mach 1.8 at 13 km	5/26/2013	H	K	1	2
2	AER	The spacecraft is to guide the Entry, Descent and Landing along the determined downrange with a final accuracy of ±150m at 13km altitude	5/26/2013	H	K	1	2
3	AER	The aerocapture must allow for dissipation of enough energy to leave the martian atmosphere with 4715 m/s	5/29/2013	H	K	1	2
4	AER	The GNC must allow for an aerocapture exit flight path angle of 9.08 deg	6/18/2013	H	K	1	2
5	AER	The spacecraft is to guide the Entry, Descent and Landing along the determined crossrange with a final accuracy of ±37.5m at 13km altitude	5/26/2013	H	K	3	N/A
6	AER	The spacecraft is to enter the atmosphere at a speed of 7 km/s with a flight path angle of -11.05 deg	5/2/2013	S	K	1	1
7	AER	The aeroshell must be able to generate a lift force via a controlled change in the angle of attack with the specified accuracy	5/2/2013	S		1	1
8	AER	The aeroshell must be able to generate a side force via a controlled change in the sideslip angle with the specified accuracy	5/2/2013	S		1	2
9	AER	The aeroshell must generate sufficient drag in order to allow the deceleration of the vehicle in accordance with requirement 14	5/2/2013	S		1	1
10	AST	The target orbit after aerocapture must be a 1 sol orbit with periapsis height of 200 km above surface	5/29/2013	S		1	1
11	DEV	The conceptual development of the system must be performed by 10 students in 10 weeks using the facilities provided by TU Delft	5/2/2013	H		1	1
12	DEV	The system must ensure that sustainability aspects are respected in accordance with UN	5/2/2013	H		1	1
13	DEV	The system must ensure that human safety regulations are respected in accordance with NASA	5/2/2013	H		3	N/A
14	DEV	The system must make use of off-the-shelf materials	5/2/2013	S		1	2
15	DEV	The cost of the system must stay within the budget specified by the costumer	5/2/2013	S		3	N/A
16	GE	The system must be designed to work on the Martian atmosphere within the most extreme measured conditions	5/2/2013	H		1	3
17	GE	The system must be in reusable conditions after landing on Mars	5/2/2013	H		3	N/A
18	GE	The system must be proven to work in ultimate conditions before final mission launch	5/2/2013	H		3	N/A
19	GNC	The system must employ an automated control system which can perform the landing on Mars autonomously	5/2/2013	H	K	1	1
20	GNC	The system must ensure a stable flight	5/2/2013	H		1	2
21	GNC	The system must ensure that all required measured values stay within the measurable ranges by the sensors employed	5/2/2013	H		1	1
22	GNC	The system must ensure a maximum failure percentage of 0.0005%	5/2/2013	H		3	N/A
23	GNC	If the manual control system is activated, the system must be able to warn the humans on board of impeding danger	5/2/2013	H		3	N/A
24	GNC	The system must be able to provide the minimum cross range and downrange specified. This requirement is in accordance with requirements 8 and 9	5/2/2013	S		1	2
25	GNC	The system must ensure attitude control with the specified accuracy. This requirement is in accordance with requirements 25 and 26	5/2/2013	S		1	2
26	GNC	The accelerations for the bank mauever must have an acceleration between 2-5 deg/s^2.	5/29/2013	S		1	3
27	HUM	The accelerations on the spacecraft must not exceed 5.2g	5/26/2013	H	K	2	1
28	HUM	The time between aerocapture and EDL must not exceed 10 days	6/3/2013	S	K	1	1

Figure B-2: Part 1 of the total requirement list.

29	HUM	The system must allow for Earth communication as specified by health conditions and mission related updates	5/2/2013	H		3	N/A
30	STR	The mass of the vehicle must not exceed 10 000 kg	5/2/2013	H	K	1	1
31	STR	The diameter of the fairing must not exceed 5 m	5/2/2013	H	K	1	1
32	STR	The mass of the hypersonic atmospheric assisted decelerator must not exceed 10% of the vehicle's entry mass	5/2/2013	H	K	4	N/A
33	STR	The diameter of the aeroshell must not exceed 13 m	5/2/2013	S	K	2	1
34	STR	The vehicle must fit within the maximum static payload length of 16.484 m for the Delta IV launch vehicle	5/29/2013	H		1	1
35	STR	The elements of the vehicle that are not protected by the TPS cannot be exposed to the flow	5/30/2013	H		1	1
36	STR	The design should ensure that at least a second redundant control system is present	5/2/2013	S		1	2
37	STR	The system must be able to withstand the peak loads during the acceleration spike.	5/2/2013	S		1	2
38	STR	The airframe must keep all deformations within their respective specified ranges	5/2/2013	S		3	N/A
39	STR	The system must be able to withstand continuous pressure loads for the specified amount of time	5/2/2013	S		3	N/A
40	STR	The structure must ensure that the vibration frequency is kept below the specified maximum	5/2/2013	S		3	N/A
41	TPS	The TPS system of the aeroshell must be able to withstand the heat flux during aerocapture and EDL	5/29/2013	H	K	1	2
42	TPS	The material composition of the structure must be such that no unexpected/uncontrolled reactions take place with the martian atmosphere.	5/2/2013	H		1	1
43	TPS	The system must be able to withstand the peak temperature at the surface	5/2/2013	H		1	1
44	TPS	The system must ensure constant pressure in the shell within the specified range	5/2/2013	H		3	N/A
45	TPS	The system must be able to ensure heat insulation for the capsule during landing to assure a maximum temperature of 30° C in the payload.	5/29/2013	S		3	N/A

Figure B-3: Part 2 of the total requirement list.

Bibliography

[1] T. De Boer, M. Coppola, W. Dalmeijer, *et al.*, "Design synthesis exercise project plan," tech. rep., Delft University of Technology, 2013.

[2] T. De Boer, M. Coppola, W. Dalmeijer, *et al.*, "Design of a controllable inflatable aeroshell - baseline review," 2013. Not published.

[3] R. A. Dillman, N. F. Cheatwood, S. J. Hughes, *et al.*, "Planned flight of the inflatable reentry vehicle experiment 3 (irve-3)," in 8^{th} *International Planetary Probe Workshop, Portsmouth, Virginia, June 6-10, 2011*, (Pasadena, CA), June 2011.

[4] T. De Boer, M. Coppola, W. Dalmeijer, *et al.*, "Design synthesis exercise mid-term report," tech. rep., Delft University of Technology, 2013.

[5] NASA, "Nasa-std-3001 - nasa space flight human system standard volume 1: Crew health," 2007.

[6] R. Noomen, "Flight and orbital mechanics - course ae2104 - tu delft," 2012. Internal Source.

[7] J. Cruz *et al.*, "Entry, descent, and landing technology concept trade study for increasing payload mass to the surface of mars," 2005.

[8] IHMC Space Exploration, "Types of human mars missions." http://cmapspaceexp.ihmc.us/rid=1J205X95J-C8GJBR-216R/Long{%}20and{%}20Short{%}20Stay{%}20Human{%}20Missions{%}20to{%}20Mars.cmap.

[9] J. Cornelisse, H. Schöyer, and K. Wakker, *Rocket propulsion and spaceflight dynamics*. No. pt. 1 in Aerospace Engineering Series, Pitman, 1979.

[10] A. Dwyer-Cianciolo, J. Davis, D. Komar, *et al.*, "Entry, descent and landing systems analysis study: Phase 1 report," 2010.

[11] J. D. Anderson, *Fundamentals of Aerodynamics, fifth edition*. McGrawHill, 2011.

[12] J. D. Anderson, *Hypersonic and Hight Temperature Gas Dynamics*. AIAA, 2006.

[13] P. A. Gnoffo, K. J. Weilmuenster, R. D. Braun, *et al.*, "Influence of sonic-line location on mars pathfinder probe aerothermodynamics," *Journal of Spacecraft and Rockets*, vol. 33, pp. 169–177, 1996.

[14] K. T. Edquist, P. N. Desai, and M. Schoenenberger, "Aerodynamics for mars phoenix entry capsule," *Journal of Spacecraft and Rockets*, vol. 48, pp. 713–726, 2011.

[15] D. R. Williams, "Mars fact sheet." http://nssdc.gsfc.nasa.gov/planetary/factsheet/marsfact.html, November 2010.

[16] F. Forget, F. Montmessin, J.-L. Bertaux, *et al.*, "Density and temperatures of the upper martian atmosphere measured by stellar occultations with mars express spicam," *Journal of Geophysical Research: Planets (1991–2012)*, vol. 114, no. E1, 2009.

[17] C. G. Justus and R. D. Braun, "Atmospheric environments for entry, descent and landing (edl)," 2007.

[18] Marshall Space Flight Center, "Mars transportation environment definition document," March 2001. marsGram.

[19] F. Reagan and S. Anandakrishnan, *Dynamics of Atmospheric Re-Entry*. AIAA Education Series, American Institute of Aeronautics and Astronautics, 1993.

[20] S. B. Josselyn, "Optimization of low thrust trajectories with terminal aerocapture," diploma thesis, Naval Postgraduate School, 2003.

[21] K. Sutton and R. A. Graves Jr, "A general stagnation-point convective heating equation for arbitrary gas mixtures," 1971.

[22] P. Gallais, *Atmospheric Re-Entry Vehicle Mechanics*. Springer Berlin Heidelberg, 2007.

[23] J. J. Bertin, *Hypersonic Aerothermodynamics*. Aiaa, 1994.

[24] J. D. Anderson, *Hypersonic and High Temperature Gas Dynamics*. Aiaa, 2000.

[25] B. E. Poling, J. M. Prausnitz, O. John Paul, *et al.*, *The Properties of Gases and Liquids*, vol. 5. McGraw-Hill New York, 2001.

[26] J. P. Holman, "Heat transfer," *McGrawHill, New York*, 2002.

[27] V. Menezes, S. Saravanan, G. Jagadeesh, *et al.*, "Experimental investigations of hypersonic flow over highly blunted cones with aerospikes," *AIAA journal*, vol. 41, no. 10, pp. 1955–1966, 2003.

[28] R. A. Beck, J. O. Arnold, S. White, *et al.*, "Overview of initial development of flexible ablators for hypersonic inflatable aerodynamic decelerators," in *21st AIAA Aerodynamic Decelerator Systems Technology Conference and Seminar*, pp. 23–26, 2011.

[29] J. A. Del Corso, W. Bruce, K. A. Liles, *et al.*, "Thermal analysis and testing of candidate materials for paidae inflatable aeroshell," *AIAA Paper*, vol. 2925, 2009.

[30] J. A. Del Corso, F. Cheatwood, W. E. Bruce III, *et al.*, "Advanced high-temperature flexible tps for inflatable aerodynamic decelerators," 2011.

[31] D. Lichodziejewski, C. Kelley, B. Tutt, *et al.*, "Design and testing of the inflatable aeroshell for the irve-3 flight experiment," 53rd AIAA/ASME/ASCE/AHS/ASC Structures, Structural Dynamics and Materials Conference, 2012.

[32] P. Fortescue, G. Swinerd, and J. Stark, *Spacecraft Systems Engineering*. Wiley, 2011.

[33] T. R. White, M. Mahzari, D. Bose, *et al.*, "A reconstruction of aerothermal environment and thermal protection system response of mars science laboratory entry vehicle," 2013.

[34] R. D. Braun and R. M. Manning, "Mars exploration entry, descent and landing challenges," in *IEEE Aerospace Conference, Big Sky, Montana, March 4-11, 2006*.

[35] E. F. Sheta, V. Venugopalan, X. Tan, *et al.*, "Aero-structural assessment of an inflatable aerodynamic decelerator," Contractor Report 216731, CFD Research Corporation, Hutsville, Alabama, Hampton, Virginia, August 2010. Prepared for Langley Research Center under Contract NNM06AA10C.

[36] R. Dillman, "Meeting regarding the measurements from irve-3," 2013.

[37] I. Richardson, "Meeting regarding mechanical linkages (11/06/2013)," 2013.

[38] K. Karagiozis, F. Cirak, R. Kamakoti, *et al.*, "Computational fluid-structure interaction methods for simulation of inflatable aerodynamic decelerators," in *20th AIAA Aerodynamic Decelerator Systems Technology Conference and Seminar*, pp. 4–7, 2009.

[39] M. C. Lindell, S. J. Hughes, M. Dixon, *et al.*, "Structural analysis and testing of the inflatable re-entry vehicle experiment (irve)," *AIAA Paper AIAA*, vol. 1699, pp. 1–4, 2006.

[40] A. D. Olds, R. Beck, D. Bose, and otherst, "Irve-3 post-flight reconstruction," in *22nd AIAA Aerodynamic Decelerator Systems Technology Conference*, 2013.

[41] Canadian Space Agency, "The structure of canadarm." http://www.asc-csa.gc.ca/eng/canadarm/description.asp, June 2013.

[42] ASM Aerospace Specification Metals Inc., "Titanium ti-6al-4v (grade 5), sta." http://asm.matweb.com/search/SpecificMaterial.asp?bassnum=MTP642.

[43] N. P. on Technology Enhanced Learning, "Shearing stress distribution in typical cross-sections." http://www.nptel.iitm.ac.in/courses/Webcourse-contents/IIT-ROORKEE/strength{%}20of{%}20materials/lects{%}20{&}{%}20picts/image/lect28{%}20and{%}2029/lecture{%}2028{%}20and{%}2029.htm.

[44] Y. T. Chung and B. L. Foist, "Prediction of payload random vibration loads," in *SPIE the International Society for Optical Engineering*, pp. 934–934, SPIE the International Society for Optical Engineering, 1995.

[45] R. Nave, "Friction assumptions." http://hyperphysics.phy-astr.gsu.edu/hbase/frict3.html.

[46] R. Beardmore, "Coefficient of friction." http://www.roymech.co.uk/Useful_Tables/Tribology/co_of_frict.html.

[47] National Programme on Technology Enhanced Learning, "Theories of elastic failure." http://www.nptel.iitm.ac.in/courses/Webcourse-contents/IIT-ROORKEE/strength{%}20of{%}20materials/lects{%}20{&%}20picts/image/lect35/lecture35.htm.

[48] J. Mulder, W. van Staveren, J. van der Vaart, and others., *Flight Dynamics Lecture Notes*. Delft University of Technology, 2013.

[49] T. Petsopoulos, F. J. Regan, and J. Barlow, "Moving-mass roll control system for fixed-trim re-entry vehicle," *Journal of Spacecraft and Rockets*, vol. 33, no. 1, pp. 54–60, 1996.

[50] E. W. Weisstein, "Moment of inertia – from eirc weisstein's world of physics." http://scienceworld.wolfram.com/physics/MomentofInertia.html.

[51] J. Graves, "Inertial measurement unit (imu)." http://www.ssl.umd.edu/projects/RangerNBV/thesis/2-4-1.html.

[52] F. M. Cheatwood, N. LaRC, *et al.*, "Msl edl instrument (medli) suite." http://msl-scicorner.jpl.nasa.gov/Instruments/MEDLI/. Visited on 22 June 2013.

[53] L. Sonneveldt, Q. Chu, and J. Mulder, "Adaptive backstepping flight control for modern fighter aircraft," *Unpublished doctoral dissertation, Delf University of Technology*, 2010.

[54] J. Wertz and W. Larson, "Space mission analysis and design." http://books.google.nl/books?id=veyGEAKFbiYC, 1999.

[55] E. Harris and D. Dreyfuss, "Manned spacecraft electrical power systems: Requirements, weight correlation and cost implications," in *A Collection of Technical Papers: Intersociety Energy Conversion Engineering Conference, Los Angeles, California, September 26-28, 1966*, p. 162, American Institute of Aeronautics and Astronautics, 1966.

[56] A. Dwyer-Cianciolo, J. Davis, D. Komar, *et al.*, "Entry, descent and landing systems analysis study: Phase 2 report," 2011.

[57] T. A. Zang, A. M. Dwyer-Cianciolo, *et al.*, "Overview of the nasa entry, descent and landing systems analysis study," *AIAA Paper*, vol. 8649, 2010.

[58] P. Brugarolas, M. San Martin, and E. Wong, "The rcs attitude controller for the exo-atmospheric and guided entry phases of the mars science laboratory," in *International Planetary Probe Workshop*, 2010.

[59] H. S. Systems, "Apollo sevice module rcs tank." http://www.space1.com/Artifacts/Apollo_Artifacts/SM_RCS_Tank/sm_rcs_tank.html, 2008.

[60] U.S. Department of Energy, NASA, "Space radioisotope power systems: Multi-mission radioisotope thermoelectric generator." http://mars.jpl.nasa.gov/msl//files/mep/MMRTG_Jan2008.pdf, January 2008.

[61] Quallion: Custom Battery Manufacturer of Lithium Ion Batteries, "Product specification ql075ka." http://www.quallion.com/sub-sp-ql075ka.asp.

[62] H. Wright, A. Cutright, J. Corliss, *et al.*, "Design of a controllable inflatable aeroshell - baseline review,"

[63] B. N. Cassenti, "The human exploration of mars," *AIAA paper*, vol. 5608, 2007.

[64] M. S. Hundal, "Product costing: A comparison of conventional and activity-based costing methods," *J. Eng. Design*, 1997.

[65] D. Koelle, *Handbook of Cost Engineering for Space Transportation Systems with TRANSCOST 7.0: Statistical-analytical Model for Cost Estimation and Economical Optimization of Launch Vehicles*. TCS-TR-168/00, TransCostSystems, 2000.

[66] H. Price, A. M. Hawkins, and T. O. Tadcliffe, "Austere human missions to mars," 2009.

[67] N. Cheatwood, "Meeting regarding irve-3," 2013.

[68] S. Hughes, F. Cheatwood, R. Dillman, *et al.*, "Hypersonic inflatable aerodynamic decelerator (hiad) technology development overview,"

[69] Interplanetary Media Group, "About mars one." http://mars-one.com/en/about-mars-one/about-mars-one, 2013.

[70] SpaceX, "Spacex - why the us can beat china: The facts about spacex costs." http://www.spacex.com/usa.php.

[71] T. J. Perrotto, J. Byerly, and B. Beneski, "Nasa partner orbital sciences test launches antares rocket." http://www.nasa.gov/home/hqnews/2013/apr/HQ_13-114_Antares_launches.html.

[72] H. Wright, A. Cutright, J. Corliss, *et al.*, "Heart flight test overview," in *9th International Planetary Probe Workshop*, pp. 16–22, 2012.

[73] D. Williams, "A crewed mission to mars." http://nssdc.gsfc.nasa.gov/planetary/mars/marsprof.html, 2005.

[74] NASA Jet Propulsion Laboratory, "Mars science laboratory - curiosity rover - spacecraft." http://mars.jpl.nasa.gov/msl/mission/spacecraft/.